# RESOLVING THE STELLAR HALO KINEMATICS OF NGC 4945

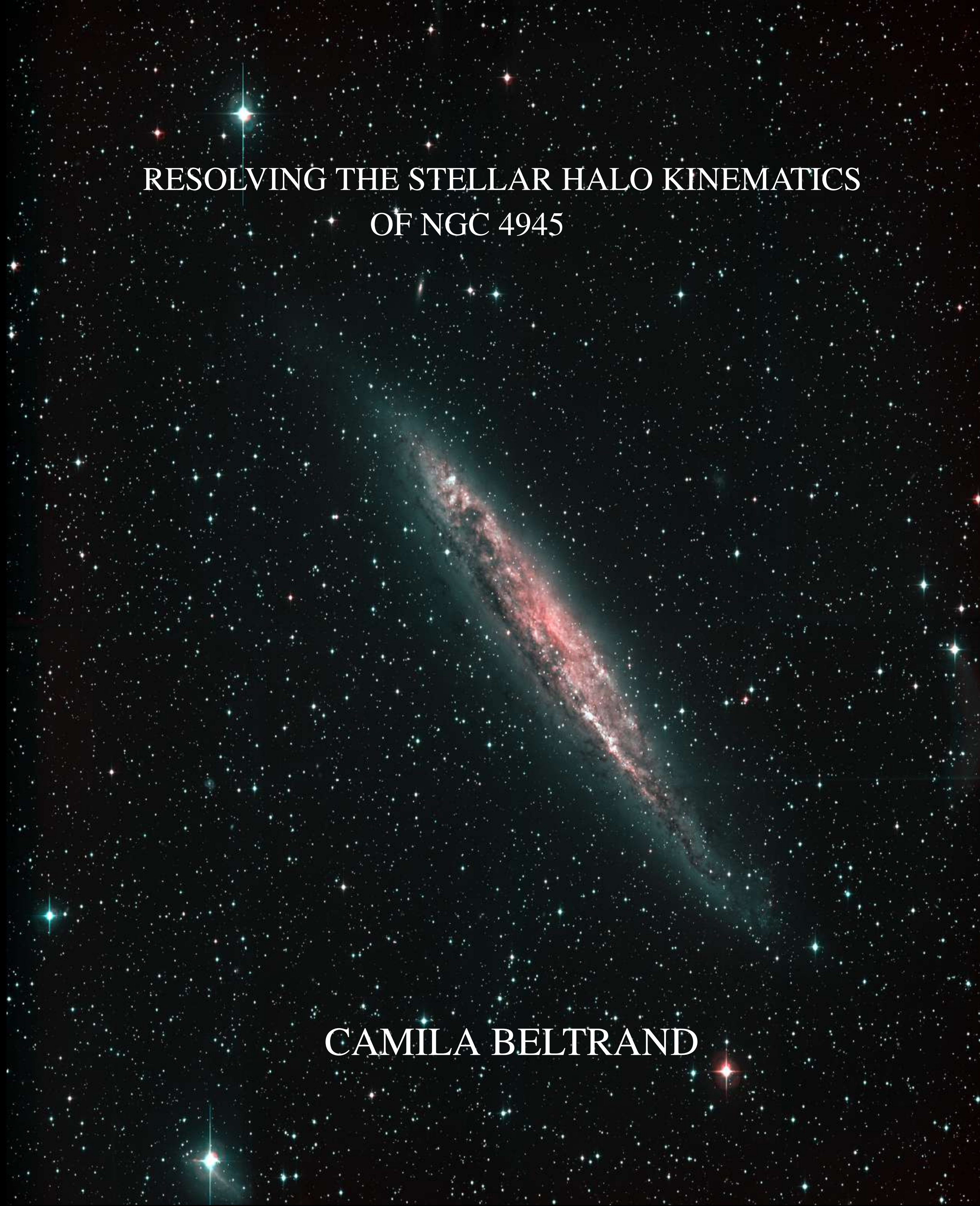

CAMILA BELTRAND

# Resolving the Stellar Halo Kinematics of NGC 4945

Camila Beltrand Calderón

**Doctoral Thesis**

To fulfill the requirements for the degree of Doctorate in Astronomy
at Universidad de La Serena by


## Camila Beltrand Calderón

under the supervision of

Dr. Antonela Monachesi, Universidad de La Serena

and co-supervision of

Dr. Richard D'Souza, Vatican Observatory


Defended on March 28th, 2025 before the committee composed of

Dr. Douglas Geisler, Universidad de La Serena
Dr. Elisa Toloba, University of the Pacific
Dr. Lorenzo Morelli, Universidad de Atacama
Dr. Patricia Tissera, Pontificia Universidad Católica de Chile

**Cover Image:** Color mosaic of the Wide-Field-Imager (WFI) at the MPG/ESO 2.2-m telescope at La Silla. It is assembled from five 15-minute R(red)-narrowband (shown in red), four 5-minute B(blue)-band (shown in green), and five 1000-second U(ultraviolet)-band (shown in blue) exposures. The full image is available in this link. **Credit:** ESO

# Contents

# Abstract

The stellar halos of galaxies, primarily formed through the accretion and merger of smaller objects, serve as a key probe for understanding the hierarchical mass assembly of galaxies. The inner regions of stellar halos in disk galaxies are also predicted to host an *in situ* component, which is expected to be prominent along the major axis. Disentangling the in situ from accreted components requires kinematic information, but the low surface brightness of stellar halos makes this challenging with traditional integrated-light spectroscopy. In this work, we used a novel technique to study the kinematics of the stellar halo of the edge-on galaxy NGC 4945. This galaxy is an ideal target for such a study, as it hosts a typical stellar halo for a MW-like galaxy, with mass and metallicity properties that fall between the extremes represented by the MW and M31. We combine new deep Multi Unit Spectroscopic Explorer spectroscopic observations with existing *Hubble* Space Telescope imaging data to study the kinematics of the stellar halo of the edge-on Milky Way-mass galaxy NGC 4945. By stacking the spectra of individual red giant branch and asymptotic giant branch stars, we measure the line-of-sight (LOS) heliocentric velocity and velocity dispersion in two fields at galactocentric distances of 12.2 kpc (outer disk field) and 34.6 kpc (stellar halo field) along the major axis. We find that the outer disk field exhibits a LOS velocity and velocity dispersion of 673 $\pm$ 11 km s$^{-1}$ and 73 $\pm$ 14 km s$^{-1}$, respectively, consistent with the HI velocity of the disk. In contrast, the halo field shows a LOS velocity and velocity dispersion of 519 $\pm$ 12 km s$^{-1}$ and 42 $\pm$ 22 km s$^{-1}$, respectively, suggesting that the stellar halo at this distance is counter-rotating relative to the disk and likely accreted. To contextualize these results, we compare them with the Auriga and TNG50 cosmological simulations. From these simulations, we measure the LOS velocity and velocity dispersion of stellar halos in MW/M31-like galaxies at distances comparable to our observed fields. The analysis reveals that galaxies with stellar halo kinematics akin to those of NGC 4945 are relatively rare: only 9 out of 180 TNG50 galaxies exhibit comparable kinematic properties. Further restricting the sample to galaxies with stellar halos with masses consistent with observational estimates of the halo mass of NGC 4945 reduces the number of analogs to just six. For these select analog galaxies, we partially reconstruct their accretion histories by identifying the satellites that contributed to their halos, examining their masses, and determining the epochs of accretion. Our results indicate that the kinematic properties of the NGC 4945 stellar halo are consistent with those predicted for halos dominated by accretion events involving massive satellites. This study provides the first resolved stellar kinematic measurements of a stellar halo beyond the Local Group and establishes a novel methodology for probing the kinematic and assembly histories of nearby galaxies.

# Chapter 1

# Introduction

In this chapter, we review how stellar halos form and grow within the context of galaxy formation as described by the ΛCDM paradigm. We focus on the stellar halos of spiral galaxies, as the object of study in this thesis is a spiral galaxy, their recent observational progress, the importance of studying their kinematics through spectroscopy, and the advancements in cosmological simulations that help to understand the significance of stellar halos in deciphering the accretion history of galaxies in the context of the current model of the Universe.

## 1.1 Galaxy growth: A brief history

In 2020, we commemorated the first centenary of what was known as the Great Debate, also known as the Shapley-Curtis Debate, which discussed differing visions of our Universe. Harlow Shapley argued for a Universe consisting of a single, large galaxy, our own Milky Way (MW), while Heber Curtis proposed that the Universe contained numerous galaxies, which were then referred to as "nebulae". It wasn't until 1929, with Edwin Hubble's observations building on Henrietta Leavitt's work with Cepheid variable stars, that the distance to M31 was measured, revealing that Andromeda was indeed a large galaxy far beyond the MW (Hubble, 1929), thus confirming Curtis's view.

Today, we know that the Universe contains billions of galaxies, which are fundamental units of the Universe on a large scale. These galaxies come in a variety of masses and sizes, ranging from small dwarf galaxies containing a few billion stars to massive elliptical galaxies with hundreds of billions of stars. Among them, the MW is a prime example of a spiral galaxy, an intricate system of stars, gas, dust, and dark matter bound by gravity. What makes the MW particularly special is that galaxies of its size, with a stellar mass of $\sim 10^{10}$ $M_{\odot}$, are among the most efficient at converting their baryonic matter into stars. This efficiency plays a crucial role in their evolutionary history, influencing their structure and dynamics. Understanding how galaxies like the MW form and evolve has become one of the primary questions in astronomy. Over many years, astronomers have gathered extensive data to construct models that capture the processes governing the growth of galaxies and other structures. Decades of research have led to the currently favored framework, the Lambda Cold Dark Matter (ΛCDM) model (White & Rees, 1978; Peebles, 1984a,b; Frenk et al., 1988). This model suggests that galaxies form hierarchically through the assembly of smaller structures that merge over time, gradually building up into larger entities (an illustrative scheme of the assembly is displayed in Fig. 1.1). ΛCDM successfully replicates the Universe as we observe today, relying on three main components: dark energy, representing the cosmological constant responsible for the accelerated expansion of the Universe; cold dark matter, which interacts with matter only gravitationally; and baryonic matter, or "normal" matter made of protons and neutrons, which we can observe directly. Observations revealed that our Universe is geometrically flat and dominated by dark matter and dark energy accounting for about $\sim 95\%$ of the energy density (Planck Collaboration et al., 2020). Normal matter makes up for the remaining $\sim 5\%$ (Vogelsberger et al., 2020).

In short, this model proposes that in the first $10^{-32}$ seconds after the Big Bang, the Universe underwent a period of rapid expansion, known as inflation (Guth, 1981). During this phase, small density fluctuations arose in the distribution of matter. Since dark matter interacts only gravitationally, these initial perturbations enabled certain regions in the Universe to attract surrounding matter, initiating their collapse. Dark matter was the first component to collapse, forming halos of dark matter (Frenk et al., 1988). In the high density environment of the early Universe, mergers between halos of comparable sizes were frequent, allowing dark matter halos to grow in mass through successive mergers. Smaller halos joined to form larger structures, creating the scaffolding for galaxy formation. In this hierarchical framework, the merging of smaller structures is the fundamental mechanism driving the growth of halos. Consequently, the evolutionary path of galaxies is intimately tied to the merger history of their host halos. This hierarchical model structure formation best explains the observed clustering of galaxies on large scales (White & Rees, 1978). Gas and dust were subsequently drawn to the centers of these dark matter halos by gravitational attraction. As gas accumulated within the halos, it began to cool through radiative processes, which allowed it to condense further and fragment into smaller clouds. These clouds collapsed under their own gravity, with their centers reaching higher densities and temperatures, leading to the formation of the first stars and galaxies.

As a result of the hierarchical growth of structures through the aggregation of smaller halos in the early Universe, mergers play a critical role in galaxy evolution. Halos, composed of both dark and baryonic matter, bring with them stars and gas that are subsequently accreted by the host galaxy. These accreted populations consist of stars that originally formed in dark matter halos other than that of their current host galaxy.

Mergers can vary in scale; they can be massive, with mass ratios – the ratio of masses between halos – close to unity, representing a significant pathway for stellar mass growth. Such mergers can induce dramatic changes in the central regions of galaxies, including the formation of asymmetries (Quillen et al., 2009), disk heating (Grand et al., 2016), and the creation of vertical structures like warps (Gómez et al., 2017).

On the other hand, minor mergers involve the accretion and tidal disruption of dwarf satellites, which constitute the most common mode of galaxy and galaxy interaction (Bullock & Johnston, 2005). As these satellites fall into the gravitational potential of their host galaxy, they experience tidal forces that gradually strip and redistribute their material. Once disrupted, the remnants of these satellites contribute low-surface-brightness stellar material at large galactocentric distances, forming a variety of coherent structures such as tidal tails, streams, and shells. These features serve as observable imprints of hierarchical galaxy formation, providing insights into the accretion history and merger events experienced by the host galaxy.

While the hierarchical growth of dark matter halos provides the structural framework for the formation and evolution of galaxies, the evolution of their baryonic components is considerably more complex. In galaxies, stars not only form and evolve but also die, enriching the interstellar medium with new chemi-

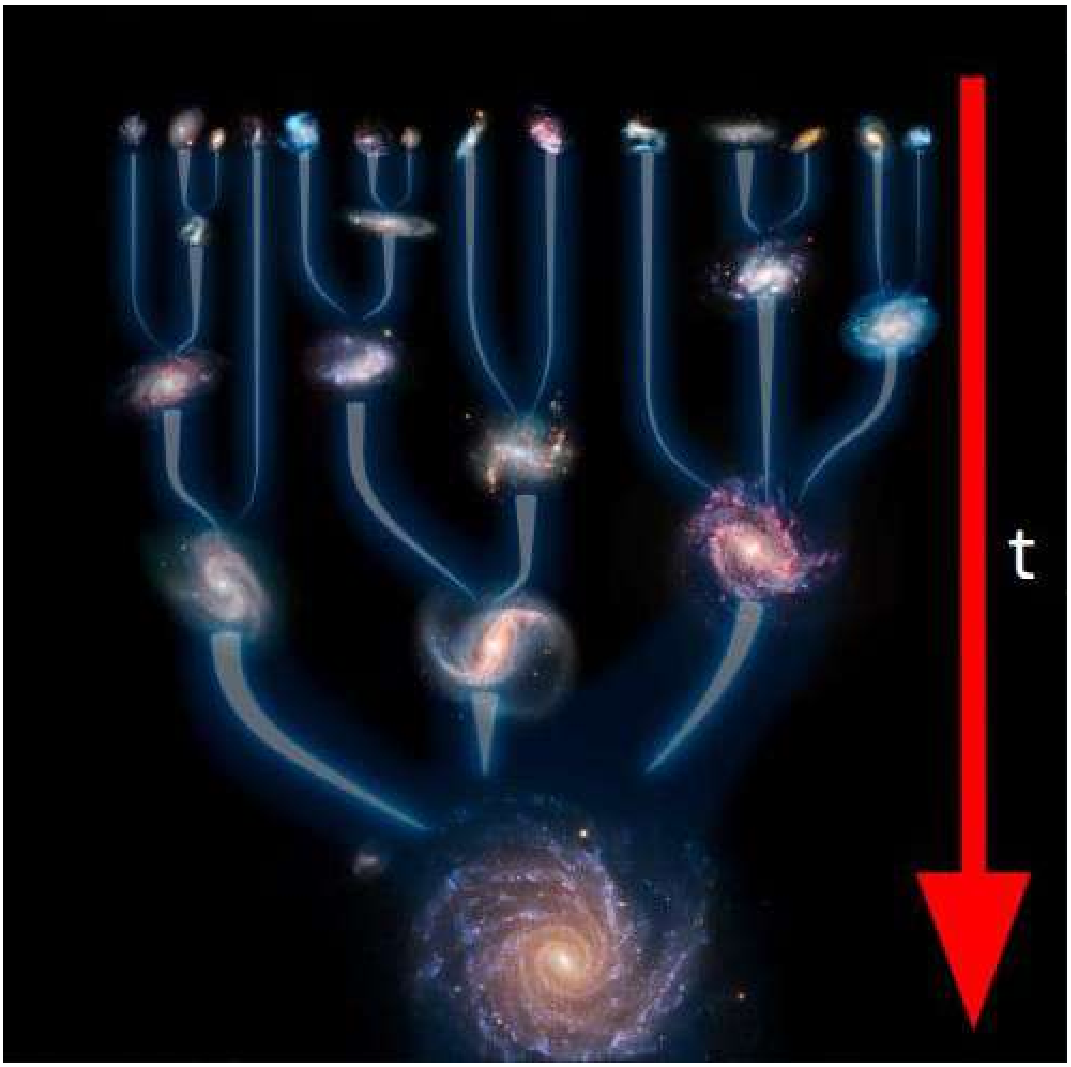


Figure 1.1: Scheme of the hierarchical model for halos growth: small halos, formed first, are the building blocks that merge into a larger one. The red arrow is the direction of the time passing. Credit: ESO/L. Calçada

cal elements through processes such as supernova explosions or stellar winds. Additionally, massive stars and supernova events can eject hot gas, and active galactic nuclei (AGN), powered by supermassive black holes at galactic centers, can heat the surrounding gas or eject it through powerful jets, limiting star formation and regulating galactic growth. On the other hand, inflows of gas from the intergalactic medium or from accreted satellite galaxies provide fresh gas for star formation. However, while these processes are fundamental to understanding galaxy evolution, their study will not be addressed in this thesis.

Hand in hand with the theoretical framework outlined in this Section, observational strategies have been developed over the past decades to find evidence supporting this cosmological model. Early surveys like the Sloan Digital Sky Survey (SDSS; York et al., 2000) and the Dark Energy Survey (DES; Melchior et al., 2015) have provided compelling evidence by revealing strong similarities between the large-scale structures observed in the Universe and those predicted by dark-matter-only simulations. These observations have cemented the λCDM model as the prevailing framework for understanding the Universe's structure and evolution.

Yet, how do we find direct evidence of hierarchical galaxy formation within galaxies themselves? Stellar halos, which retain the signatures of gravitational interactions and satellite accretion events, are critical to unveiling the accretion history of galaxies. Additionally, obtaining kinematic measurements of this component provides crucial insight into the origins of the resident populations within stellar halos. In the course of this thesis, we will explore the role of stellar halos in tracing the complex processes of galaxy formation and assembly and we will focus on kinematic measurements in the stellar halo of NGC 4945 with resolved stars to shed light on the processes that shape these extended galactic structures.

## 1.2 Theory of Stellar halos

The origin of the stellar halo has been a long-standing problem in astronomy, with early theories divided between two opposing models: the monolithic collapse scenario proposed by Eggen et al. (1962) and the chaotic accretion model of Searle & Zinn (1978). In their work, Searle & Zinn (1978) analyzed the metallicity distribution of globular clusters in the MW at galactocentric distances r>8 kpc and found no radial dependence. The lack of a metallicity gradient led them to propose that those globular clusters formed in distinct small "protogalaxies" which later merged to create the Galactic halo. This was an observational clue in favor of the hierarchical galaxy formation model.

The discovery of the Sagittarius dwarf galaxy (Ibata et al., 1994), which is currently being disrupted by the MW, motivated subsequent studies within the hierarchical framework to focus on the fossil evidence left by a satellite galaxy disruption (Johnston et al., 1995).

Each satellite carries its own chemical and dynamical information, which is deposited into the host galaxy, acting as a fossil record that we aim to trace to construct the list of progenitors of the host galaxy. Galaxies like the MW have undergone multiple merger events at different epochs. The tidal disruption of these satellites is predicted to form the diffuse stellar halo of a galaxy (Bullock et al., 2001; Bullock & Johnston, 2005; Cooper et al., 2010). For MW-like galaxies, this is characterized by having a very low surface brightness (SB, $\mu_V \geq 28$), containing a small fraction of the main galaxy's light – approximately 1-10 percent – and extends to approximately 100-200 kpc around the galaxy (Bullock & Johnston, 2005; Purcell et al., 2007).

Identifying all the satellite progenitors has been a major challenge developed over many years, starting with the pioneering work of Helmi & White (1999). Helmi & White (1999) developed a model to study the phase-space distribution of halo stars, focusing on the debris left by disrupted satellites. The phase-space framework combines both the positions and velocities of stars, providing a comprehensive view of their dynamical state. Initially, the debris from a disrupted satellite forms a coherent structure with high density in phase-space. Over time, the stars undergo phase mixing, where their spatial distribution becomes more diffuse. While the debris loses structure in configuration space, correlations in velocity space are partially retained. This dual evolution underscores how remnants of satellite galaxies contribute to the formation of the diffuse stellar halo, with more recent accretion events leaving visible substructures in the galaxy's outskirts, as they are not completely mixed (Bullock et al., 2001; Bullock & Johnston, 2005; Bell et al., 2008; Johnston et al., 2008; Cooper et al., 2010; Vera-Casanova et al., 2022).

Progress in theoretically understanding galaxy formation and evolution has been facilitated by advancements in simulations of galaxy formation in a cosmological context. Numerical simulations of MW-like galaxies initially focused mainly on the evolution of tidal stripping of merging systems. Johnston et al. (1996) used a MW model, consisting of a disk with a spherical halo, and used numerical simulations to model the disruption of satellites by the MW, focusing on how debris from these interactions evolves over time and found that this debris can remain aligned in a tidal stream close to the parent satellite's original orbit. Other theoretical studies allowed us to characterize the mass and orbits of progenitor satellites or the potential of the galaxy they are orbiting, using semianalytic models (Johnston et al., 1999) or N-body simulations (Helmi & White, 2001). These works did not focus on the evolution of galaxies but on characterizing the properties of the satellites that these galaxies could have accreted. In particular, they aimed to link the Sagittarius stream, discovered in those years, with the progenitor satellite galaxy. These models are computationally inexpensive and physically simple, enabling them to resolve even small infalling dwarf galaxies.

Modeling the stellar halo in a cosmological context is not a trivial task; it requires information on the frequency of satellites and the phase-space structure of particles. Moreover, the resolution achieved at the time did not allow for this. For instance, Sagittarius is the largest contributor of substructure with the mass on the order of $10^8 M_\odot$(Law et al., 2005), so simulations could not resolve such an object with more than a few hundred particles. This type of simulation is more computationally expensive and intensive, allowing only the examination of a handful of halos. Even when it became possible to do so, these simulations only followed the dark matter component of each galaxy, not the stellar one (Helmi et al., 2003).

Analytic and semi-analytic approaches permitted the construction of various halos and the tracking of stars separately from dark matter (Bullock et al., 2001), but it was not possible to obtain details of the phase-space structure accurately. Bullock & Johnston (2005) used a hybrid approach, combining semi-analytic models with dark matter-only N-body simulations to model accretion events contributing to the formation of stellar halos in MW-like galaxies. Their work was the first focused on stellar halo formation and showed abundant substructures at distances of 30-60 kpc and beyond (as shown in the top panel of Fig. 1.2), as it is expected from a hierarchical stellar halo formation. The stellar halo view in Fig. 1.2 shows a recent disruption of a satellite (1.5 Gyr look-back time) and the residue of this event is seen as the bright plume in the northwest of the halo (upper left in the figure) down toward the halo center and the bright feature just to the southwest of the halo center is also associated with the same disruption event. They also found that the stellar halos form from the inside out, with the majority of mass coming from the most massive accretion events. The bottom panel of Fig. 1.2 plots the radial velocity $V_r$ versus radius, which is a 2D slice of the full 6D phase-space and shows a radial color profile reflecting the inside-out

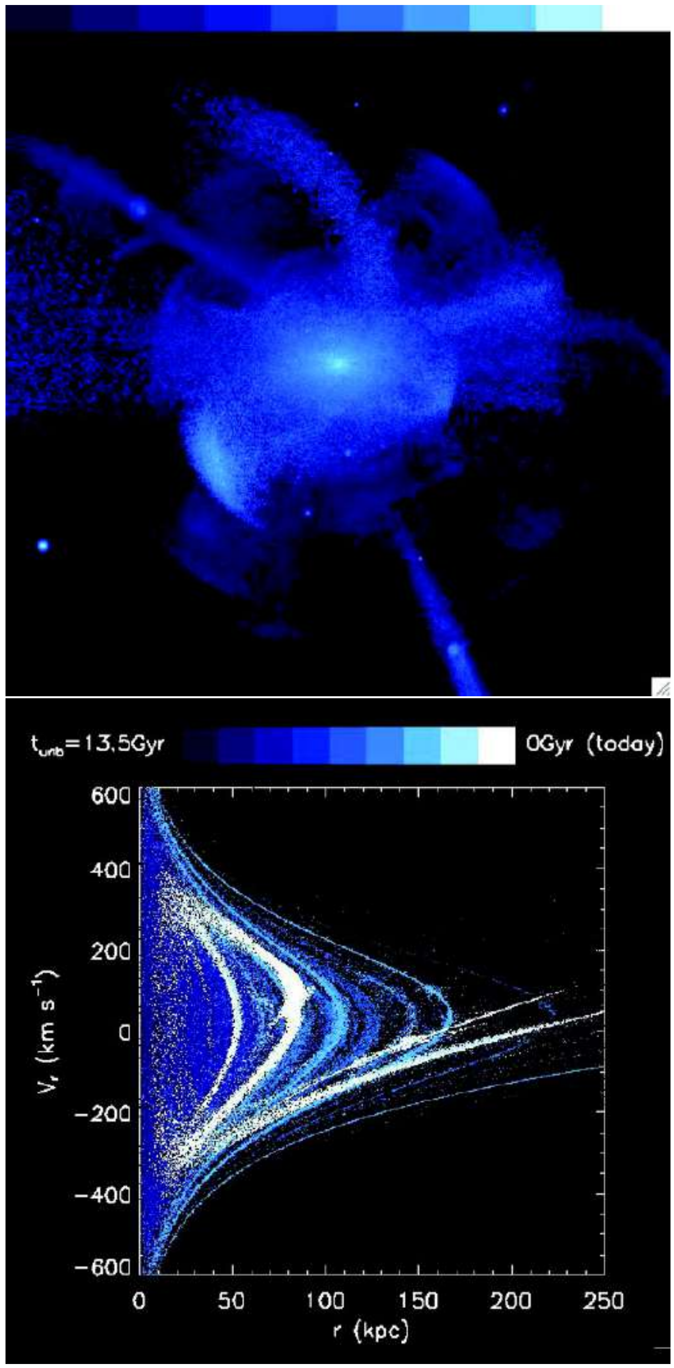


Figure 1.2: Upper: External view of a simulated halo in a box of 300 kpc. The color code indicates surface brightness from 23 mag arcsec$^{-2}$ (white) to 38 mag arcsec$^{-2}$ (dark blue/black). North is up and east is to the right. Lower panel: Radial phase-space diagram ($V_r$ vs. r relative to the host halo center). The color code represents the time each particle became unbound to its parent satellite. White points are either bound or became unbound in the last 1.5 Gyr. Figures extracted from Bullock & Johnston (2005).

formation of the stellar halo. The color code indicates the time the particle became unbound from its original satellite. The work of Bullock & Johnston (2005) also found that surviving dwarf satellites are accreted much later ($\sim$3–5 Gyr look-back) than their destroyed counterparts and that the most massive satellites that survive at $z = 0$ tend to be accreted even later because the destructive effects of dynamical friction are more important for massive satellites. These can offer constraints on the late-time accretion histories of galaxies, validating the hierarchical cosmological model on small scales.

Abadi et al. (2006) used a set of cosmological simulations and defined the "in situ" stars, which were formed in the most massive progenitor and the "accreted" stars, which were formed in progenitors that merged with the main galaxy. They found that in situ stars dominate the inner 20 kpc of their galaxies (mainly the young stars in the disk) but some are present beyond that distance, while accreted stars make up preferentially the central spheroidal component and dominate the outer regions of the galaxies. In addition to a dominant accreted stellar halo component, other theoretical works predict a dual origin of halo stars. Zolotov et al. (2009) use four high-resolution cosmological SPH + N-body simulations to analyze the formation of stellar halos in four disk galaxies and found that both accretion and in situ star formation contribute to the inner regions of stellar halos. They found that most of the in situ halo stars were displaced from their central original locations into the halos as a result of mergers, the so-called disk kicked out stars. They linked the merger histories of the galaxies with the properties of the in situ and accreted populations in stellar halos, showing that the two galaxies with quiescent merger histories have a higher fraction of in situ halo stars compared to those with active recent mergers. This is likely because such galaxies with more active recent accretion histories lead to more massive accreted halos, hence the relatively low presence of in situ halo stars. Purcell et al. (2010) arrived at a similar result, but with the difference that minor mergers were responsible for heating the disk, leading to the subsequent ejection of some of its stars into the diffuse stellar halo. They also suggested that these ejected disk stars occurred in the same event in which the satellite deposited its material into the outer stellar halo. The disk kicked-out stars (disk heated stars) could contribute about 20% to the inner halo (Tissera et al., 2013).

Cooper et al. (2015) added two more categories to the definition of in situ halo stars: those formed from smoothly accreted gas and those that formed in gas streams stripped from infalling satellites. They found that in situ stars dominate the stellar halo out to 20 kpc They also found that the majority of in situ halo stars belong to the stripped gas category.

Hydrodynamical simulations of stellar halo formation provide predictions for the global properties of stellar halos – such as stellar density profiles, metallicity gradients, and the relative contributions of in situ and accreted stars – across host galaxies with a broad range of masses and merger histories (Font et al., 2011; Tissera et al., 2014). New hydrodynamical simulations, such as IllustrisTNG50 (Pillepich et al., 2019; Nelson et al., 2019) or Auriga (Grand et al., 2017), yield insight into the global structure and substructures in the stellar halos. The presence of coherent debris structures within halos gives us information about the hierarchical formation of galaxies, offers clues about the nature of smaller galaxies in the past, and constrains the accretion history of the parent galaxy. Additionally, the collective interpretation of debris can provide sensitive constraints on the distribution of mass in the DM halo. These hydrodynamical simulations highlight the various mechanisms – accretion and kicked-out stars from the inner galaxy – that contribute to the formation of simulated stellar halos.

Using these simulations, it has been shown that the in situ halo should be more metal-rich than the accreted halo, as its stars were formed in the main, more massive galaxy (Monachesi et al., 2019), and it is predicted to be more prominent along the major axis of the galactic disk (Pillepich et al., 2015;

Monachesi et al., 2016b). The presence of these in situ halo stars complicates the characterization of the accreted stellar halo, leading to uncertainties and difficulties in inferring the merger history of galaxies. The extent of this population varies dramatically among models, being dominant only in central regions, less than 11 kpc for some, or up to 30 kpc for others (Zolotov et al., 2009; Cooper et al., 2015; Pillepich et al., 2015; Wright et al., 2023), underscoring the fundamental limitations of these models as they rely on different prescriptions for star formation and feedback below their respective resolutions. Nevertheless, simulations provide valuable datasets for understanding the distinctive signatures left by different formation mechanisms in simulated stellar distributions and for suggesting how the true contribution of stars formed in situ, kicked out, or accreted might be assessed from observations (Zolotov et al., 2010).

These differences motivate a detailed observational characterization of stellar halos that allows us to constrain the models and thus improve our interpretation of the accreted stellar halo and the merger history of a galaxy.

## 1.3 Stellar Halos: Observations

Observing stellar halos presents a significant challenge due to their extremely low surface brightness ($\mu_V \geq 28\,\mathrm{mag/arcsec^2}$ Bullock & Johnston, 2005), which is even fainter than the night sky itself. However, stellar halos are critical for understanding galactic evolution and the processes of mass assembly.

With the generation of large statistical samples of galaxies across broad sections of the sky and at different redshifts (Galaxy Zoo and CANDELS; Darg et al., 2010; Grogin et al., 2011), galaxy mergers appear as a catalyst that could describe many properties of galaxies, such as the growth of stellar bulges (Bell et al., 2017; Gargiulo et al., 2022), the growth of the central supermassive black holes, the triggering of quasars or the formation of elliptical galaxies (e.g., Springel et al., 2005b,a; Hopkins et al., 2006), among others. However, obtaining information on how merger history impacts galactic evolution is still difficult.

Nearby galaxies offer excellent opportunities to explore merger histories of galaxies more extensively, as their stellar populations can be resolved and their properties can be investigated in detail. Within the Local Group (LG), the two most massive and studied galaxies are the MW and its closest large neighbor, M31. The MW is currently undergoing interactions with its major satellites, the Large and Small Magellanic Clouds, along with the Sagittarius dwarf galaxy (Ibata et al., 1994), leading to various effects ranging from wrapping the disk (Laporte et al., 2018) to the building up of the stellar halo (Helmi & White, 1999; Bullock & Johnston, 2005; Bell et al., 2008).

The advent of large-area, all sky surveys, such as the Sloan Digital Sky Survey (SDSS; York et al., 2000) and the Two Micron All-Sky Survey (2MASS) has greatly enhanced sensitivity for star-count studies, enabling detailed studies of substructure within the MW. Many new tidal structures were discovered using SDSS data, such as the Palomar 5 stream, the Monoceros ring, the orphan stream, and the Virgo overdensity. These surveys have revealed halos extending beyond 100 kpc from the Galactic centers, with rich substructure in the form of streams, tidal tails, and other remnants of past accretion events (Belokurov et al., 2006; Ibata et al., 2007).

The Gaia spacecraft (Gaia Collaboration et al., 2016, 2018, 2021) has revolutionized our understanding of the MW by providing precise measurements, including parallax distances, proper motions, and radial velocities of more than one billion stars. These measurements have enabled the differentiation of stars belonging to the disk and halo based on their kinematics, leading to the discovery of new halo

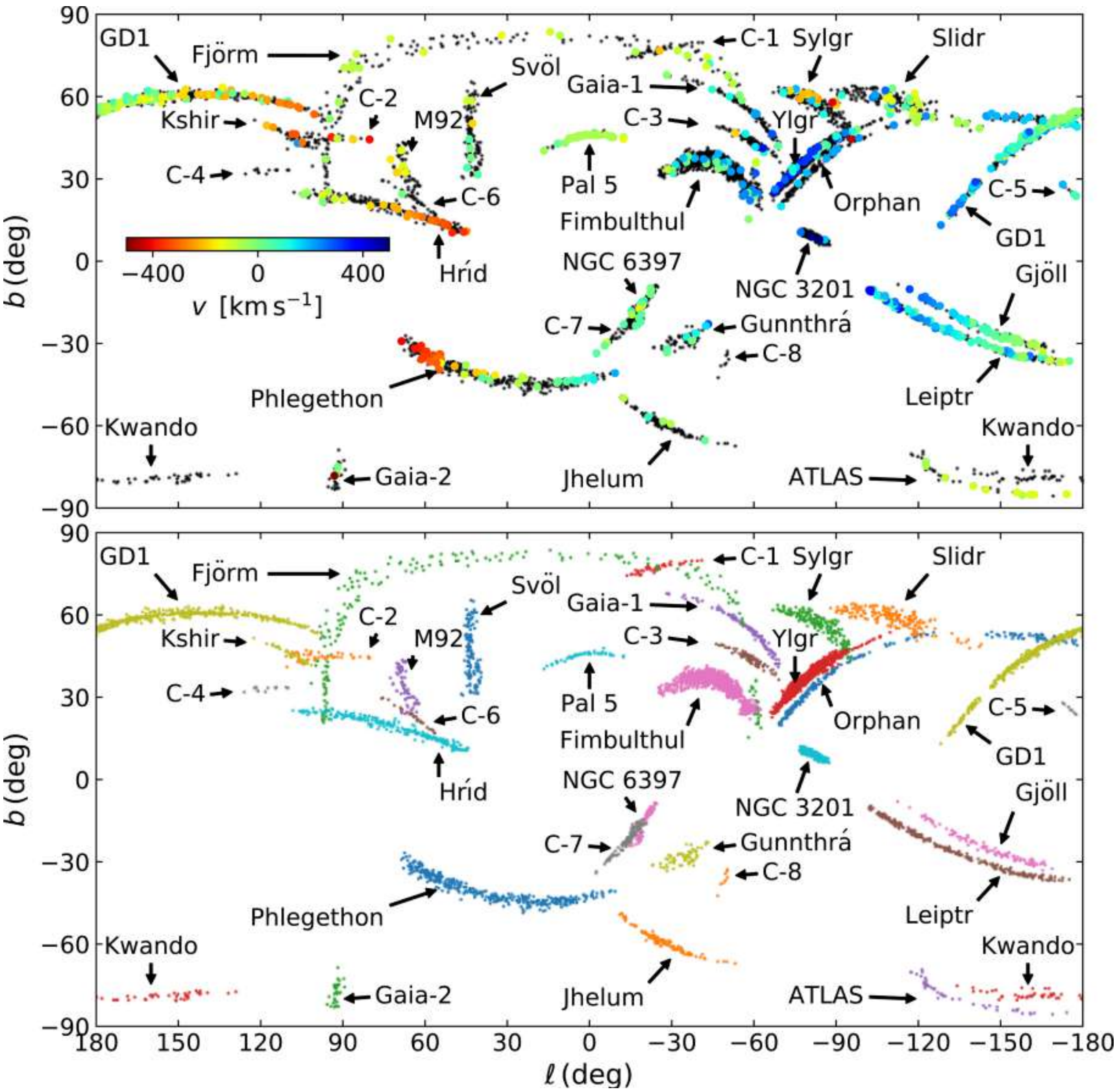


Figure 1.3: (Top) Sky distribution of the 685 radial velocity measurements of the Gaia DR2 sample (Gaia Collaboration et al., 2018). (Bottom) Sky distribution of 5960 Gaia stars in different streams color-coded to allow for easier visual discrimination in sky regions where they overlap (Ibata et al., 2021).

streams and substructures (see Fig. 1.3). Notably, the discovery of 'Gaia-Enceladus' revealed halo stars on radial orbits and high metallicities, which sheds light into the origin of the chemically distinct 'thick disk', whose progenitor, a dwarf galaxy, would have had a stellar mass of $\sim 6 \times 10^8$ $M_{\odot}$and was accreted approximately 10 Gyr ago (Helmi et al., 2018; Belokurov et al., 2018).

Similarly, the proximity of M31 allows for detailed observations of its entire stellar halo through projects like PAndAS (Pan-Andromeda Archeological Survey, McConnachie et al., 2009), albeit with less detailed phase-space information compared to the MW. Through MegaCam on the Canada-France-Hawaii Telescope (CFHT), PAndAS imaged the stellar halo of M31 out to 150 kpc, covering more than 300 square degrees in 4 years, revealing that M31 possesses almost double the satellites at all galactic radii within this radius as well as other tidal structures in comparison to the MW (e.g. McConnachie et al., 2018). With PAndAs data, Ibata et al. (2014) show that the most metal-rich populations are more present in stream structures; interestingly, the most metal-rich stars are those associated with the "Giant Stellar Stream". The substructures and the metallicity map are shown in Figure 1.4. Ibata et al. (2014) also found a metallicity gradient from -0.7 to -1.5 from the inner 30 kpc to 150 kpc of distance, with the smooth halo being 0.2 dex more metal-poor than the full sample (considering the populations that are associated to distinct substructures), and they also estimated the total stellar mass of the M31 smooth stellar halo at $8 \times 10^9$ $M_{\odot}$.

The Spectroscopic and Photometric Landscape of Andromeda's Stellar Halo (SPLASH, Gilbert et al., 2012) survey consists of broad and narrow-band imaging and spectroscopy of Red Giant Branch (RGB) stars in line-of-sight (LOS) ranging in distance from 2 kpc to more than 200 kpc from the Andromeda's center. The SPLASH survey revealed that M31 experienced a major merger (log $M_* \sim 10.3$) approximately 2-4 Gyr ago (Hammer et al., 2018; D'Souza & Bell, 2018), impacting on M31's properties: its disk was thickened to a nearly 1 kpc scale height (Dalcanton et al., 2015) and these intermediate-age disk populations posses high-velocity dispersions of $\sim$90 km $s^{-1}$ (Dorman et al., 2015). Moreover, the entire disk appears to have undergone a burst of star formation just at the final stage of the massive merger that M31 was experiencing, after which its star formation began to decrease until now (Williams et al., 2015).

Beyond the MW and M31, LG dwarf galaxies have also been studied to decipher their stellar halos. Most of the dwarf galaxies studied are satellites of the MW or M31. The latest study was conducted on 45 ultra-faint dwarf galaxy satellites of the MW using RR Lyrae stars, as tracers of the old stellar populations, and shows that these galaxies have very extended stellar populations, belonging to the stellar halo (Tau et al., 2024).

Since observing the stellar halos of galaxies is extremely challenging due to their low surface brightness, multiple approaches have been developed to measure and characterize them. On one hand, integrated light observations provide a panoramic view of galaxies, offering a powerful tool to study their structures and faint features. By the early 2000s, streams, and tidal features had already been identified in spiral galaxies beyond the LG, including NGC 253 and NGC 5236 (Malin & Hadley, 1997), NGC 5907 (Martínez-Delgado et al., 2008), NGC 4013 (Martínez-Delgado et al., 2009), and M94 (Trujillo et al., 2009). These discoveries naturally led to systematic efforts to detect such structures in nearby, MW-like spiral galaxies. One such effort was conducted by Martínez-Delgado et al. (2010), who carried out ultra-deep, wide-field imaging of eight isolated spiral galaxies using small telescopes. Their observations achieved surface brightness limits of 28.5 mag/arcsec$^2$, revealing a remarkable diversity in the morphological characteristics of stellar streams and other faint features. They also captured surviving satellites in the process of tidal disruption, findings that aligned closely with predictions from cosmological simu-

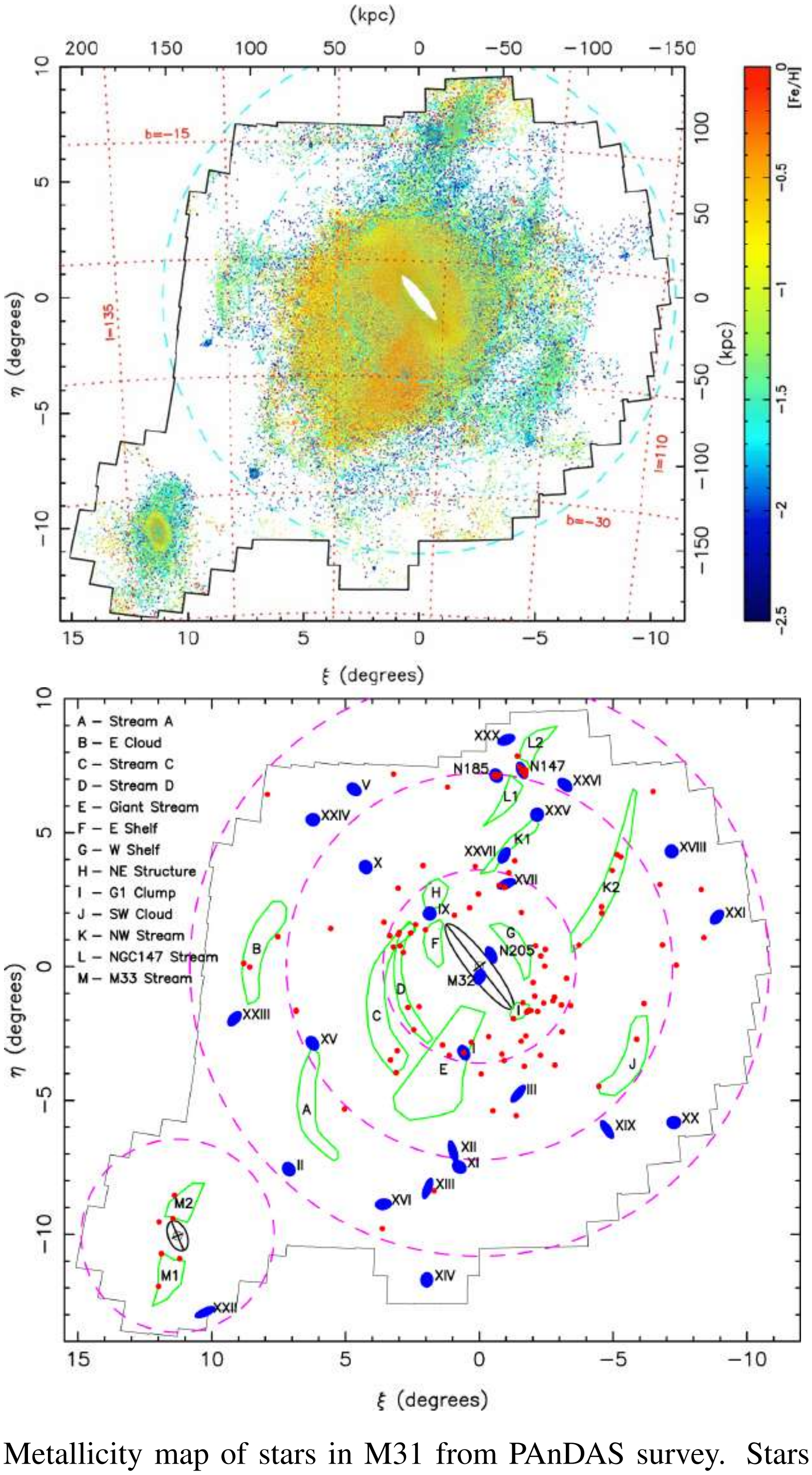


Figure 1.4: Upper: Metallicity map of stars in M31 from PAnDAS survey. Stars were selected such that $(g-i)_0 < 1.8, -2.5 < [Fe/H] < 0$ and $i_0 < 23.5$. this map reveals the multiple accretion events that M31 has experienced (Ibata et al., 2014). Lower panel: Spatial positions of stellar substructures (green polygons), globular clusters (red dots), and satellite dwarf galaxies (blue ellipses) detected by McConnachie et al. (2018) in M31. The dashed circles correspond to projected radii of 50 kpc, 100 kpc, and 150 kpc from M31, and 50 kpc from M33.

lations. Moreover, integrated light observations allow for statistical studies of large galaxy samples. By stacking observations of similar galaxies, these studies can derive average properties of stellar halos and faint structures, as demonstrated in large-scale surveys like the Sloan Digital Sky Survey (e.g., D'Souza et al., 2014).

Using multi-band observations, color mass-to-light ratio relations can measure the stellar halo mass, but this requires assumptions regarding the stellar populations present, as they do not resolve individual stars. However, this technique is affected mainly by two effects: i) scattered light originating from the galaxy's center, as well as stars or other compact sources within or near the field of view (FoV, de Jong, 2008) and ii) the presence of foreground Galactic cirrus, which will inevitably appear in deep observations reaching fainter surface brightness levels ($\mu_V \geq 28\,\mathrm{mag/arcsec^2}$), leading to the appearance of false substructure-like features (de Jong, 2008; Cortese et al., 2010; Hodges-Kluck & Bregman, 2014).

The Dragonfly Telephoto Array (Dragonfly; Abraham & van Dokkum, 2014) is a robotic refracting telescope specifically designed to minimize reflections and detect low surface brightness emission. Its large field of view ($2^\circ \times 3^\circ$) allows for panoramic imaging of each targeted galaxy. Using Dragonfly, Merritt et al. (2016) obtained extremely deep surface brightness profiles, reaching levels of 31–32 mag/arcsec$^2$, for eight nearby spiral galaxies with absolute magnitudes $M_B < -19.3$ and distances of 7–18 Mpc. These profiles extended out to semi-major axis distances of 20–70 kpc. Interestingly, stellar halos were not detected in three out of the eight galaxies, contrary to predictions from simulations. More recently, Gilhuly et al. (2022) analyzed 12 nearby edge-on spiral galaxies (at distances $d < 25$ Mpc) spanning a wide range of stellar masses ($10^{9.68}$ to $10^{10.88}$ $M_\odot$). The edge-on orientation minimized contamination from the galactic disk, enabling a clearer exploration of stellar halos. They found a broad range in stellar halo mass fractions and identified a weak positive correlation between stellar halo mass fraction and total stellar mass, particularly in the halo-dominated regions beyond 20 kpc. This correlation became stronger when the stellar halo mass was measured beyond five half-mass radii. Their measurements of stellar halo mass fractions were consistent with studies based on resolved stellar populations, such as those by Harmsen et al. (2017).

On the other hand, discrete tracers like globular clusters (GC), planetary nebulae (PN), and resolved individual stars provide alternative approaches for studying stellar halos. Early spectroscopic and photometric studies, such as van den Bergh (1969), found that GCs in M31 are generally more metal-rich on average than those in the MW. They also noted that the GCs in the Fornax dwarf spheroidal galaxy appeared to have very low metallicities compared to those in the MW and M31, demonstrating the importance of GC systems in reflecting substantial differences that can provide hints about the formation and chemical enrichment histories of their parent galaxies (Brodie & Strader, 2006). GCs have been especially important for studying distant systems whose stars are unresolved but whose GCs can be observed with integrated light spectroscopy.

PNs are another important tracer, often used to map stellar halos or differentiate them from the surrounding intracluster light (ICL) (e.g. Peng et al., 2004; Hartke et al., 2022). Overdensity patterns of PNs can be associated with an accretion event, reflecting incomplete phase-space mixing of a disrupted galaxy (Longobardi et al., 2015). While GCs and PNs offer the advantage of brightness, they provide sparse sampling and preferentially trace specific stellar populations rather than the overall halo.

Resolved stellar populations, though observationally intensive, allow reaching fainter surface brightness levels ($\mu_V \sim 32-34$ mag/arcsec$^2$, Harmsen et al., 2017), overcoming limitations such as scattered light and Galactic cirrus. Additionally, resolved stars provide insight into the metallicity and age distributions of the populations that make up the stellar halo. Ground-based wide-field telescopes, for instance, offer panoramic views of stellar halos resolving the brighter magnitudes of RGB stars. This capability allows the detection of overdensities in the outskirts of galaxies, estimation of halo masses, characterization of halo profile shapes, and insights into stellar halo population properties (see e.g. Barker et al., 2009; Greggio et al., 2014). However, measurements of RGB star colors in stellar halos are less precise due to challenges like crowding and contamination from unresolved background galaxies (Bailin et al., 2011).

In contrast, surveys using the *Hubble* Space Telescope (HST) achieve unparalleled star-background galaxy separation for galaxies up to 10 Mpc (e.g., Rejkuba et al., 2009; Monachesi et al., 2013; Peacock et al., 2015; Cohen et al., 2020; Rejkuba et al., 2022). HST's ability to avoid seeing degradation not only allows it to resolve stars in more distant galaxies but also provides a unique advantage for studying stellar populations with greater accuracy and depth. The first studies of stellar halos in spiral galaxies outside the LG using resolved populations were conducted with HST by Mouhcine et al. (2005a,b,c). Using the Wide Field Planetary Camera 2 (WFPC2), they imaged the stellar halo populations of eight spiral galaxies at projected distances of $\sim$10 kpc from the galactic centers, resolving their RGB stars. They found that the color of the RGB stars in intrinsically bright galaxies is redder than in faint galaxies, implying that the more luminous spiral galaxies also have more metal-rich stellar halos. However, their analysis was limited to a single field per galaxy, restricting their ability to robustly correlate the properties of the stellar halo population to the parent galaxy.

The Galaxy Halos, Outer disks, Substructure, Thick disks, and Star clusters (GHOSTS) survey (Radburn-Smith et al., 2011) was later established to analyze the stellar populations of nearby disk galaxies. Using deep HST images, GHOSTS observed 16 edge-on galaxies up to $\sim$17 Mpc, covering a range of masses ($V_{rot} = 80 - 260$ km s$^{-1}$), making it the largest HST program dedicated to resolving stars in the outskirts of disk galaxies. Multiple pointings were strategically placed along the major and minor axes of the galaxies, as shown in Figure 1.5, to target RGB stars as tracers of the stellar halo population to study the halo's size, shape, and stellar population properties such as age and metallicity. RGB star colors serve as metallicity proxies, with minimal degeneracy with age at this evolutionary stage (Worthey, 1994). Additionally, the magnitude of the Tip of the RGB (TRGB) is used to measure the distance to the galaxy. However, studying more distant galaxies requires longer integration times because the brightness of RGB stars diminishes. For ground-based telescopes, we also have to consider atmospheric seeing conditions, which limit the angular separation of stars. The image quality of ground-based telescopes is often insufficient to distinguish stars from distant background galaxies.

As part of the GHOSTS survey, Monachesi et al. (2016a) analyzed the median RGB color profiles along the minor axis of six nearby spiral edge-on galaxies and found variations from galaxy to galaxy. The median color, which serves as a proxy for metallicity, showed that color variations reflect variations in the metallicity of the stellar population. Additionally, half of the galaxy sample showed a negative color gradient, while the other half exhibited a rather flat color profile (Figure 1.6). Harmsen et al. (2017) presented density profiles along minor and major axes for the sample analyzed by Monachesi et al. (2016a), measuring the shape of the stellar halos and finding them to be mainly flattened ($c/a \sim 0.5$). Using RGB star counts, they measured the mass of the stellar halo and found a marked relationship between halo mass and metallicity at 30 kpc (measured along the minor axis), showing that more massive stellar halos are more metal-rich. This correlation was also supported by simulations (Deason et al., 2016; Monachesi et al., 2019), as shown in Fig. 1.7.

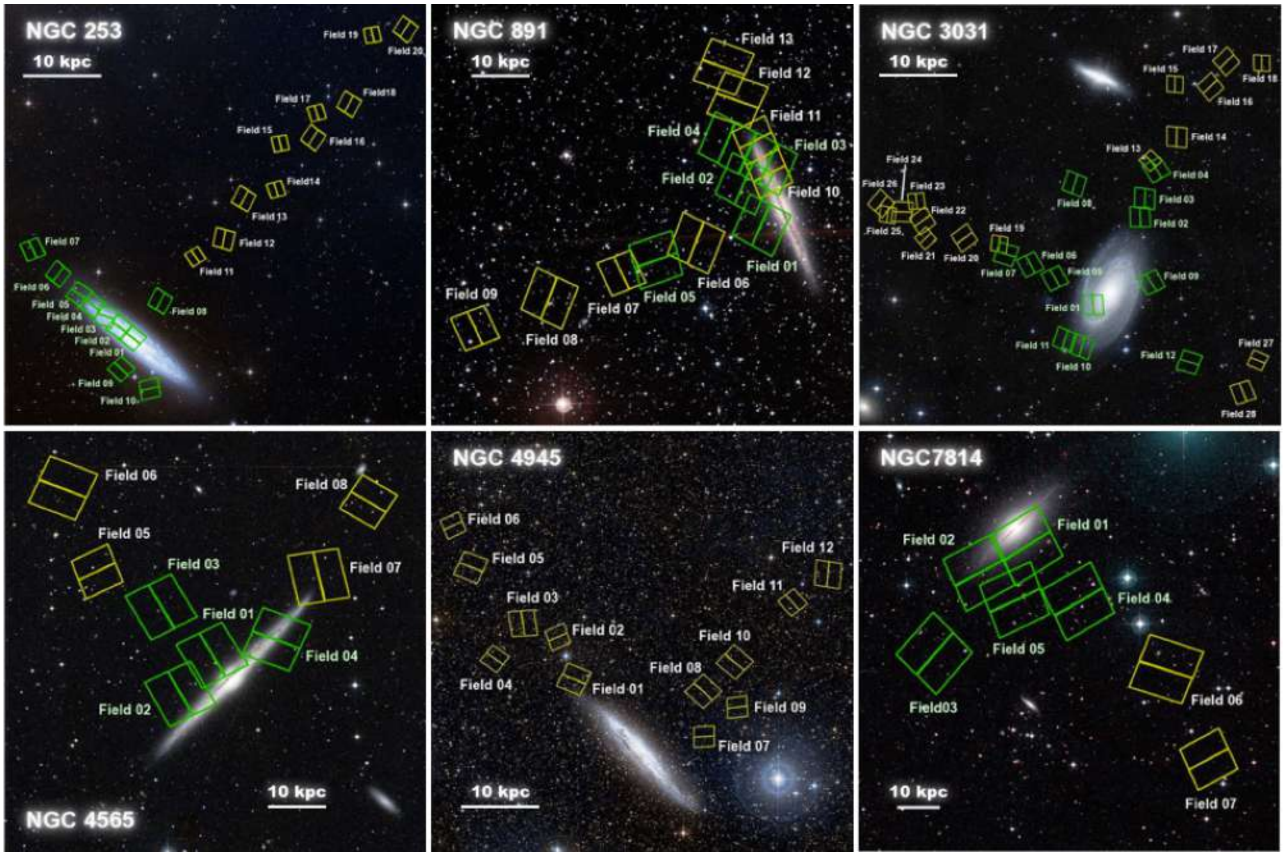


Figure 1.5: Location of the GHOSTS HST ACS/WFC and WFC3/UVIS fields overlaid on DSS colored images of each of six nearby spiral galaxies. Green fields were introduced in Radburn-Smith et al. (2011) whereas yellow fields were presented by Monachesi et al. (2016b). North is up and east is to the left. Figure extracted from Harmsen et al. (2017).

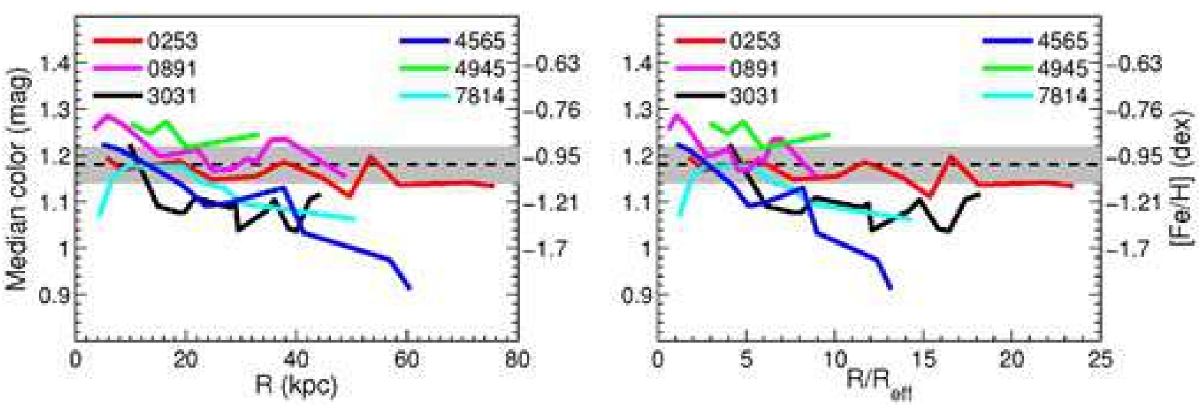


Figure 1.6: Color profiles of the six nearby spiral galaxies along the minor axis as a function of galactocentric distance in kpc (left) and in units of effective radius (right). Figure taken from Monachesi et al. (2016b).

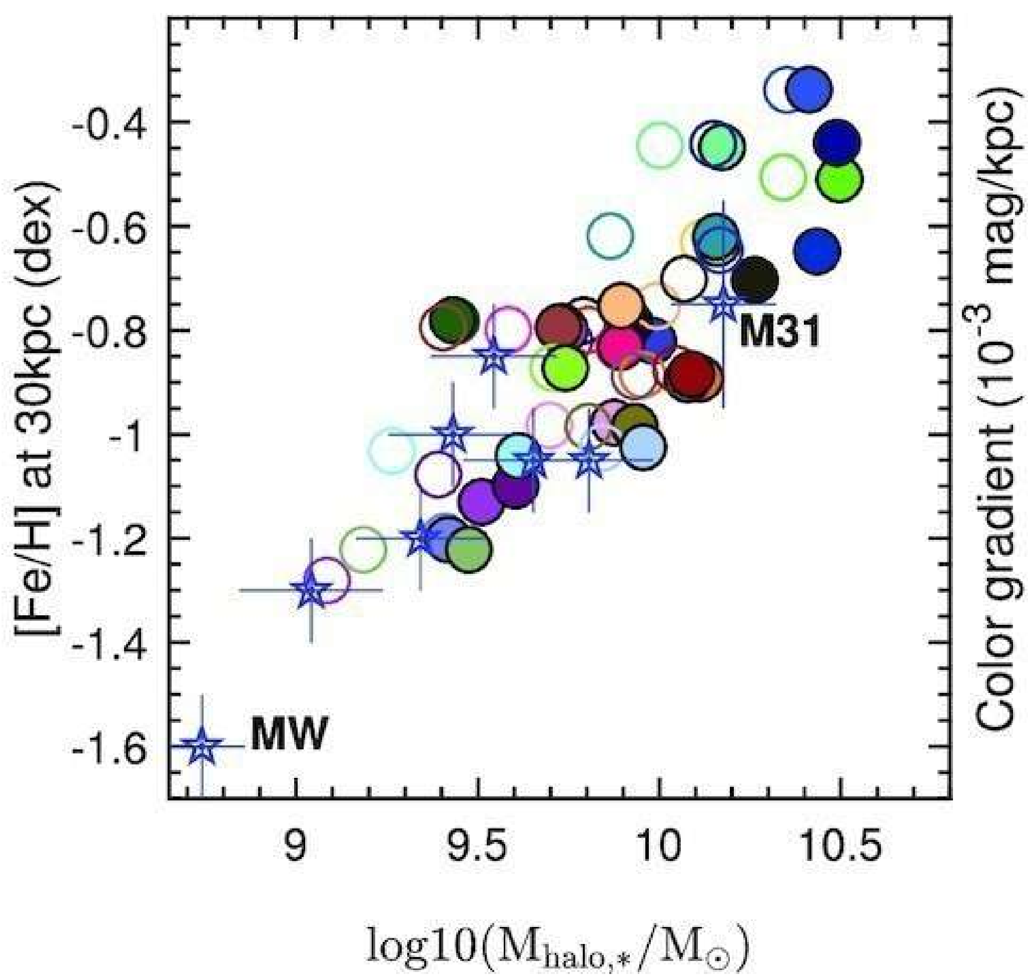


Figure 1.7: Correlation between stellar halo mass and stellar halo metallicity for accreted stellar particles only in each of the Auriga galaxies, labeled by different colors. Data from GHOSTS galaxies, M31, and MW are shown as blue stars. Figure extracted from Monachesi et al. (2019).

## 1.4 Kinematics of Stellar Halos

In addition to photometric studies, kinematic studies are essential for differentiating stellar components, which is hard to achieve using solely photometric data, and inferring the merger history of galaxies. Kinematic studies can reveal the presence of accreted and in situ halo components (Gilbert et al., 2007, 2012; Escala et al., 2019; Gilbert et al., 2022; Dey et al., 2023). Generally, stellar halos are expected to show no net rotation due to the random arrival of accreted satellites (Bullock & Johnston, 2005). However, the accretion of a single massive satellite could produce a rotational signature in the halo, which might even influence the alignment of the disk (Gómez et al., 2017; D'Souza & Bell, 2018). A rotational signature could also be produced by the contribution of disk stars that were kicked out and have now become part of the halo (Pillepich et al., 2015; Monachesi et al., 2016b).

The properties of stellar halos along their major axes, in contrast to the minor axis properties, are particularly insightful in distinguishing between an accreted stellar halo or an in situ dominated component: while rotation in the stellar halo along the major axis could be caused by a single large accreted event or kicked-up disk stars, the detection of zero rotation in the halo unambiguously points to it being of accreted origin. Yet, measuring the velocity of stellar halos of MW-like galaxies outside the LG is extremely hard due to the low surface brightness, which prohibits the analysis of standard integrated spectroscopy. Kinematics of halos in external galaxies have been performed using discrete tracers, such as planetary nebulae or globular clusters (e.g., Pulsoni et al., 2020; Hartke et al., 2022; Pulsoni et al., 2023; Bhattacharya et al., 2023), taking clear advantage of their brightness, but these are sparse sampling and are preferentially tracing special stellar populations compared to the bulk of the stellar halo population, which is indeed traced by the RGBs. Consequently, so far only the diffuse stellar halos of the MW and M31, i.e. only two MW-like galaxies, have been characterized kinematically, from the spectroscopy of their resolved stars.

Our internal vantage point provides us with exquisite detail of the inner halo of the MW, but it is difficult to study the outer halo due to the large distance uncertainties, low stellar densities, and vast survey areas required for even a partial view of the halo. Early kinematics studies found a prograde rotation of about 50 km $s^{-1}$ from the analysis of the line-of-sight velocities of halo globular clusters (Frenk & White, 1980; Zinn, 1985). Carollo et al. (2007) found a dual structure in the stellar halo of the MW consisting of a weakly prograde-rotating inner halo and a retrograde-rotating outer halo of lower metallicity. Deason et al. (2011a), using a sample of 3549 Blue Horizontal Branch (BHB) stars from SDSS with r>10 kpc, also found a dichotomy with a prograde-rotating, metal-rich component, and a retrograde-rotating, metal-poor component. While this study agrees with Carollo et al. (2007) regarding a net retrograde-rotating metal-poor outer halo component, they also found that the outer halo contains a slightly prograde-rotating, more metal-rich component. We now know that the MW has little-to-no (prograde) rotation ($V_{rot} \sim 5-25$ km $s^{-1}$, Deason et al., 2017; Helmi et al., 2018; Bird et al., 2021; Yang et al., 2022), as shown in Figure 1.8, and that the MW accreted an LMC-like progenitor on an extremely radial orbit 8-11 Gyr ago (Belokurov et al., 2018; Helmi et al., 2018). Conversely, our external vantage point provides a global view of the halo of Andromeda. The ability to take spectra of individual stars in the halo of M31 opens up many doors for studying its kinematics, structure, and metallicity. As part of a large spectroscopic survey using the Deep Imaging Multi-Object Spectrograph (DEIMOS) on the Keck II 10 m telescope Gilbert et al. (2006) developed a method to isolate a clean sample of RGB stars in M31 using a combination of spectroscopic and photometric information. The method used 5 diagnostics to

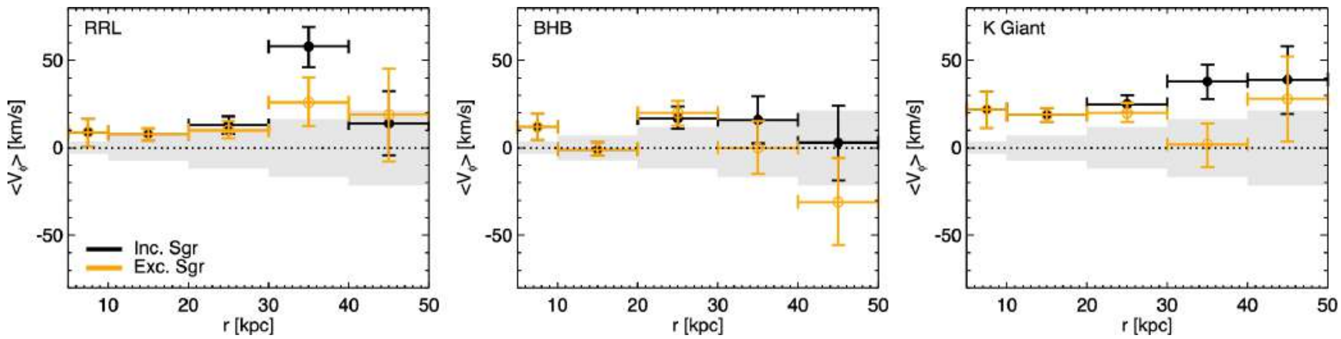


Figure 1.8: Rotation of the stellar halo in Galactocentric radial bins using RR Lyrae, BHB, and K giants stars in the halo of the MW. Black circles show all halo stars and the open orange circles show the rotation when stars likely associated with the Sagittarius stream are removed. The shaded gray region indicates the systematic uncertainty of the SDSS-Gaia proper motions. Figure extracted from (Deason et al., 2017).

isolate RGB stars: radial velocity, photometry with the intermediate-band DDO51 filter, the equivalent width (EW) of the NaI absorption feature, color-magnitude diagram (CMD) position, and a comparison of spectroscopic versus photometric [Fe/H] values. They could find an extended stellar halo out to 165 kpc (in projection) from the galaxy's center. Using this technique Gilbert et al. (2007) analyzed the kinematics of the inner spheroid of M31 with $\sim$1000 RGB stars in the radial range from 9 to 30 kpc along the southeastern axis and found a mean velocity of -287 km s$^{-1}$ and a velocity dispersion 129 km s$^{-1}$ with no evidence of a decrease in the velocity dispersion in this radial range.

Dorman et al. (2012), as part of SPLASH (Section 1.3), found a significant rotation of $\sim$50 km s$^{-1}$ in the spheroid and that the velocity dispersion decreases from about 140 km s$^{-1}$ at 7 kpc to 120 km s$^{-1}$ at 14 kpc. This was confirmed by Gilbert et al. (2018) who found a mild decrease from 108 km s$^{-1}$– in the inner region from 8.2 to 14.1 kpc – to $\sim$80 km s$^{-1}$ in the region from 40 to 130 kpc.

M31 has strong signatures of halo rotation, with $V_{rot} \sim 150$ km s$^{-1}$, see Figure 1.9, out to beyond 40 kpc along the major axis (Ibata et al., 2005; Dey et al., 2023), and together with the large metallicity gradient (extending over 100 kpc), this may indicate that the majority of its halo stars were contributed by one to a few early, relatively massive accretion events (see discussion in Gilbert et al., 2014).

Beyond the two most extensively studied stellar halos (MW and M31), there are no kinematic measurements of diffuse stellar halos in galaxies outside the LG. Kinematic constraints on the stellar halos of MW-like galaxies outside the LG, and in particular of a typical stellar halo, in between the extreme stellar halos of MW and M31, can give us valuable insights into their formation mechanisms, as well as help us constrain the in situ component of the stellar halo.

In this context, the work of Toloba et al. (2016a) represents a pioneering approach to address this gap by obtaining kinematic measurements of the stellar stream in the external galaxy NGC 4449, located at approximately 4 Mpc. Due to this distance, the apparent magnitudes of its RGB stars are too faint to be spectroscopically targeted, and its extremely low surface brightness also precludes the use of integrated light spectroscopy. To overcome these limitations, Toloba et al. (2016a) combined integrated light spectroscopy with spectroscopic techniques for individual stars, paving the way for new methodologies to study the kinematics of faint stellar structures beyond the LG. Toloba et al. (2016a) used deep photometric images from Subaru/Suprime-Cam to select individual stars and star blends in the stellar stream and main body of NGC 4449, using their positions in the $(r-i)$ CMD (Martínez-Delgado et al., 2012).

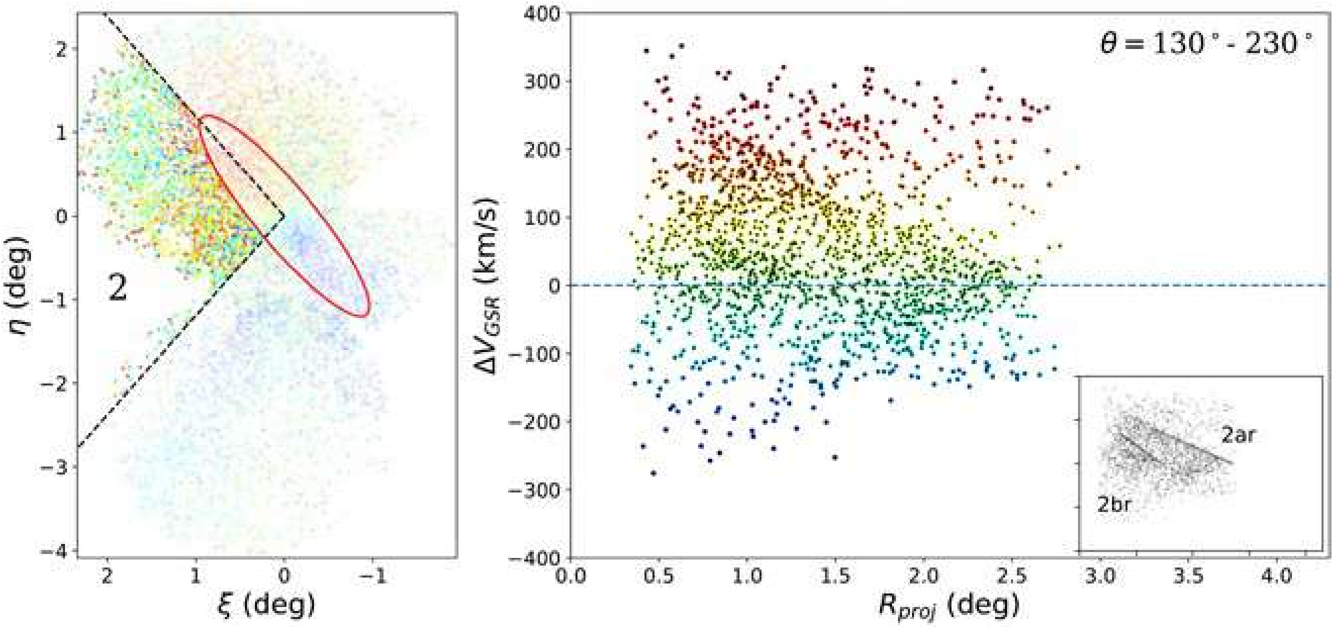


Figure 1.9: LOS velocity-position diagram (right) for the angular zone indicated in the left panel, extracted from (Dey et al., 2023). Velocities are relative to M31's central velocity of $V_{los} = -300$ km $s^{-1}$. Stars within the red ellipse are excluded from the analysis

They targeted objects brighter than the TRGB, $i \leq 24.2$, with colors in the range $-0.1 \leq (r-i) \leq 0.5$, as illustrated in the CMD of NGC 4449's stellar stream Fig. 1.10.

NGC 4449 is a starburst galaxy with a young and intermediate age stellar population, while its stream is mainly composed of older stars, and possibly some intermediate-age Asymptotic Giant Branch (AGB) stars. The selected targets, as shown in Fig. 1.10, are blends of stars rather than individual sources, so the nature of the blends varies between the galaxy and its stream. In the galaxy, blends are typically dominated by a single bright intermediate-age AGB star with a few fainter companions, meaning the brightest star dominates the light. In contrast, blends in the stream primarily consist of RGB stars of similar luminosities, although some intermediate-age AGB stars may occasionally contribute to the blend.

The stream, which spans $\sim 8$ kpc in length and $\sim 1.5$ kpc in width (Martínez-Delgado et al., 2012), fits well within the Keck/DEIMOS spectrograph's field of view ($16.7' \times 5.0'$), enabling efficient placement of slits for both the galaxy and its stream, as shown in the lower left panel of Fig. 1.10. The slits, with a width of $1''$, were carefully placed on selected stars, and spectra were obtained with a wavelength range of $\sim 6500-9000$ Å, at spectral resolution of $R \sim 6000$, and a total exposure time of 8400 s split into four individual exposures of 1200 s and two of 1800 s.

The method consisted in the co-addition of spectra from blends of RGB stars, as well as some individual AGB stars, to enhance the signal-to-noise ratio (S/N), achieving a minimum of $\sim 2\text{Å}^{-1}$ in the calcium triplet (CaT) region. This allowed for reliable measurements of the radial velocities and metallicities. For NGC 4449, radial velocity measurements were obtained from three individual spectra and two co-added spectra (from 19 and 15 individual spectra, respectively), yielding a median velocity of $227.2 \pm 10.7$ km $s^{-1}$. For the stream, they obtained radial velocities for two individual spectra and three co-added spectra (from 15, 16, and 15 individual spectra, respectively), resulting in a median velocity of $225.8 \pm 16.0$ km

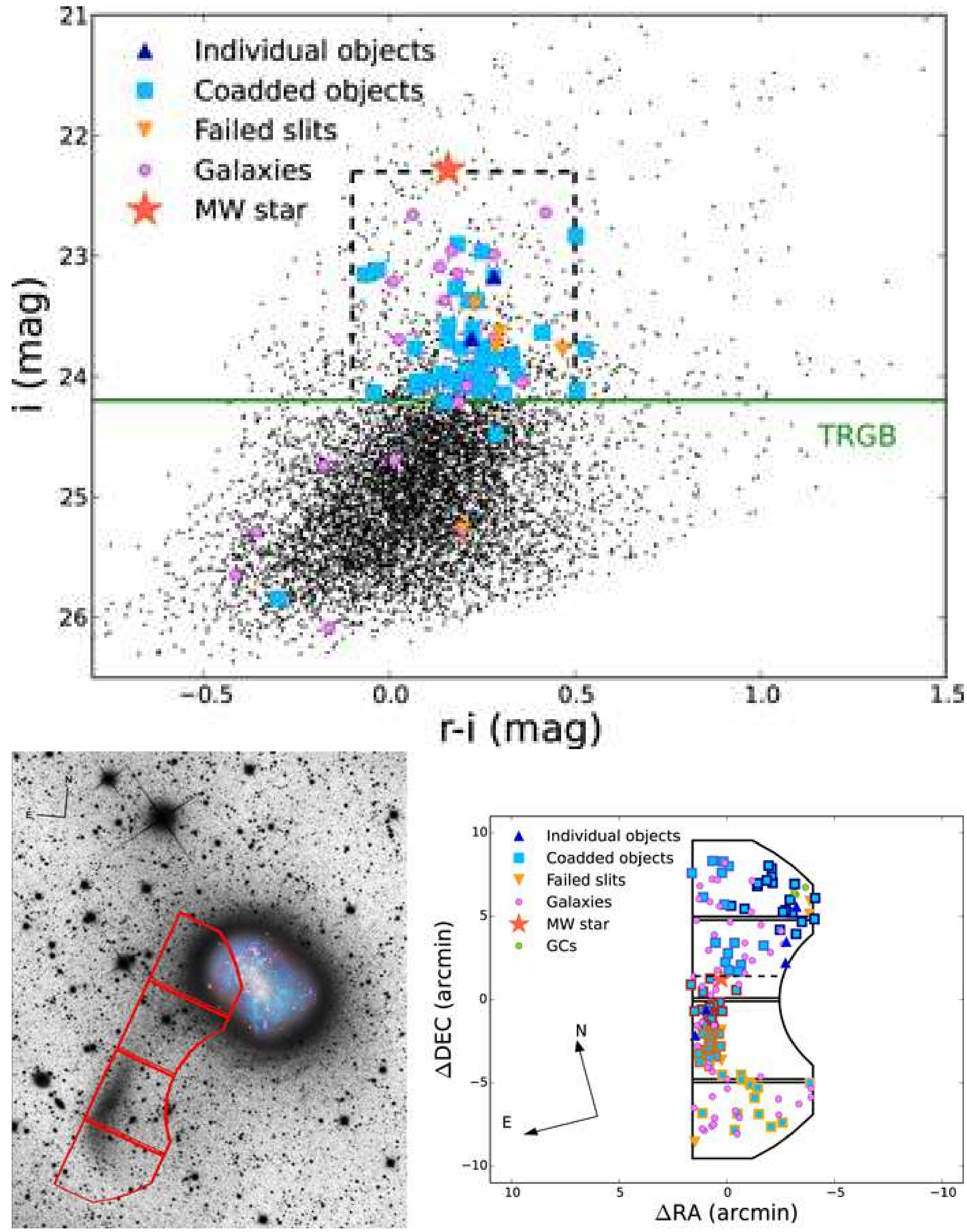


Figure 1.10: Upper panel shows the Subaru/Suprime-Cam CMD of the spectroscopic targets of NGC 4449's stellar stream. Dark blue triangles addressed as individual objects are blends of RGB stars with high S/N to measure their radial velocities. Light blue squares indicate the blends of RGB stars that are coadded in different spatial bins along the stellar stream to increase the S/N to measure radial velocity. The lower left panel illustrated the Keck/DEIMOS slitmask (red) used for the spectroscopic observations overlaid on NGC 4449 and its stellar stream. The lower right panel marks the positions of the target objects. Squares with the same edge color indicate coadded objects. The dashed black line indicates the assumed separation between NGC 4449 and the stellar stream. Figure taken from Toloba et al. (2016a).

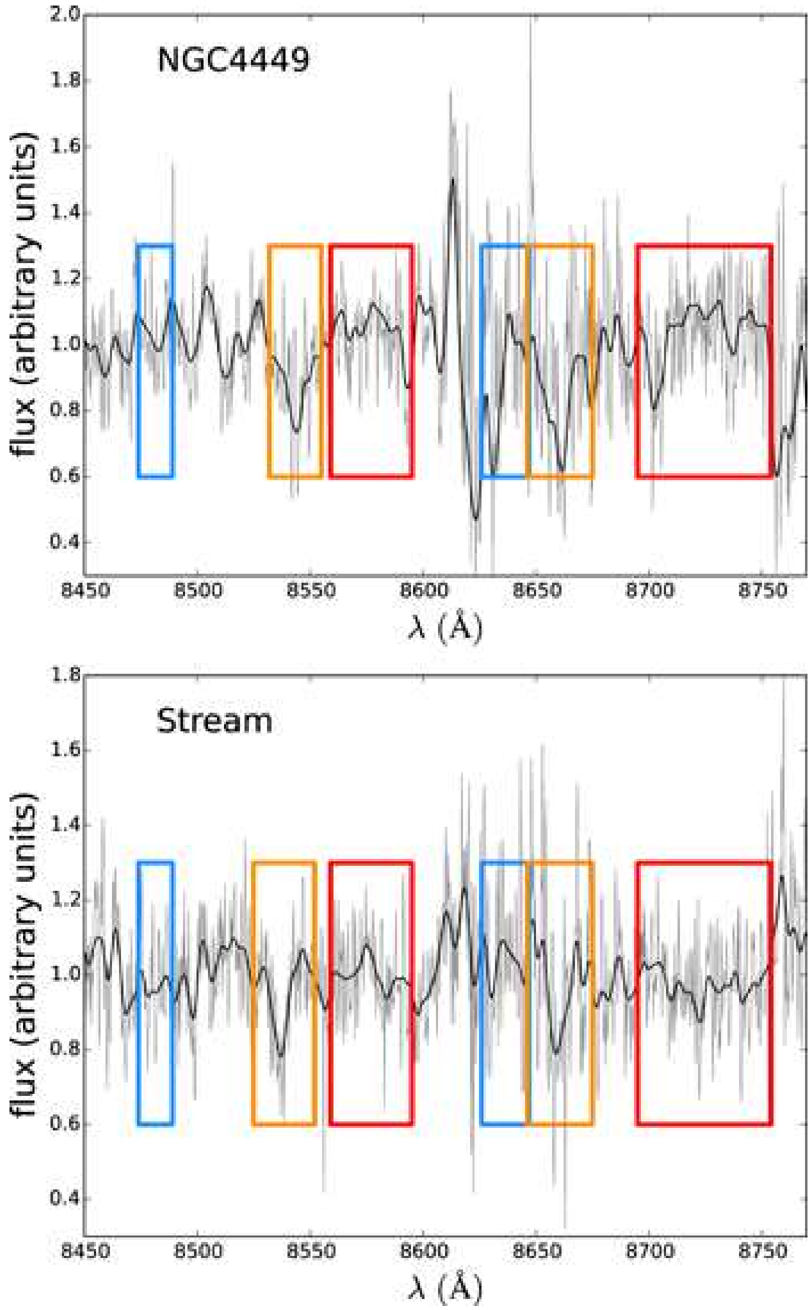


Figure 1.11: Resulting coadded spectra for NGC 4449 and its stream in the CaT region (gray lines). The black lines are the coadded spectra smoothed. Orange boxes mark the two strongest CaT lines at 8562 and 8662 Å, and the blue and red boxes on either side of the CaT line are continuum regions used in the procedure to fit the CaT absorption lines. Figure taken from Toloba et al. (2016a).

$s^{-1}$. These results demonstrated that NGC 4449 and its stellar stream share consistent radial velocities, supporting the hypothesis that the stream is gravitationally bound to the galaxy. They also estimated the stellar metallicity of the stream based on the equivalent width of its calcium triplet lines as shown in Fig. 1.11. In this Figure, the gray lines represent the co-added spectra of NGC 4449 (top panel) and its stream (bottom panel) in the region of the CaT lines. The co-added spectrum for NGC 4449 consists of 31 individual spectra, while the stream's co-added spectrum comprises 51 individual spectra, resulting in S/N values of 5.2 $\text{Å}^{-1}$ and 6.6 $\text{Å}^{-1}$, respectively. The black lines show the smoothed spectra, where the two strongest CaT lines (at 8562 Å and 8662 Å) are highlighted in orange boxes. For the stream, they measured a metallicity of [Fe/H]$= -1.37 \pm 0.41$.

The same technique was applied to measure the first velocity and metallicity of a dwarf spheroidal galaxy beyond the LG, using individual stars (Toloba et al., 2016b). This galaxy, located in the halo of M81, has a heliocentric radial velocity of $-38$ km $s^{-1}$, consistent with the galaxy being gravitationally bound to M81.

As mentioned at the beginning of this Section, kinematic studies of stellar halos are crucial for distinguishing between the in situ and accreted components of the stellar halo. For this reason, the work by Toloba et al. (2016a) paves the way and inspired the development of a methodology to obtain kinematic measurements in the diffuse stellar halo. This thesis seeks to achieve such measurements by determining the velocity and velocity dispersion of the stellar halo of the MW-like galaxy NGC 4945, a galaxy outside the LG, using its resolved stars. In contrast to Toloba et al. (2016a), who employed long-slit spectroscopy to study the stellar stream of NGC 4449, this thesis utilizes Integral Field Spectroscopy to obtain kinematic information of the stellar population in the stellar halo of NGC 4945.

### 1.4.1 Integral field spectrographs

Integral-field spectrographs (IFS, also commonly named integral field unit IFU) are instruments that combine spectrographic and imaging capabilities within a defined wavelength range, allowing for resolved spectra to be obtained across a two-dimensional field-of-view (FoV) from a single exposure. The basic concept behind these instruments is that the signal collected in each spaxel (spatial pixel) in the FoV is transformed into a spectrum. All the resulting spectra are arranged into a datacube (see Figure 1.12), which contains the entire 2D image in the field of view, with $(x, y)$ representing the spatial dimensions, and the third dimension, $\lambda$, representing the wavelength of the spectra. This is an advanced technique that allows the simultaneous acquisition of spectral and spatial information from an extended object, such as a galaxy or group of galaxies, among others.

Regarding IFS technology, different types of IFS use various techniques to divide the field of view, as illustrated in Figure 1.13. The three main types are: those using a microlens array, those using fiber with or without lensets, and those using an image slicer. In the first type, the input image is split by a microlens array. In the second type, the input image is formed at the front surface of a bundle of optical fibers, which direct the light to the spectrograph. Contiguous lenslets placed in front of the fibers collect the light that would otherwise fall in the gaps between the fibers. The last type uses a mirror to segment the input image into several thin slices, reflecting each slice in slightly different directions.

Using the advantage of spectroscopic information at all spatial positions, several surveys have employed IFS to obtain detailed spectral maps that reveal the internal structure and composition of various astronomical objects. One example of these surveys is the ATLAS3D (Cappellari et al., 2011), which

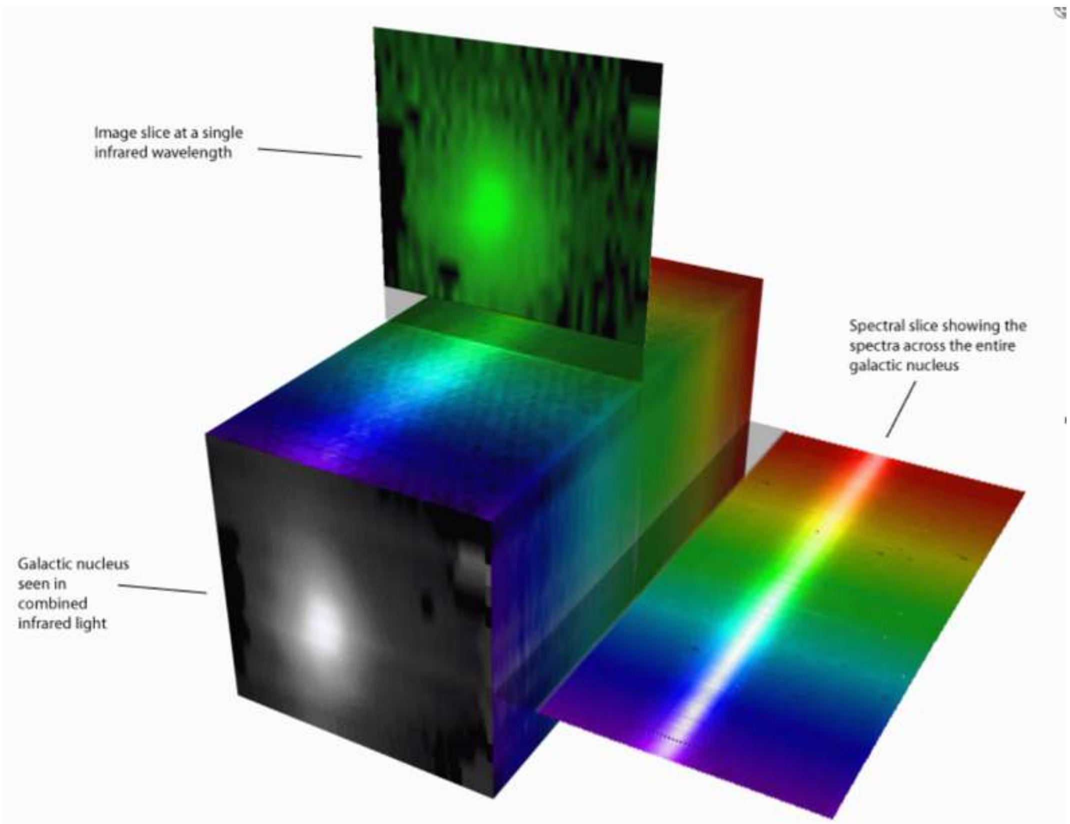


Figure 1.12: The concept of a data cube, with two spatial dimensions and one spectral dimension. Each data cube slice represents a monochromatic image, Each data cube column, along the spectral direction, represents a spectrum. Credit: Stephen Todd (ROE) and Douglas Pierce-Price (JAC).

used the SAURON IFS (Bacon et al., 2001) on the William Herschel Telescope, focusing on understanding the formation and dynamics of 260 galaxies within a selected volume of the nearby universe, z<0.01. Another case is the Calar Alto Legacy Integral Field Area Survey (CALIFA; Sánchez et al., 2012), which was conducted with the Postdam Multi Aperture Spectrograph (Roth et al., 2005) and targeted over 600 galaxies of any type in the Local Universe (z< 0.03). Moreover, the Sydney-AAO Multi-object Integral field spectrograph (SAMI; Croom et al., 2012) uses an array of IFUs to observe over 3000 galaxies across a wide range in mass and environment, below z=0.115, exploring the influence of environment on galaxy evolution. Finally, the Mapping Nearby Galaxies (MaNGA; Bundy et al., 2015), part of the SDSS-IV, also used IFS to map the internal kinematic structure and composition of gas and stars of about 10000 nearby galaxies.

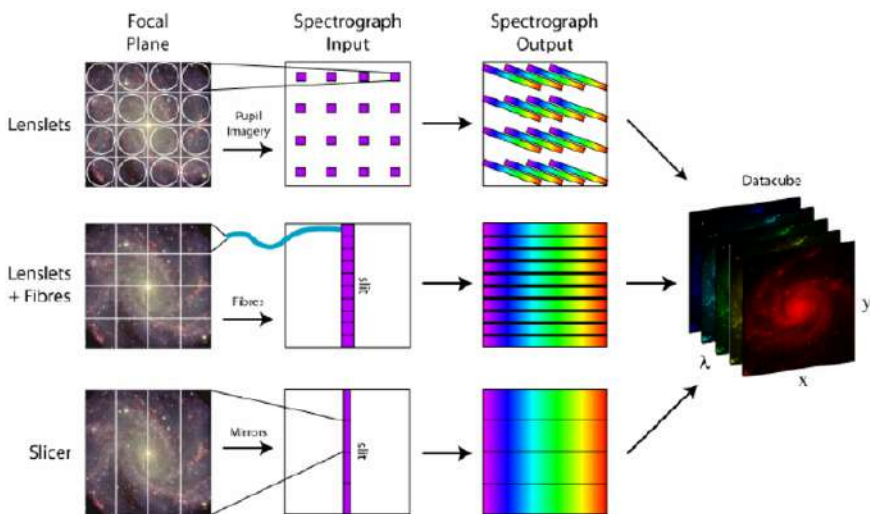


Figure 1.13: Methods of IFS to divide the FoV. The top one shows a lenslet array feeding the spectrograph. The second option is fibers which transfer the light to the spectrograph. At the bottom, image slicers use a mirror to segment the input image into thin sections. Credit: Westmoquette et al. (2009)

The Multi-Unit Spectroscopic Explorer (MUSE) is a panoramic IFS operating in the visible wavelength range on the Very Large Telescope (VLT). MUSE employs the slicer technique to form the final data cube. The instrument consists of 24 identical integral field units which split the FoV into 24 sections or channels, resulting in 24 separate optical beams. Each beam is then further split by a second slicer which divides the beam into 48 mini slits, which are directed to the spectrograph to obtain the spectra for a specific section of the FoV. This process occurs simultaneously across all 24 spectrographs. Finally, MUSE software reconstructs a 3D data cube by aligning the spectra according to their positions in the original FoV. A schematic view of the process is shown in Figure 1.14. In Wide-Field Mode (WFM), MUSE has a 1x1 square arcminute FoV sampled at $0.2 \times 0.2$ square arcseconds, a simultaneous spectral range of 465-930 nm, and a spectral resolving power ranging from 1750 at 465 nm to 3750 at 930 nm.

In this thesis, we use MUSE data which, in conjunction with HST photometry, offers a new and powerful way of measuring the velocity field of the stellar halos of nearby MW-like galaxies outside the Local Group, targeting individual stars. In particular, we will analyze the stellar halo of NGC 4945

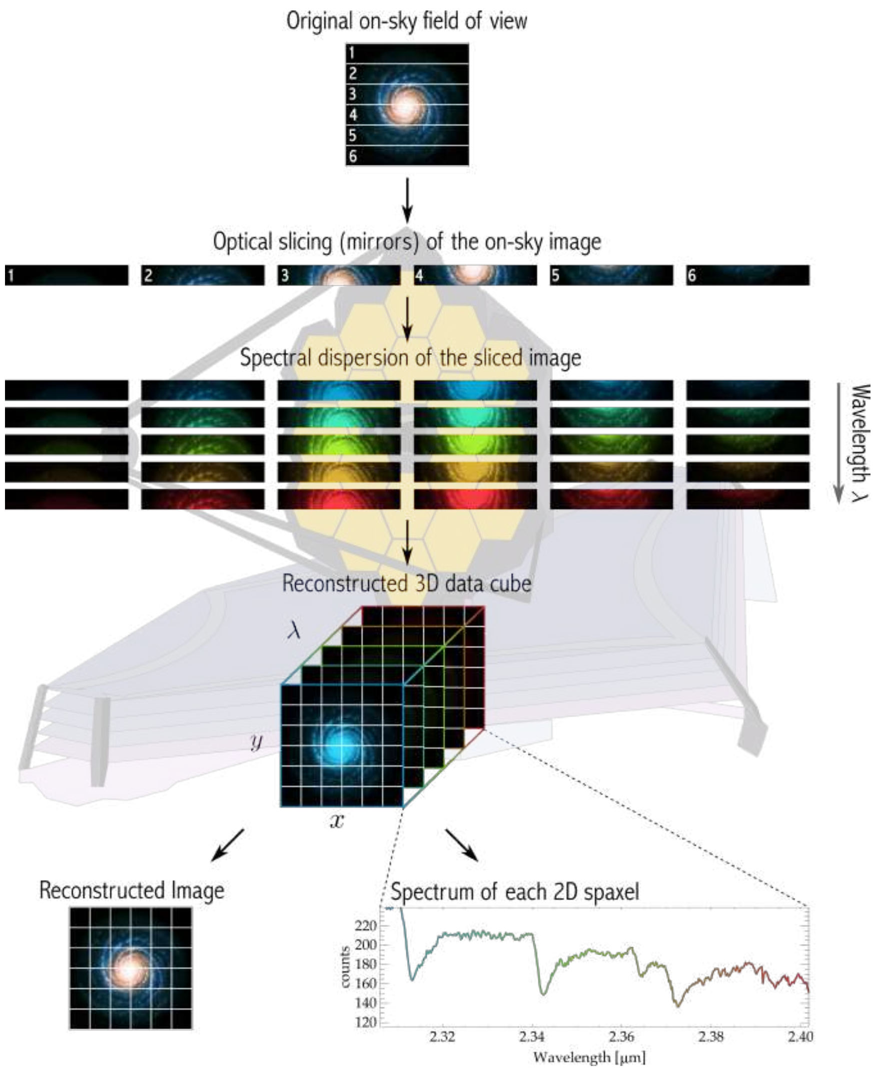


Figure 1.14: Illustrative view of a slicer-type IFS. An array of slicing mirrors samples the telescope focal plane, each of them directs its light to a dispersive element to produce a long slit spectrum of each slice on a detector. Pipeline processing then reconstructs the dispersed spectra together into a 3-dimensional data cube consisting of images of the source at each wavelength (or correspondingly, a spectrum of the source in each spaxel). Figure taken from this link.. This image example corresponds to the IFS on board of the James Webb Space Telescope which works in the same way as the one in MUSE.

## 1.5 NGC 4945 stellar halo: a typical MW-like stellar halo

As mentioned above, kinematic constraints on the stellar halos of MW-like galaxies outside the LG, and in particular of a typical stellar halo, can give us valuable insights into their formation mechanisms, as well as help us constrain the in situ component of the stellar halo for MW-like galaxies. We obtain such measurements in this thesis for the first time for a galaxy outside the LG.

NGC 4945 is a typical MW-like galaxy with a stellar mass of $3.8 \times 10^{10}$ $M_{\odot}$(Harmsen et al., 2017), luminosity of $M_B = -20.5$ (from HyperLEDA[1]; Makarov et al., 2014), and a systemic velocity of 563±3 km $s^{-1}$ from its HI spectrum (Koribalski et al., 2004). It is a spiral edge-on galaxy with an inclination $i > 80°$.

This galaxy is a unique case in that it is one of the closest (3.6 Mpc; Monachesi et al., 2016b) hosting both a Seyfert 2-type AGN (Schurch et al., 2002) and a central starburst (Bendo et al., 2016; Emig et al., 2020). In the radio regime, Emig et al. (2020) identified 27 compacts (1-4 pc) super star cluster candidates in the central starburst that likely correspond to young massive clusters powering the starburst. NGC 4945 is also notable for hosting a nuclear biconical outflow (Mingozzi et al., 2019), where the northwest (NW) cone is far brighter and extended than the southeast (SE) cone so the galactic plane resides behind the NW lobe with respect to the observer (i.e., tilted toward the observer) while the SE one stands behind the disk and is partially obscured by dust. Ianjamasimanana et al. (2022) studied the neutral gas using MeerKAT data, which are more sensitive than the previous HI work by Koribalski et al. (2018), showing that its HI disk is slightly larger than the bright optical disk. They also found a large amount of halo gas around the disk with an asymmetric distribution, with more HI located through the receding side of the galaxy. This halo gas does not follow the kinematics of the rotating disk and has velocities closer to the systemic velocity. The authors suggest that this gas is likely due to outflows driven by the central starburst of the galaxy (as seen in NGC 253, Lucero et al., 2015).

NGC 4945 has been observed as part of the GHOSTS survey (Figure 1.5) and it was found that it has a relatively large ($\sim 3.5 \times 10^9$ $M_{\odot}$, Harmsen et al., 2017) and metal-rich ([Fe/H]$\sim -0.9$ dex, Monachesi et al. 2016b) stellar halo, characterized using HST photometry of RGB stars as tracers for its underlying population. Its density profile along the minor and major axes are consistent with each other and can be approximated by power laws with slopes of $-2.72 \pm 0.17 \pm 0.2$ and $-2.73 \pm 0.23 \pm 0.2$ the first reported errors were calculated by bootstrapping and the second are the systematic uncertainties, respectively, as is shown in Figure 1.15 which result in an axis ratio of $c/a = 0.51$ (at 25 kpc), reflecting an oblate stellar halo (Harmsen et al., 2017). Additionally, Monachesi et al. (2016b) shows that NGC 4945 has a flat halo color radial profile, both on the major and minor axes, indicating a flat metallicity profile (see Figure 1.16). These characteristics leave us at a crossroads. On the one hand, we have a stellar halo that is large and oblate, suggesting a strong contribution from kicked-up disk stars, shaping its flattened distribution. On the other hand, the similarity in color profiles along the major and minor axis hints at an accretion origin. Thus, only a kinematical measurement has the potential to disentangle its origin. If we detect signs of rotation in the NGC 4945 halo, this could be attributed to either an in situ or accreted component. However, the absence of rotation would unequivocally indicate that its stellar halo is dominated by accretion.

NGC 4945 is thus an optimal galaxy for our investigation. Its proximity, at a distance of 3.6 Mpc (Monachesi et al., 2016b), makes it an exceptional laboratory for studying stellar halos. This nearby

[1] http://leda.univ-lyon1.fr/

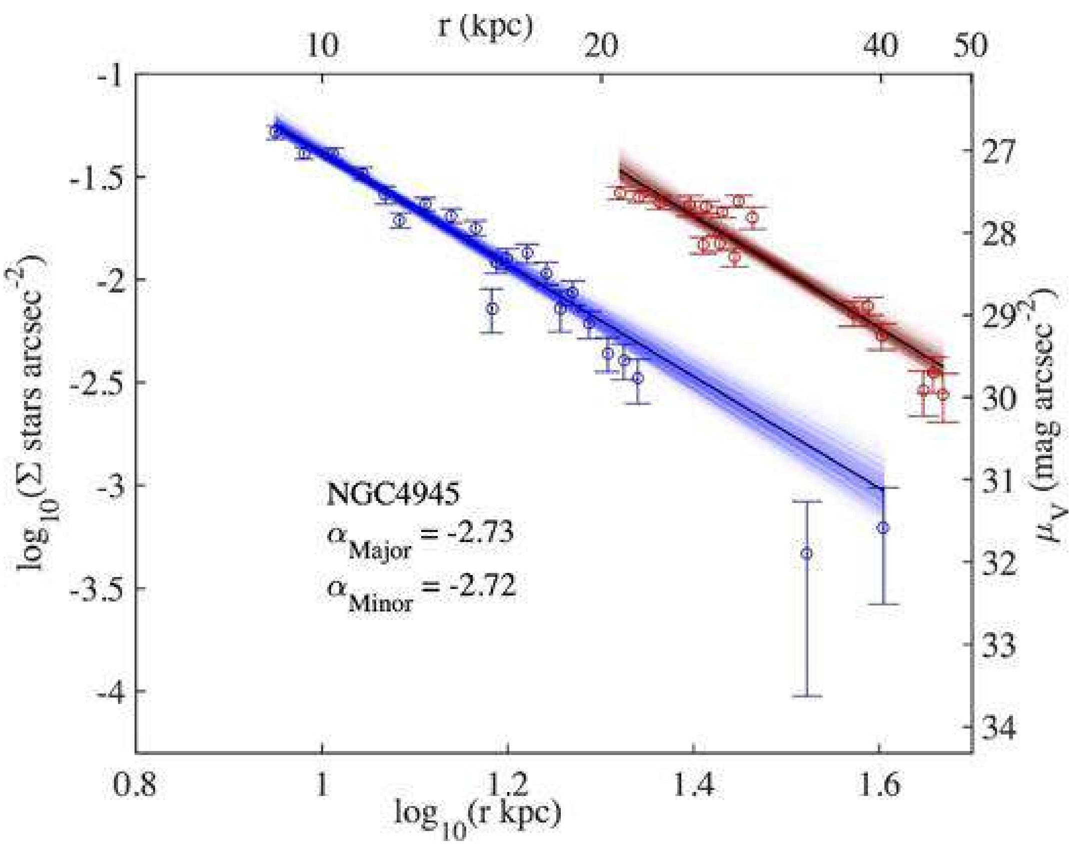


Figure 1.15: Stellar density profile for NGC 4945's halo (Harmsen et al., 2017) along the minor (blue) and major (red) axes. The profiles are fitted as a power law and the best fit is shown as the solid lines. The α values are the slope for the power-law. The translucent lines are the fits resulting from bootstrapping the data.

edge-on galaxy, similar to the MW, offers the unique advantage of resolving its stars with HST while also being accessible to observations with MUSE. As mentioned in the previous section, MUSE's IFS capabilities enable us to target individual stars and obtain their spectra. This allows us to perform the first kinematic study of a stellar halo with resolved stars in a galaxy beyond the LG, which is the focus of this thesis. Furthermore, the systemic velocity of NGC 4945 ($563 \pm 3$ km s$^{-1}$) provides a distinct separation between MW foreground stars and stars in NGC 4945. This separation, combined with the ability to resolve stars brighter than the TRGB, allows us not only to identify and quantify intermediate-age AGB stars but also to potentially uncover younger stellar populations within the stellar halo. These capabilities open a new window into understanding the complex assembly history and evolution of galaxies beyond our immediate cosmic neighborhood.

## 1.6 This Thesis

The primary motivation and main goal of this thesis is to perform the first-ever measurement of the velocity and velocity dispersion of a diffuse stellar halo in a galaxy outside the LG using resolved stars. This

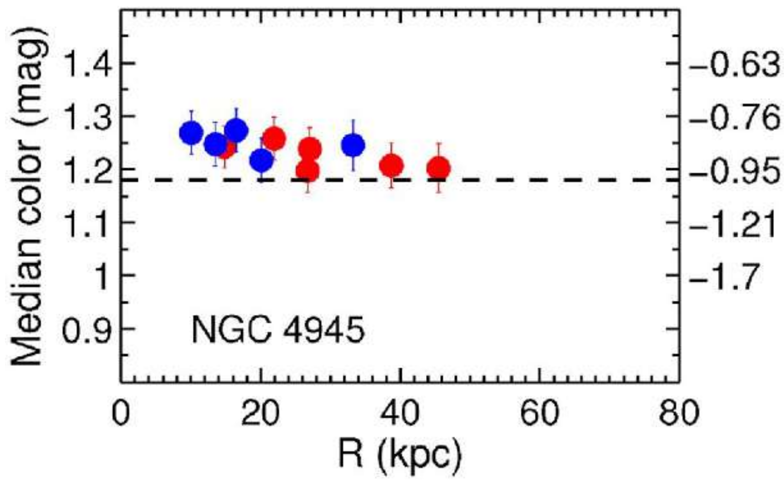


Figure 1.16: Color profile of NGC 4945's halo along the minor (blue dots) and major (red dots) axes as a function of projected radius. The dashed line at colour = 1.18 represents the average color profile of the 11 Bullock & Johnston (2005) stellar halo model realizations, which lacks a color gradient.The right-hand y-axis indicate the [Fe/H] values that the color correspond to. Figure extracted from Monachesi et al. (2016a).

work focuses on NGC 4945 to characterize the origin of its diffuse stellar halo by investigating whether its formation is predominantly due to accreted material or if it has a significant in situ contribution.

Studying the kinematics of stellar halos in MW-like galaxies outside the LG is a challenging endeavor. The difficulty arises primarily from the extremely low surface brightness of these structures, which makes observational data inherently scarce. To date, kinematic studies of stellar halos in external galaxies have largely relied on discrete tracers such as PN and GCs, or integrated light analyses. However, these approaches come with limitations. Discrete tracers often sample only sparse and specific stellar populations, while integrated light studies are vulnerable to contamination from scattered light and can not isolate individual stellar populations.

Consequently, most detailed kinematic analyses of stellar halos of spiral galaxies have been confined to the MW and M31. Expanding this field of study to include a third MW-like galaxy with resolved stellar populations represents a significant leap forward. It opens a new window for understanding the formation and evolution of stellar halos in MW-like galaxies beyond the LG. Such studies offer unprecedented opportunities to disentangle the complex interplay of accretion and in situ processes that shape these halos.

The potential of this methodology is further amplified when considering the capabilities of next-generation telescopes. Instruments like MOSAIC and HARMONI will allow not only for more extensive kinematic studies of stellar halos but also for metallicity analyses of individual stars in galaxies even farther away. These advancements will significantly enhance our ability to build a statistically meaningful sample of MW-like galaxies, paving the way for a deeper understanding of stellar halo origins and their evolution across cosmic time.

In this thesis, we target two fields along the major axis of NGC 4945: (1) a halo field at a projected distance of ∼35 kpc and (2) an outer disk field at 12.2 kpc, which serves as a control velocity field. For both fields, the mean velocity and velocity dispersion are measured by co-adding the spectra of individual RGB stars in the halo field and RGB/AGB stars in the outer disk.

This work represents the first kinematical study of a diffuse stellar halo derived from the spectra of its resolved stars in a galaxy beyond the LG. The methodology focuses on extracting spectra of RGB and AGB stars in each observed field using MUSE. In both fields, individual stellar spectra are stacked to produce a combined spectrum with an increased S/N, allowing us to obtain reliable measurements of the LOS radial velocity and velocity dispersion. The selection of RGB and AGB stars was accomplished using the precise photometry and astrometry provided by HST observations.

In addition, this thesis demonstrates that, for stars brighter than the TRGB in the halo field, the S/N of their spectra is sufficient to measure their radial velocities. This capability allows us to distinguish NGC 4945 halo stars from MW foreground stars, a critical step given the low Galactic latitude of NGC 4945 and the resulting high foreground contamination.

Moreover, this thesis explores MW-like galaxies in the TNG50 and Auriga simulations to provide a cosmological context for the observed kinematics of NGC 4945's stellar halo. Using these simulations, we focus specifically on regions of the stellar halo and outer disk situated at comparable distances to the observed fields in NGC 4945. This approach ensures a consistent comparison between simulated and observed data.

Our analysis reveals that galaxies with stellar halo kinematic properties similar to those of NGC 4945 are relatively uncommon within the full sample of simulated MW-like galaxies. In addition, when we further restrict the sample to galaxies with stellar halo masses consistent with measurements by Harmsen et al. (2017), the number of analogs decreases even further, isolating a subset of six true analogs to NGC 4945. For these analog galaxies, we conducted an analysis to partially reconstruct their accretion histories. This included identifying and characterizing the satellites that contributed to their stellar halos at z=0, examining the masses of these satellites, and the epochs of their accretion.

The main results obtained in this thesis, the methodology developed to achieve them, and the steps taken to compare observations of NGC 4945 with simulations are described step by step throughout the following chapters. This sets the stage for the thesis outline, which is detailed below.

### 1.6.1 Outline

The structure of this thesis is as follows:

- Chapter 2: This chapter introduces the HST photometric catalogs obtained from the GHOSTS survey and the selected fields in NGC 4945 used for this study. These catalogs resolve the RGB down to 2 magnitudes below the TRGB, allowing precise star selection for kinematic analysis. We also present the MUSE observations conducted to perform the first kinematic study of a stellar halo beyond the Local Group. These observations target two fields previously analyzed by GHOSTS: Field 1, representing the outer disk, and Field 5, focusing on the stellar halo of NGC 4945. These new spectroscopic data complement the GHOSTS photometry, enabling measurements of the heliocentric line-of-sight radial velocities for stars in both the stellar halo and the outer disk.

- Chapter 3: This chapter provides a step-by-step explanation of the methods developed to extract individual stellar spectra from the halo and outer disk fields. We detail the processes used to combine these spectra, achieving the final signal-to-noise ratio required for reliable velocity measurements.

- Chapter 4: We present the main results obtained from measuring the velocity and velocity dispersion in the halo and outer disk fields. Additionally, we highlight the velocities of three individual stars in the halo field that are brighter than the TRGB and are strong candidates for membership in NGC 4945. This chapter concludes with a discussion of our findings in the context of existing kinematic studies of the stellar halos in the MW and M31.
- Chapter 5: We compare our results with Auriga and TNG50 Simulations. We measure the velocity and velocity dispersion of simulated MW-like galaxies at distances analogous to the MUSE observed fields in NGC 4945. Furthermore, we partially reconstruct the accretion histories of these simulated galaxies, identifying the contributing satellites, examining their masses, and determining the epochs of accretion.
- Chapter 6: We summarize the key methodological steps and the primary results obtained throughout this thesis.
- Chapter 7: We conclude this thesis by presenting potential follow-up studies that arise from this work, emphasizing their relevance for advancing the field of stellar halo kinematics in galaxies beyond the LG.

# Chapter 2

# Data

In this chapter we describe the data used in this thesis to achieve our goal of measuring the line-of-sight velocity of the stellar halo of NGC 4945. We use new MUSE spectroscopic observations in combination with photometric catalogs from the GHOSTS HST survey.

We first introduce the GHOSTS survey and its photometric catalogs, providing precise positions and magnitudes of the stars detected in the regions observed. Additionally, we give an overview of the main features of integral field spectrographs, with focus on MUSE, and detail the MUSE data cubes that will be analyzed in this thesis. We also describe the stellar library employed for fitting and measuring the radial line-of-sight velocities in the observed fields.

## 2.1 Photometric catalog from GHOSTS

The GHOSTS survey[1] is one of the largest HST programs designed to study resolved stellar populations in the outskirts of 18 nearby disk galaxies of different masses, luminosities, and inclinations (Radburn-Smith et al., 2011; Monachesi et al., 2016b, for a detailed description). This survey aims to characterize the stellar halos of these galaxies while minimizing contamination from the disk and avoiding uncertainties caused by projection effects. For this purpose, the selected galaxies fulfill strict criteria: they are edge-on ($i > 87^\circ$) with rotational velocity above 80 km s$^{-1}$. Additionally, these galaxies needed to have low extinction with $A_V < 0.5$ mag and a distance modulus less than 31.13 ($\sim$ 16.8 Mpc).

Each galaxy in the survey has several spaced HST pointings observed with the Advanced Camera for Surveys (ACS) and the Wide Field Camera 3 (WFC3). The ACS observations were conducted using its wide field channel, which has a field of view of $202 \times 202$ squared arcseconds, while the WFC3 observations employed the ultraviolet and visible light channel, offering a slightly smaller field of view of $160 \times 160$ squared arcseconds. These pointings, distributed along the major and minor axis of the galaxies, enable the study of stellar halo out to large projected galactocentric distances of up to $\sim$75 kpc. The precise field locations were strategically chosen to avoid bright foreground stars, allow full HST roll angles available, and sample key features such as disk truncation and previously identified stellar streams.

The primary tracers of the stellar halo population are RGB stars, as they are both the most luminous and numerous among old stellar populations that are expected to dominate the GHOSTS halo fields.

[1] http://vo.aip.de/ghosts/index.html

Imaging was thus obtained in the F814W filter, where the flux of these stars peaks, together with the F606W filter for color discrimination. Compared to the longer wavelength baselines available with other filter choices, F606W and F814W imaging maximizes throughput in a single orbit at the expense of some loss in color sensitivity. Each field was observed with at least two exposures per filter to remove the effects of cosmic rays, with total exposure times ranging from 500 s to 1300 s for the nearest and farthest galaxies, respectively. This setup ensured the required S/N of 10 at 1 mag below the TRGB.

Data reduction and stellar photometry were performed using the GHOSTS pipeline, described in detail in Radburn-Smith et al. (2011) and Monachesi et al. (2016b). In short, the images were downloaded from the Mikulski Archive for Space Telescopes (MAST), underwent bias subtraction, flat-fielding, cosmic ray subtraction, and correction for charge transfer efficiency (CTE). Images for each field and filter were aligned and combined using the ASTRODRIZZLE package, which also flagged residual cosmic rays and removed distortions. The output drizzled images were used as a reference frame for coordinate positions. Stellar photometry was then performed with DOLPHOT, which performed simultaneous Point Spread Function (PSF) fitting photometry on all images per field. DOLPHOT provides the position of each star relative to the F814W drizzled image, together with the instrumental HST magnitudes in the VEGAmag system. The DOLPHOT output catalogs include various diagnostic parameters such as sharpness and crowding used to distinguish stars from background galaxies or other contaminants. To minimize spurious detections and maximize the number of real stars, specific parameter thresholds, referred to as culls in the ACS[2] catalogs, were applied. These criteria are as follows:

$$-0.06 < \mathrm{SHARPNESS}_{F606W} + \mathrm{SHARPNESS}_{F814W} < 1.30$$

$$\mathrm{CROWDING}_{F606W} + \mathrm{CROWDING}_{F814W} < 0.16$$

Applying these selection criteria to the photometry output effectively removed ~95 percent of contaminants.

Unresolved background galaxies are the most important source of contamination, especially in the outermost fields (stellar halo) which may contain only a hundred real stars. Additionally, SEXTRACTOR was used to mask all extended sources in each field, including background galaxies and bright foreground MW stars, which were subsequently removed from the photometric catalogs. These catalogs enabled the construction of CMDs for each field, typically reaching $\sim 2-3$ magnitudes below the TRGB.

As explained in Chapter 1, this thesis focused on the study of the stellar halo of NGC 4945, one of the GHOSTS galaxies. For this galaxy, 12 HST fields were observed – six along the major axis and six along the minor axis (as shown in Figure 1.5). These fields extend up to 45 kpc along the major axis and 40 along the minor axis. Among these fields, this work focuses on two specific fields along the major axis: Field 1 at $\sim$ 12 kpc (located in the outer disk) and Field 5 at $\sim$ 35 kpc (in the stellar halo). The two GHOSTS fields, 1 (outer disk) and 5 (halo) have a surface brightness of ~26 and ~29 mag/arcsec$^2$ and a total number of stars of 16088 and 1638, respectively. (Harmsen et al., 2017). The choice of the major axis was motivated by the fact that models predict that the contribution of kicked-up disk stars, i.e. the in situ halo, is more noticeable along the major axis (Monachesi et al., 2016a; Gómez et al., 2017). These two fields provide key insights into both the disk and halo components of the galaxy.

[2]The corresponding values for WFC3 data differ slightly but remain close to those used for the ACS culls; detailed values can be found in Monachesi et al. (2016b).

Table 2.1: Positions (RA and Dec) of both MUSE FoV, the total integration time of the final datacubes, average seeing during observations and the field's distance to the galaxy's center.

| Field | RA (h:m:s) | Dec (d:m:s) | $t_{\rm exp}$ (s) | seeing (arcsec) | D (kpc) |
|---|---|---|---|---|---|
| Halo | 13:07:41.64 | -49:02:54.74 | 29920 | 0.7 | 34.6 |
| Outer disk | 13:06:17.66 | -49:19:40.25 | 2520 | 0.7 | 12.2 |

Field 1 was chosen to maximize the contribution from the disk and it will be used as a control field to study the kinematics of the disk, as it is expected to exhibit disk-like velocities. In contrast, Field 5 was chosen to reach as far out as possible into the stellar halo while also having enough RGB stars.

## 2.2 MUSE Observations

While the GHOSTS survey provides high-precision photometric data, spectroscopic observations are required to measure radial velocities and velocity dispersions for studying the kinematics of the stellar halo, as well as (ideally) metal abundances and [$\alpha$/Fe] ratios. In this thesis, we complement the GHOSTS photometric data with spectroscopic data from MUSE observations. The much smaller field of view of MUSE compared to ACS necessitates a careful selection of pointing locations to maximize the overlap with RGB stars in the GHOSTS fields. Additionally, bright foreground MW stars were avoided during the selection process.

The MUSE field for the outer disk is positioned in one corner of Field 1, closest to the galaxy center, ensuring the largest contribution from disk stars. In contrast, the halo MUSE field is within Field 5, at 35 kpc, to probe the outer halo while retaining a sufficient number of RGB stars for stacking and achieving the required S/N (see Chapter 3). These two fields are shown in the left panel of Figure 2.1, where the GHOSTS fields are marked in yellow, and the MUSE pointings are shown in red.

Observations of the two MUSE fields were taken in July 2019 and in January, February, and March 2020 in service mode during dark time and photometric conditions with an average seeing of $0.8''$ (observing program 103.B-0514, PI: A. Monachesi). The instrument was set up in wide-field mode, without adaptive optics. We use the instrument in its nominal-wavelength mode (480-930 nm). This setup ensures a FoV of $1' \times 1'$, a spatial sampling of $0.2''$ per pixel, with a spectral sampling of 1.25 Å/pixel. Each resolution element is sampled by 2.5 pixels along the spectral direction, which corresponds to a velocity resolution of 50-80 km s$^{-1}$. The spectral resolution of MUSE at 9300 Å is 3590. The choice of the wide-field mode allows us to cover a larger area and thus include as many stars as possible.

The integration time was chosen such that it would be possible to reach the required minimum S/N$>2$ per resolution element in the final stack to measure reliable velocities (Toloba et al., 2016a). We expect to have 2000 and 150 RGB stars for co-addition in the respective MUSE FoVs. Taking into consideration these numbers, the halo field was observed for 8 h in 11 Observing Blocks (OB) of 2720 s each. Each OB consists of 2 exposures of $\sim 1320$ s and a rotation of $90^\circ$. The outer disk field was observed for 42 min in 1 OB of 4 exposures of 630 s. Table 2.1 lists the positions of both fields, the integration times, the average seeing conditions (in arcsec) during the observations, and distances from the NGC 4945 galactic

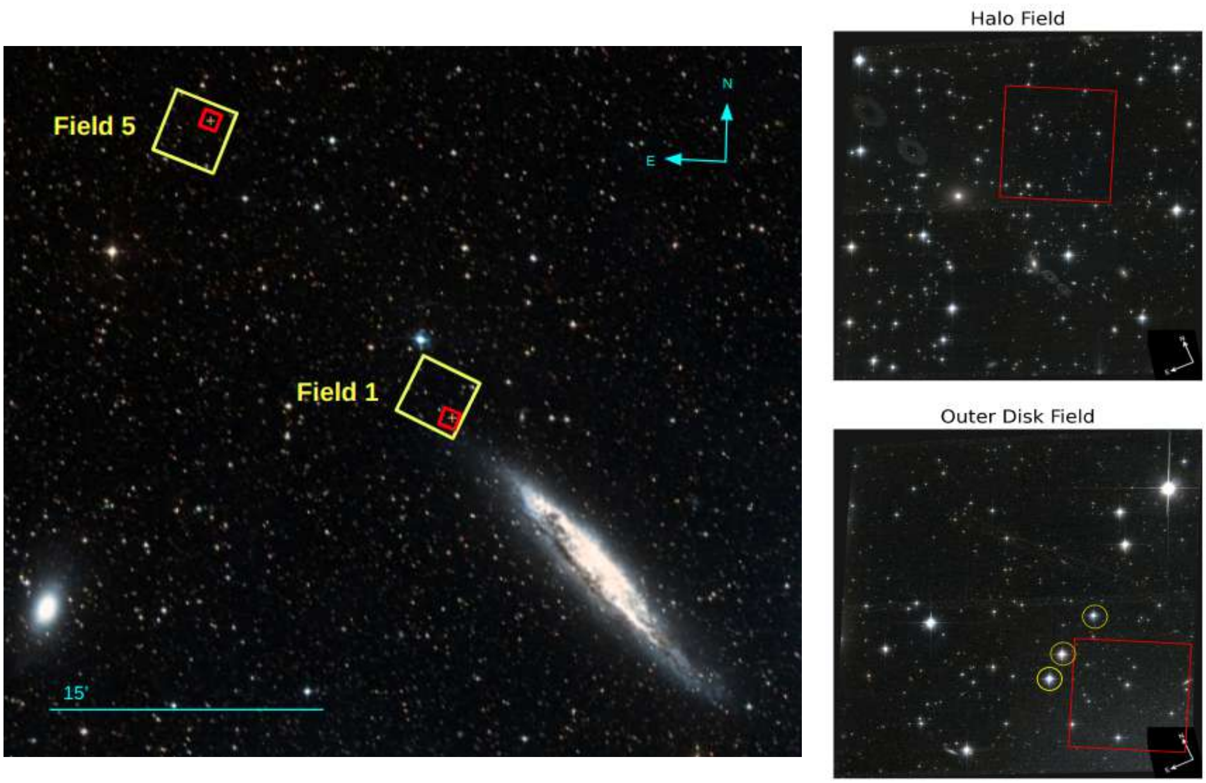


Figure 2.1: DSS colored image of NGC 4945 showing the location of the GHOSTS Field 1 and 5 (yellow boxes) and the MUSE targets (red boxes) shown on the left. Field 5 is at ∼35 kpc, and Field 1 is at ∼12 kpc from the center of the galaxy along the major axis. HST ACS/WFC images of Field 1 (bottom panel) and 5 (top panel) shown on the right. The FoV of each image on the right is 3.4'× 3.4'. Red boxes show both MUSE FoVs (1'×1') inside the HST ACS/WFC Fields 1 and 5, and yellow circles highlight the 3 bright MW stars that are outside the outer disk MUSE FoV but close to one edge of the MUSE FoV.

center.

All the data have been reduced by the MUSE consortium using the official pipeline version 2.8 (Weilbacher et al., 2020). All the exposures were processed by the MUSE scibasic recipe, which used the corresponding daily calibrations (flatfields, bias, arc lamps, twilight exposures) to produce a pixel table containing all pixel information: location, wavelength, photon count, and an estimate of the variance. The pipeline recipe scipost is then used to perform astrometric and flux calibrations, and the sky subtraction on the pixtable to create the final reduced data cubes. We use the two final integrated data cubes, one per field, containing a flux- and wavelength-calibrated spectrum in each spaxel as a starting point[3], to which we then make an astrometric correction and additional residual sky emission lines subtraction, as we show in Chapter 3, before the spectral analysis.

In Figure 2.2, we show the images of the MUSE datacubes extracted within the HST F814W passband, i.e. using the flux in the wavelength range from 6869 to 9300Å, for the outer disk and halo MUSE fields with all detected stars from GHOSTS marked in red.

### 2.2.1 Color-magnitude diagrams of stars in the MUSE fields

In Fig. 2.3 we show the GHOSTS CMDs of stars in the regions observed by MUSE: the halo (left) and outer disk (right) containing a total of 184 and 2975 stars respectively. The magnitude of the TRGB for NGC 4945 was calculated by Monachesi et al. (2016b) to be 23.72 in the F814W filter. These CMDs reach two magnitudes below the TRGB, well above 50% completeness level (see Monachesi et al. 2016b), and they clearly evidence the presence of a well-defined RGB population (both in the halo and outer disk field) and AGB stars (in the outer disk field). The RGB stars are the main source for characterizing the halo field, while AGB stars are additionally incorporated to characterize the outer disk field. Also in Fig. 2.3, we illustrate the delimited region for selecting RGB stars (red box) and AGB stars (blue box), with F814W magnitudes between 23 and 23.72 and a color range between 0.8 and 2.5. Figure 2.2 displays, as red points, the distribution of the selected RGB stars within the red box for the halo MUSE field and the distribution of the selected RGB and AGB stars (blue and red box) for the outer disk MUSE field. The boxes that we use for analysis in this work have been predominantly defined using the CMD of the outer disk field. We adopted a conservative red limit to the AGB box to avoid as much as possible contamination from MW stars (see below). The astrometric precision of the GHOSTS data aids in the extraction of the spectra of individual RGB and AGB stars in each field.

In addition to the dominant population of RGB stars in the halo of NGC 4945, owing to its low Galactic latitude $b = 13.3°$, the CMDs should also contain MW foreground stars as contaminants. We estimated the contamination level of foreground stars using TRILEGAL models[4] (Girardi et al., 2005). TRILEGAL is a population synthesis code for simulating the stellar photometry of any Galaxy field. The photometry can be produced for many different broad- and intermediate-band systems. We use the coordinates of our halo and outer disk field and the area to be covered around our fields (the area covered by a MUSE field). We also choose the photometric systems HST/ACS WFC. We use this model to simulate the photometric properties of stars located toward our MUSE fields and to estimate the MW foreground contamination. For the magnitude range F814W= 21-27 and color (F606W- F814W)>0 the MW trilegal stars are shown in Figure 2.3 as green crosses. We find that most of the MW contaminants are stars brighter than the

[3]The data are publicly available http://archive.eso.org/cms.html

[4]http://stev.oapd.inaf.it/cgi-bin/trilegal

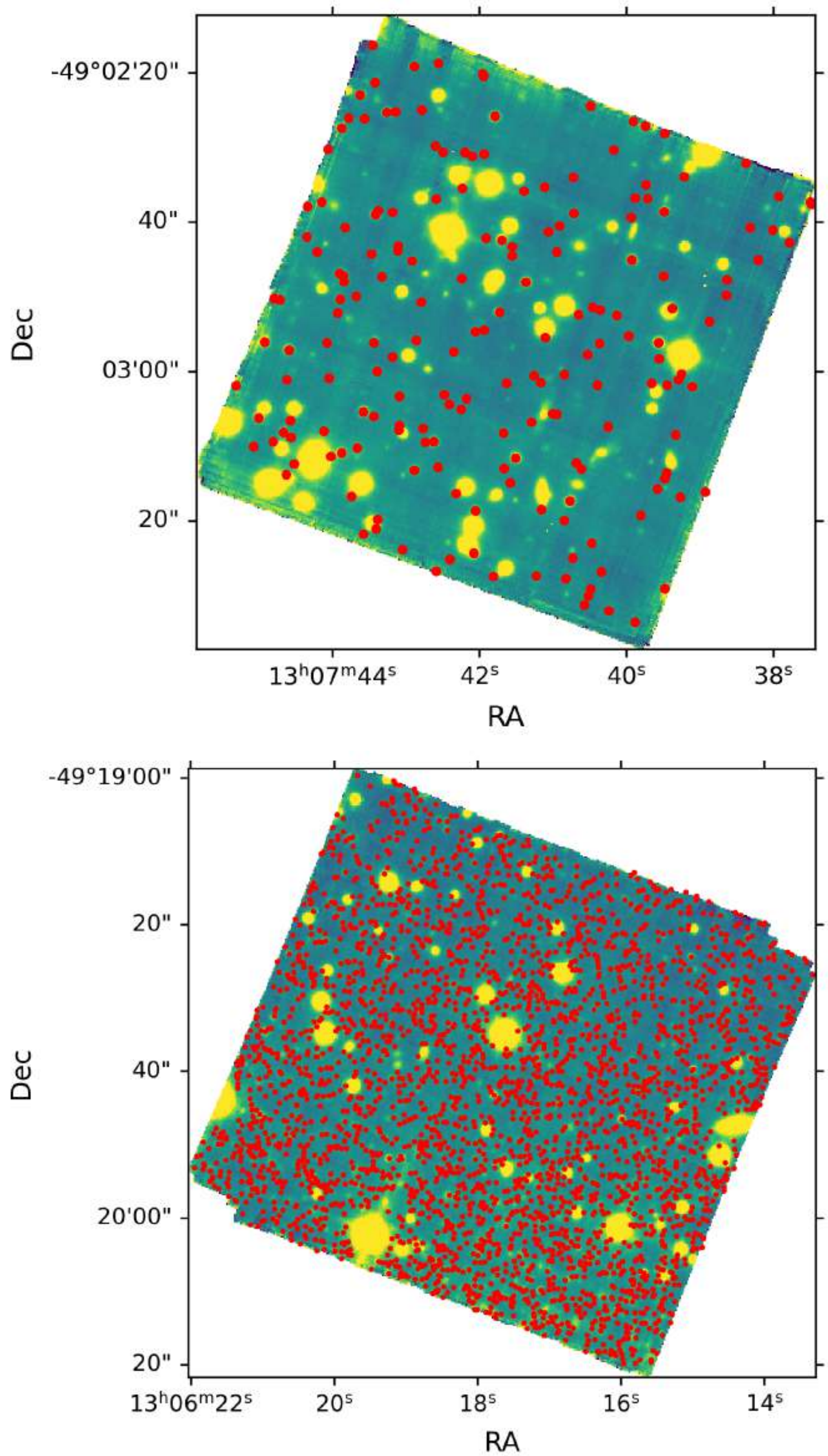


Figure 2.2: Halo (upper) and outer disk (bottom) MUSE FoV. The images were created using the flux in the wavelength range from 6869 to 9300 Å, representative of the F814W HST/ACS filter. Red points are all the detected stars from GHOSTS catalogs.

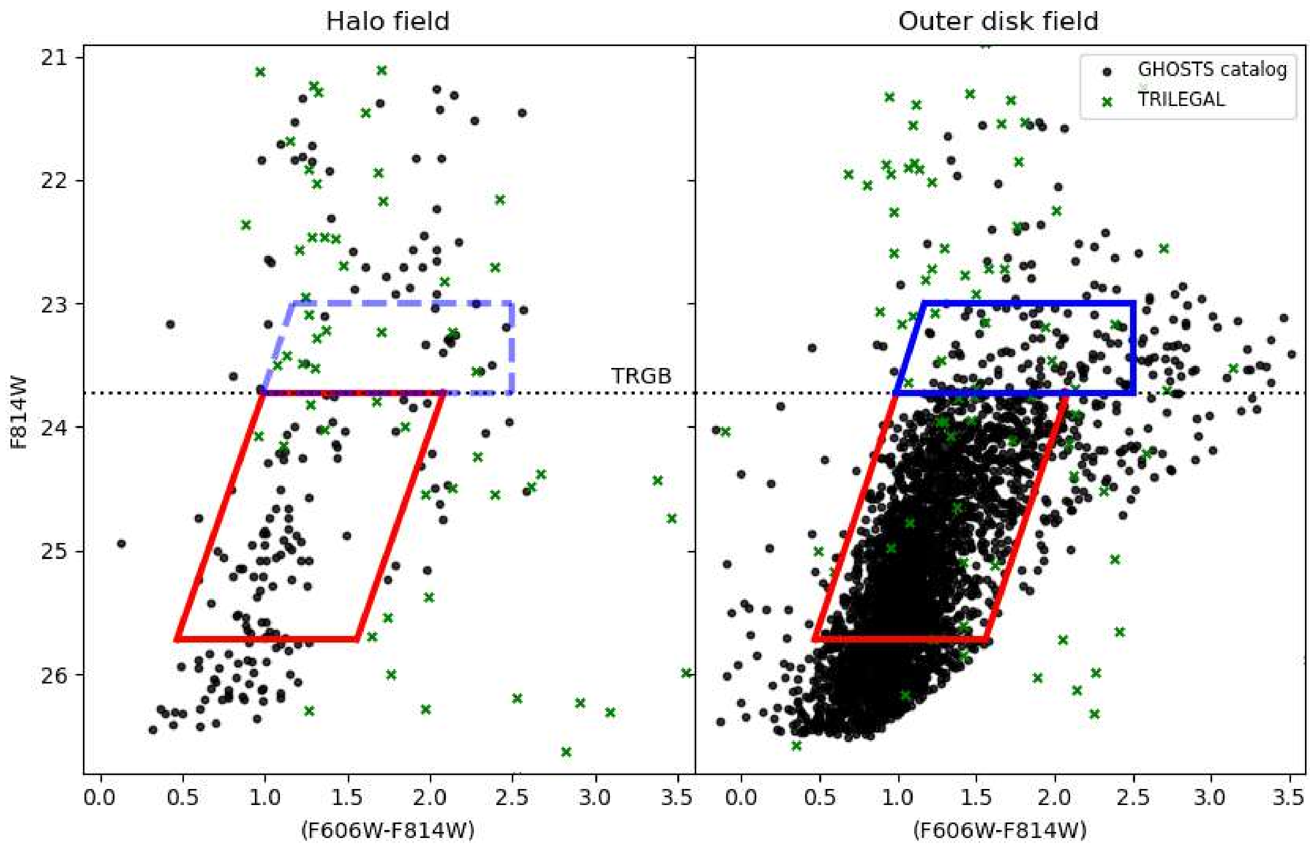


Figure 2.3: CMDs of detected stars from GHOSTS in the MUSE Halo (left) and Outer Disk (right) FoV. Magnitudes are corrected for Galactic extinction. The magnitude of the TRGB is 23.72 in the F814W filter and it is marked with a black dotted line. Green crosses represent the contamination from MW foreground stars estimated using the TRILEGAL model. The red and blue boxes are illustrative and indicate the regions in the CMD where RGB and AGB stars are selected, both in the halo and outer disk fields. We marked the AGB box differently in the halo field (light blue dashed lines) from the one in the outer disk field to indicate where AGB stars would mainly be located in this field. However, these AGB stars are not added to the final stack spectrum; only the RGB stars are included. In the case of the outer disk, since the contamination from MW background stars is negligible compared to the number of NGC 4945 stars, both RGB and AGB stars were used in the final stack.

TRGB or redder than the RGB ($F606W - F814W > 1.6$) and have a higher fractional contribution in the low-density halo field. If a few of the stars above the TRGB are truly NGC 4945 stars in the halo field, it is important to find them since those would be the brightest stars in our sample, thus, they will contribute significantly to the combined spectrum in that field. Thanks to the large integration time in the MUSE halo field, individual spectra for stars brighter than the TRGB (i.e. with $F814W < 23.72$) have enough S/N to measure their velocities, which permits discrimination between NGC 4945 ($400 < v_{los} < 800$ km $s^{-1}$) and MW ($v_{los} < 400$ km $s^{-1}$) stars. In the outer disk field, it is not possible to obtain reliable velocity measurements of individual NGC 4945 stars due to the shorter exposure time. Nevertheless, given the higher stellar density (see Fig. 2.2), the number of MW contaminants is negligible compared to the AGB and RGB stars in that field, thus, there is no need to kinematically discriminate the MW contaminants from the stacked spectrum of the outer disk field.

# Chapter 3

# Methodology

In this chapter, we explain the methodology developed to conduct the kinematic analysis of the stellar halo of NGC 4945. We detail all the different steps and tests carried out to obtain spectra of RGB and AGB stars that are as free of contamination as possible, whether from background galaxies or foreground MW stars. We additionally describe the stacking process and the procedure for measuring the LOS velocities and velocity dispersions.

Since our target stars are fainter than 23 in I-band magnitude, their individual S/N range between 0.5-4 and 0.1-1 for the halo and the disk RGB, respectively. For this reason, we were unable to utilize the standard stellar spectra extraction software PampelMUSE (Kamann et al., 2013). PampelMUSE was developed to extract stellar spectra in crowded fields optimizing for the PSF as well as the fluxes of deblended stars and works very well in the high S/N regime (S/N >10). On the other hand, in the low S/N regime, it becomes very difficult to optimize for the flux of a star. Instead, in the limit of working at very low S/N, we develop our own custom spectral extraction method akin to "forced PSF photometry", which allows us greater flexibility. Instead of optimizing for the Point Spread Function (PSF), we constrain it from the very bright stars present in both our MUSE FoVs. Given a PSF, we then extract the spectra of our target stars at their proper locations, forcing the target to have the PSF.

For the kinematical measurements, our approach is based on the one developed by Toloba et al. (2016a) but has key differences. We use higher-resolution HST imaging (0.05" per pixel), allowing us to target fainter individual stars and to perform a more precise astrometry. Additionally, MUSE's IFU capability lets us observe all stars in its field of view and use surrounding pixels as local background. The position of Toloba's slits is mainly within the stream of NGC 4449, which has higher stellar density and surface brightness ($\mu_g = 26.72\,\mathrm{mag/arcsec^2}$, Martínez-Delgado et al., 2012) compared to the surface brightness of the stellar halo at $\sim$ 35 kpc from the center of NGC 4945 ($\mu_V \sim 29\,\mathrm{mag/arcsec^2}$, Harmsen et al., 2017), where one of our MUSE fields is located. While MUSE has a lower spectral resolution (R$\sim$3000) than Toloba et al.'s data, its broader spectral coverage allows it to fit a wider wavelength range and cover more spectral features. Therefore, MUSE in combination with HST imaging, offers a new and powerful way of measuring the velocity field of the stellar halos of nearby MW-like galaxies outside the Local Group.

In the following sections, we describe our astrometric corrections to the MUSE datacubes, the sky[1]

[1]When referring to the sky in this work, we specifically mean the residual sky component, as the sky background was already subtracted during the data reduction process carried out by the MUSE pipeline.

subtraction procedure, how we constrain the PSF, our stellar extraction procedure, and finally, the stacking process and procedure to measure the radial line-of-sight (LOS) velocities, velocity dispersions, and their associated uncertainties.

## 3.1 Astrometry correction

To accurately extract the stellar spectra of our target stars, it is essential to achieve precise astrometric alignment between the MUSE fields and the HST images, as the stellar positions are provided using the WCS obtained from HST. Therefore, we aligned the WCS of our MUSE fields with that of the GHOSTS HST images. This step is critical because the MUSE pipeline's default astrometric alignment often exhibits a shift relative to the calibration provided by HST.

To perform the astrometric correction for each datacube, we employed the MPDAF[2] tool. We first aligned the images, calculated the offset between the sky coordinate systems of the current image and the reference image, and adjusted the pixel offsets in the coordinate reference pixel values (CRPIX) of the WCS in the MUSE field images to align them with those in the HST image.

For the disk field, the calculated offset was -4.30 and 6.54 pixels, corresponding to a shift of dy = 0.86 arcsec and dx = 1.31 arcsec. For the halo field, the offset was -6.77 and -3.10 pixels, corresponding to a shift of dy = 1.35 arcsec and dx = -0.62 arcsec.

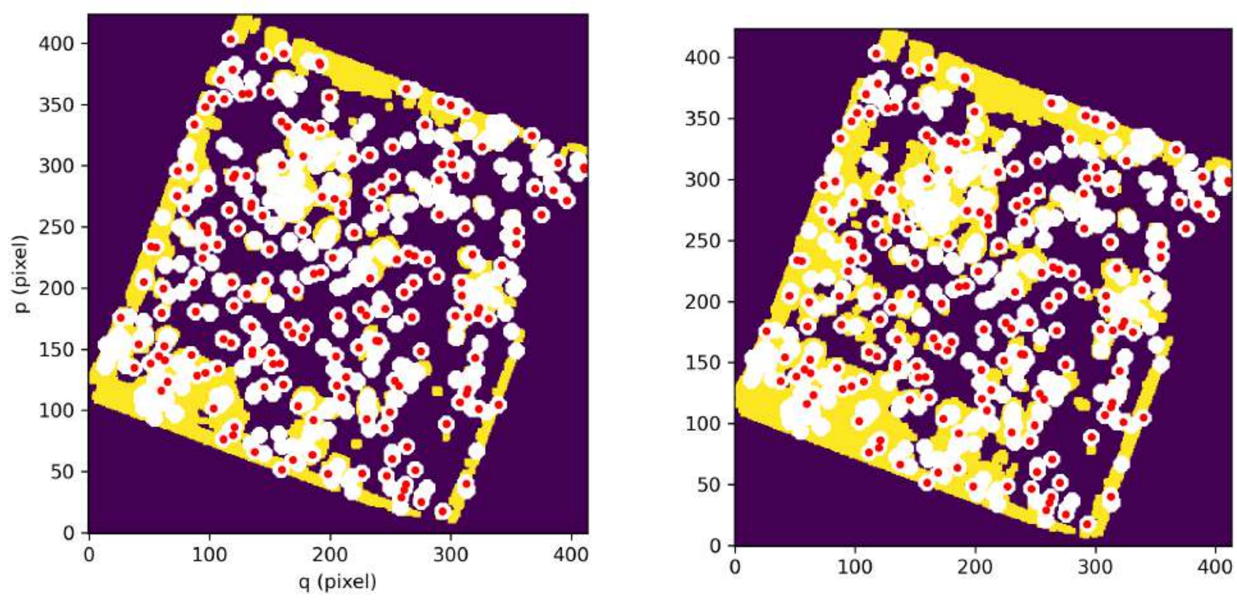


Figure 3.1: Comparing the masks created with photutils using two different sigma thresholds, $\sigma = 1.0$ (left) and $\sigma = 0.5$ (right), represented by the yellow area. In white we overplotted all the sources detected by GHOSTS masked with a radius of 7 pixels. Finally, red dots are the stellar sources from the GHOSTS catalog. The remaining purple spaxels inside the FoV are the unmasked spaxels used to calculate the sky background spectrum. The purple regions at the edges are outside the FoV, so they were not used.

[2] https://mpdaf.readthedocs.io/en/latest/index.html

Table 3.1: Masking configurations used to generate residual sky spectrum in the halo field with ZAP. The first column indicates the sigma threshold applied to detect sources, and the second column specifies the additional radii used to mask sources from the GHOSTS catalog. Columns 3 and 4 show the total number of unmasked and masked pixels, respectively. Finally, column 5 provides the percentage of unmasked pixels relative to the total FoV.

| $\sigma$ | r (pix) | N° unmask | N° mask | % unmask |
|---|---|---|---|---|
| 1 | 7 | 42894 | 64028 | 40.1 |
| 0.5 | 7 | 34434 | 72488 | 32.2 |
| 0.5 | 10 | 20661 | 86261 | 19.3 |

## 3.2 Residual Sky subtraction

Once the positions of the MUSE data cube are aligned with the HST reference image, the next critical step is to refine the sky subtraction. As mentioned in Section 1.3, the surface brightness of the stellar halo is far below the brightness of the sky. Therefore, this step is crucial to extract stellar spectra as free from sky contamination as possible, given the faintness of the signal from individual stars.

Upon inspecting the spectra of the halo field cube, we noticed that the standard sky subtraction procedure carried out by the MUSE pipeline leaves behind residual skylines within the final data cube. The sky subtraction in the MUSE pipeline has multiple ways of deriving the sky contribution, which also depends on the user input and the type of field being processed. For example, in the case of a filled science field, an offset sky field has to be used to characterize the sky background; sky lines and continuum are then needed as inputs. The procedure is the same for a largely empty science field. The spectrum has to be created from a region of science that is devoid of objects, and a list of the sky emission lines is required. This is our case since we do not have an offset sky field. In this case, the user usually has to tell the pipeline which spatial fraction of an exposure is sky-dominated so that the software can use that portion of the data to reconstruct the sky spectrum. In our case, the SKYMETHOD parameter was set to MODEL, and the `skymodel_fraction` was 0.2, which defines the fraction of the field to take as a sky. The `skymodel_ignore`, set to 0.05, is the default 5 percent of the FoV with the darkest pixels considered as artifacts to be ignored. The next fainter pixels (defined in the `skymodel_fraction`) are taken to calculate the sky background.

To address this problem (default sky subtraction), we utilized the Zurich Atmosphere Purge (ZAP; Soto et al., 2016), a post-processing tool designed to enhance sky subtraction by effectively removing residual sky lines while preserving the flux and shape of astronomical source lines. The ZAP code uses a principal component analysis (PCA) to the data cube to identify and subtract residual sky features. To ensure accurate processing, all detectable sources within the field of view (FoV) were masked, leaving only sky pixels in the cube. From these source-free regions, ZAP calculates the residual sky background directly and subtracts it, improving the quality of the astronomical signals in the data cube.

To ensure the best results, we varied the source detection threshold three times and compared the outcomes. We use the *photutils* tools to create three different masks: one with a sigma threshold of 1 and two with a threshold of 0.5. Additionally, we manually masked all the sources from the GHOSTS catalog down to F814W$\sim$26.5 that were not detected by *photutils*. This approach ensured that only sky

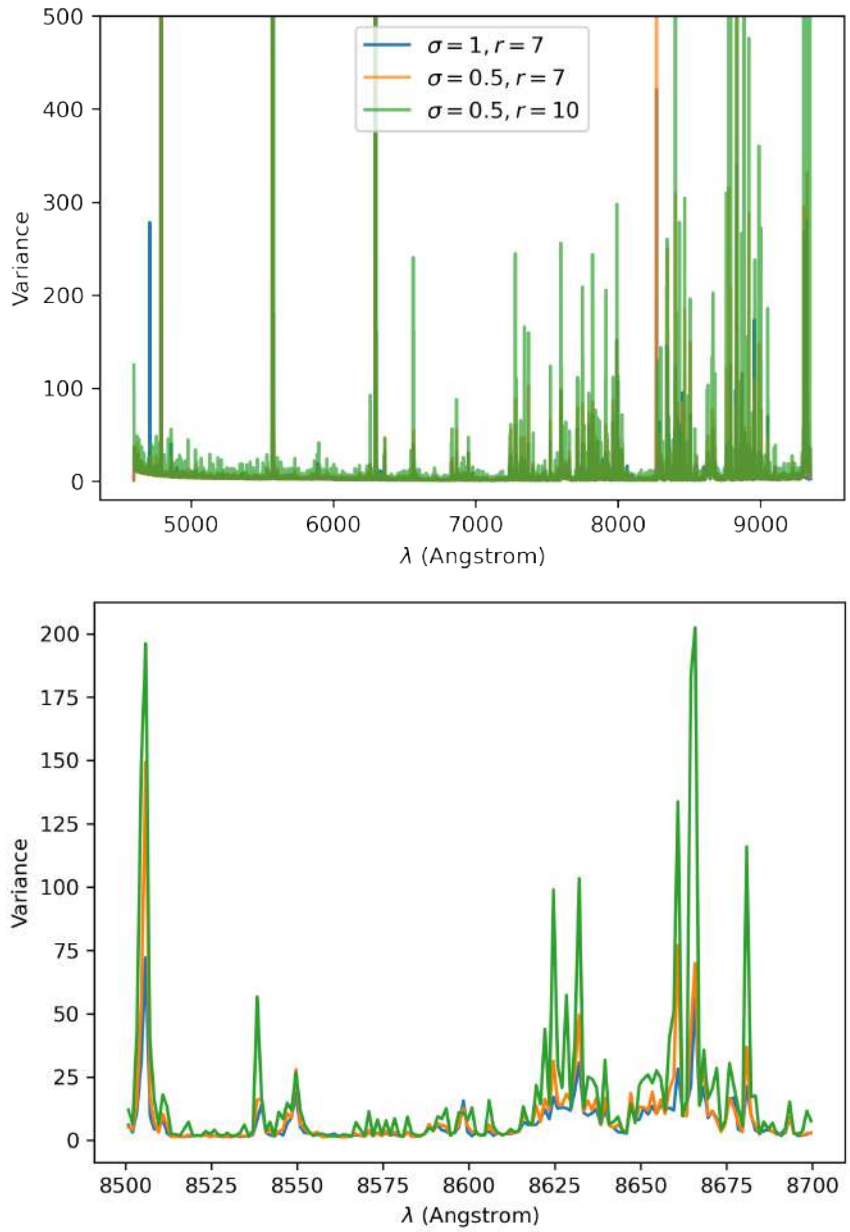


Figure 3.2: Comparing the variance spectrum calculated with the sky spaxels available using the three different masks. We show the spectra in the entire wavelength range in the upper panel. In the bottom panel, we zoom in the CaT region of the spectra. The green spectrum represents the variance using the more restrictive mask (σ=0.5 and r=10), i.e, using the minimum number of sky spaxels to estimate the sky background, the blue is the variance calculated with the largest number of sky spaxels, as shown in Table 3.1. We selected this one, which shows a better subtraction of the residual sky lines.

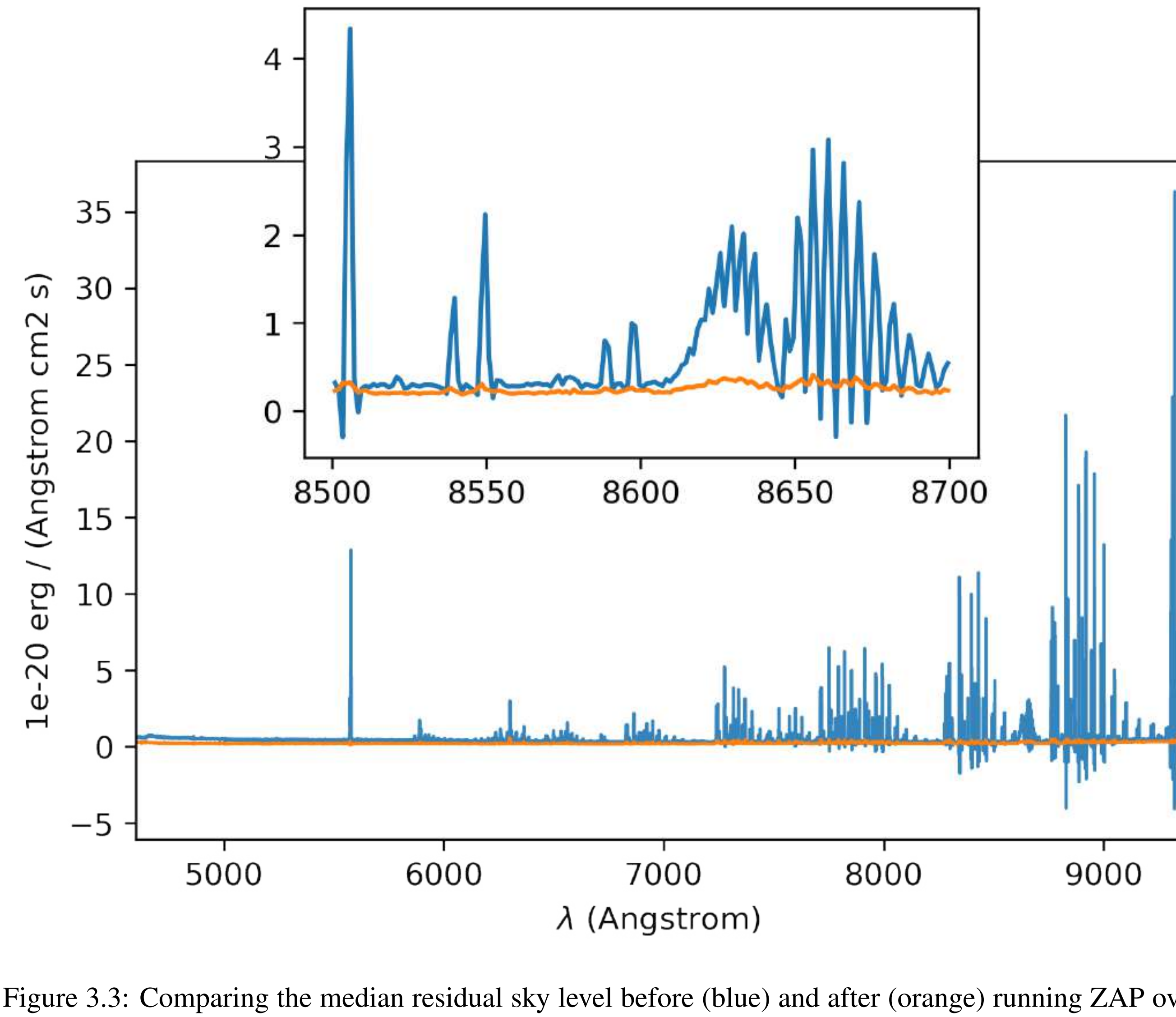


Figure 3.3: Comparing the median residual sky level before (blue) and after (orange) running ZAP over the halo datacube. The inner box is a zoom-in in the CaT region.

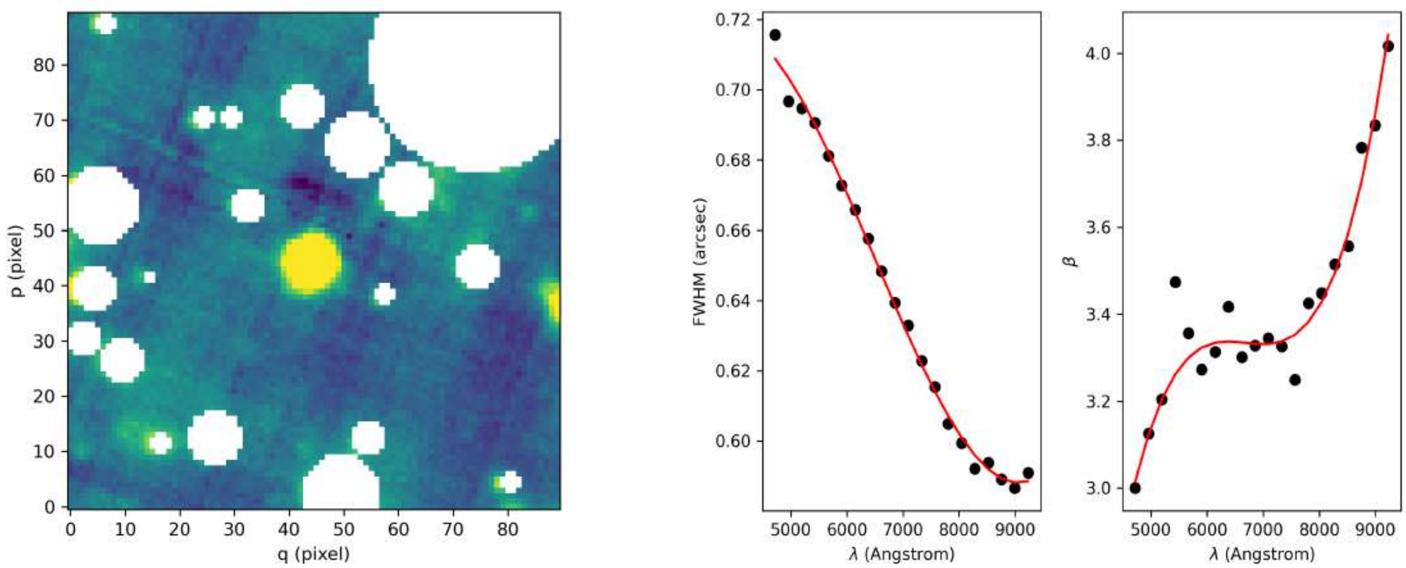


Figure 3.4: Left: Isolated star at the center of a data cube of 90x90 pixels. This star was used to fit the PSF. White circles are nearby sources that were masked. Right: FWHM and β parameters as a function of wavelength.

pixels remained unmasked for ZAP processing.

For the $\sigma = 0.5$ masks, GHOSTS catalog sources were masked with radii of 7 and 10 pixels. For $\sigma = 1$, a radius of 7 pixels was used. These radii were chosen to cover the sources as comprehensively as possible while preserving enough unmasked pixels to calculate the residual sky spectrum (see Figure 3.1).

Table 3.1 shows the number of source-free pixels available for each mask configuration and their percentage relative to the total pixels in the halo FoV. ZAP was applied using the source-free pixels from each mask, and the variance spectrum of the resulting clean cube was calculated from the same unmasked pixels. This procedure was repeated for all three masks, and the variance spectra were compared, as shown in Figure 3.2. In this Figure, we can see that the variance spectrum for the most restrictive mask is higher, implying that this mask did not significantly improve the removal of residual sky lines. Based on the variance spectra comparison, we concluded that the optimal results were achieved with the $\sigma = 1$ mask and a radius of 7 pixels. Figure 3.3 shows the sky spectra before and after ZAP.

For the outer disk, higher stellar crowding made it impractical to use the same mask sizes as in the halo field, as this would leave too few unmasked spaxels for effective sky cleaning. Instead, a mask with a sigma threshold of 1 was created, masking GHOSTS catalog sources with a radius of 1 pixel. ZAP was then executed using the same procedure as for the halo field.

## 3.3 Point Spread Function

An accurate description of the PSF is essential for the optimal extraction of stellar spectra from a datacube, especially when dealing with faint stars. To derive the PSF, we use the MUSE specific tools in MPDAF, creating a wavelength-dependent PSF model under the assumption that the PSF is spatially constant across the entire FoV. This model employs a Moffat circular function to describe the radial

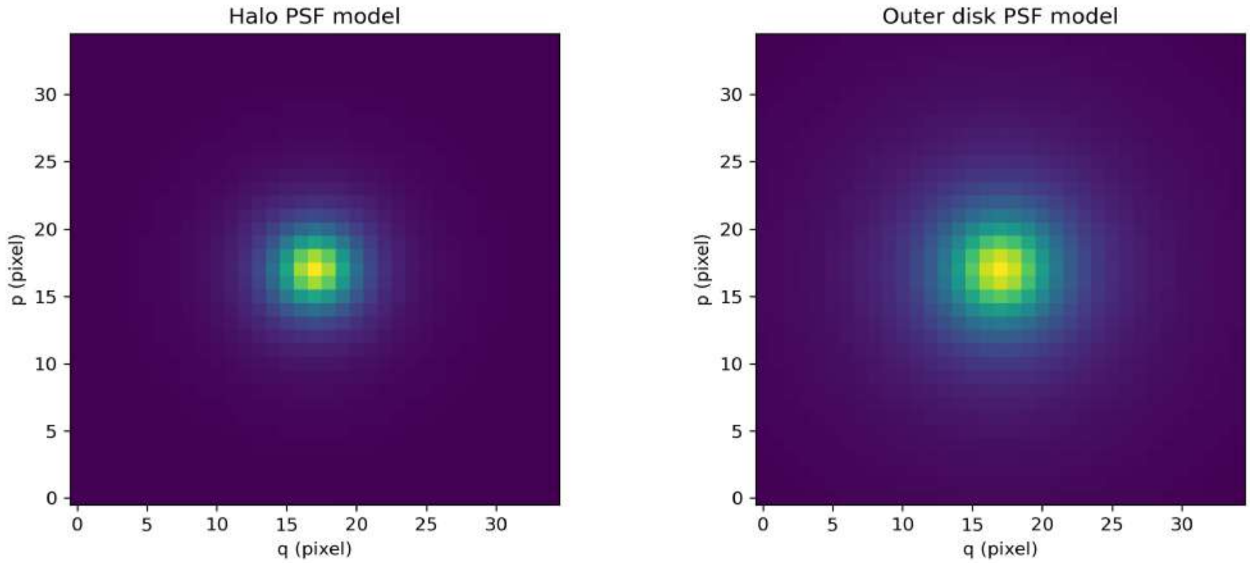


Figure 3.5: Mean image of the PSF model for the halo (left) and outer disk (right) fields.

shape of the PSF, where the full-width at half-maximum (FWHM) and β parameters vary as a function of wavelength.

The Moffat profile is described as:

$$PSF(r) = I_0 \left[ 1 + \left( \frac{r}{r_d} \right)^2 \right]^{-\beta}, \tag{3.3.1}$$

where $I_0$ is the central intensity, and $r_d = FWHM / \left( 2\sqrt{2^{1/\beta} - 1} \right)$. The β parameter measures the strengths of the PSF's wings.

This process was performed independently for the halo and outer disk fields to account for differences in observing conditions and potential variations in the PSF. For each field, we selected an isolated, bright MW star with a 90x90 spaxels sub-cube centered on the star. We then masked all nearby sources within this sub-cube to ensure the PSF fitting was not affected by contamination.

The PSF fitting was carried out on 20 evenly spaced layers along the wavelength axis, allowing the FWHM and β parameters to be adjusted as functions of wavelength. Figure 3.4 illustrates the process for the halo field, showing the sub-cube with masked sources and the resulting FWHM and β trends with wavelength.

The resulting PSF cubes for the halo and outer disk fields encompass the entire wavelength range and are shown in Figure 3.5. These PSF models are used to extract the spectra of target stars and create a model of bright stars in each FoV. This model allows us to estimate the contamination levels from bright stars on fainter target stars, as described in Section 3.4.

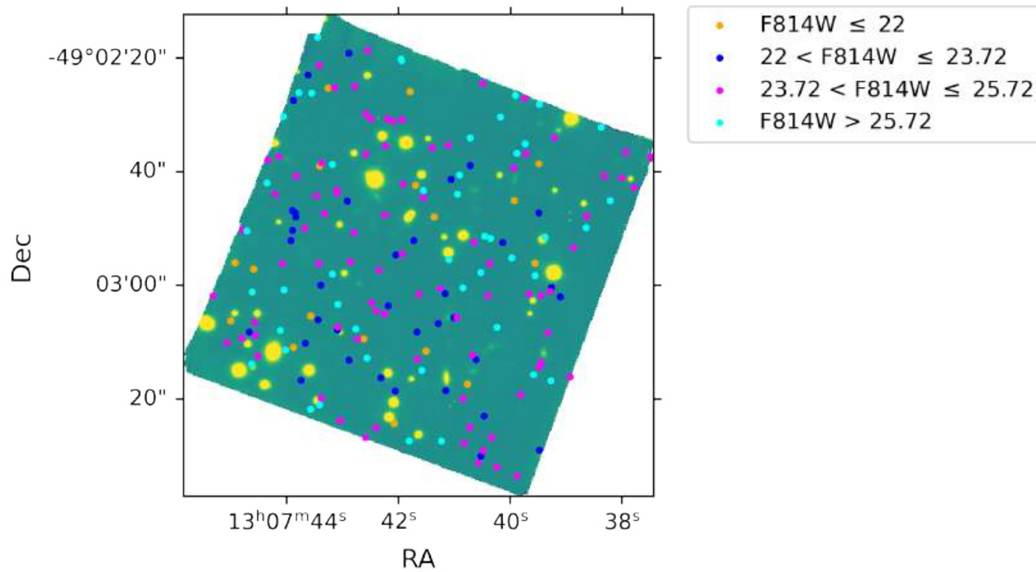


Figure 3.6: Image of the halo field with GHOSTS stars marked accordingly to its magnitude.

## 3.4 Contamination from bright and neighboring sources

As mentioned earlier, it is essential to account for contamination from various sources, particularly when analyzing RGB stars in the halo and both RGB and AGB stars in the outer disk field. The main sources of contamination include: (1) bright MW foreground stars (from Gaia and not present in the GHOSTS catalog), (2) bright MW stars with magnitudes above the TRGB (found in the GHOSTS catalogs), (3) faint MW stars with magnitudes below the TRGB, and (4) background galaxies. Minimizing contamination in the individual stellar spectra is key for accurate analysis.

The most significant contamination comes from scattered light originating from bright MW stars, particularly those brighter than the TRGB. This contamination can impact the FoV and hinder the extraction of clean spectra from fainter stars. In Figure 3.6, we show an image of the halo FoV where all the stars from the GHOSTS catalog are marked in different colors, corresponding to specific magnitude ranges. The stars within the magnitude range representing the RGB stars analyzed in this study (F814W between 23.72 and 25.72) are shown in magenta. Additionally, the brightest sources, MW foreground stars, and background galaxies not included in the GHOSTS catalog appear in yellow. This figure highlights that some stars in the RGB range are located close to bright foreground MW foreground stars or other stars brighter than 23.72, further emphasizing the need to account for these contaminants.

To better visualize the influence of bright stars on the fainter ones, we selected a narrow rectangular region in the halo FoV that includes a bright MW star and two GHOSTS catalog stars: one with a magnitude of 21.3 and another faint star with a magnitude of 26.2. The top panel of Figure 3.7 shows an image of this region. The two brighter stars are clearly visible, while the faintest star is barely distinguishable. The bottom panel of Figure 3.7 displays the flux distribution across the region. All three stars are identifiable by the peaks in the flux distribution. Additionally, the proximity of the fainter stars to the bright MW star indicates that the flux from the bright star likely affects them.

Additionally, fainter stars comparable in brightness to our target RGB stars, which are redder than the RGB box defined in Fig. 2.3 (and hence likely MW star), may also contaminate the extracted flux of our sample of RGB stars. Lastly, extended galaxies that are near in projection to our RGB stars may also introduce contamination to their stellar spectra.

To assess which stars in our RGB and AGB selected boxes (see Figure 2.3) from the GHOSTS catalog are affected by these potential sources of contamination, we create a 2D model of the contaminants in both fields. In each of the MUSE FoVs, there are several bright stars (as shown in Figure 2.2) that are not present in the cleaned GHOSTS catalog since they are saturated or fragmented into small entities by the GHOSTS pipeline. Some of these stars have been identified by Gaia Survey (Gaia Collaboration et al., 2021), totaling 18 and 15 in the Halo and Outer disk, respectively. We utilize *photutils* to identify stars and galaxies within each MUSE image field. In the halo field, we identify a total of 125 bright stars, 7 foreground galaxies, and 19 faint stars outside the RGB box. In the outer disk, we identify 52 bright stars and one foreground galaxy.

Subsequently, we construct a mock halo/outer disk image of the FoV, respectively, by positioning a scaled and wavelength-flattened PSF for each individual contaminating star identified. Furthermore, we modeled the projected galaxies with a two-dimensional Sersic function whose parameters (Sersic index, effective radius, position angle, and central coordinates) we extracted from the image using *galfit* (Peng et al., 2002). The distribution of light from these models is added into the mock field at the position of each of the extended galaxies detected. In Fiugre 3.8 we show the mock halo/outer disk image of the FoV, respectively.

With all these potential sources of contamination accounted for in the mock field, we estimate the projected flux of scattered light from these sources at the position of each star from the GHOSTS catalog within the RGB and AGB boxes selected for our analysis. We then compare this estimated flux with the actual flux of these stars at their central spaxel and calculate the percentage of contamination that reaches each star. Given that we are working with very faint stars, we conducted several tests to evaluate different levels of contamination (5 to 30%) to minimize the inclusion of light from neighboring sources in our stacked spectrum of RGB/AGB stars. We find that the velocity measurements are stable in all cases. Thus, to maximize the number of stars in each field, and thus the S/N in the stacked spectrum, and at the same time minimize the contamination as much as possible, we will include in our analysis stars with contamination levels up to 20% for the halo field and up to 30% for the outer disk field. This corresponds to 53 and 1021 RGB stars in the halo and outer disk field, respectively, when considering stars down to two magnitudes below the TRGB.

## 3.5 Star Spectrum Extraction procedure and background subtraction

In this Section, we explain our approach for extracting the spectra of RGB and AGB stars in both the halo and outer disk fields, emphasizing the maximization of S/N while minimizing contamination from the background sky. Because of the differences in depth and crowding between the two fields (see Figure. 2.2), different procedures were employed in the halo and outer disk field for estimating the sky background and for the extraction of the star spectrum.

The extraction was guided by the following steps: In the halo field, we compute the local sky background around each star by selecting a square region whose size depends on the star's magnitude. For

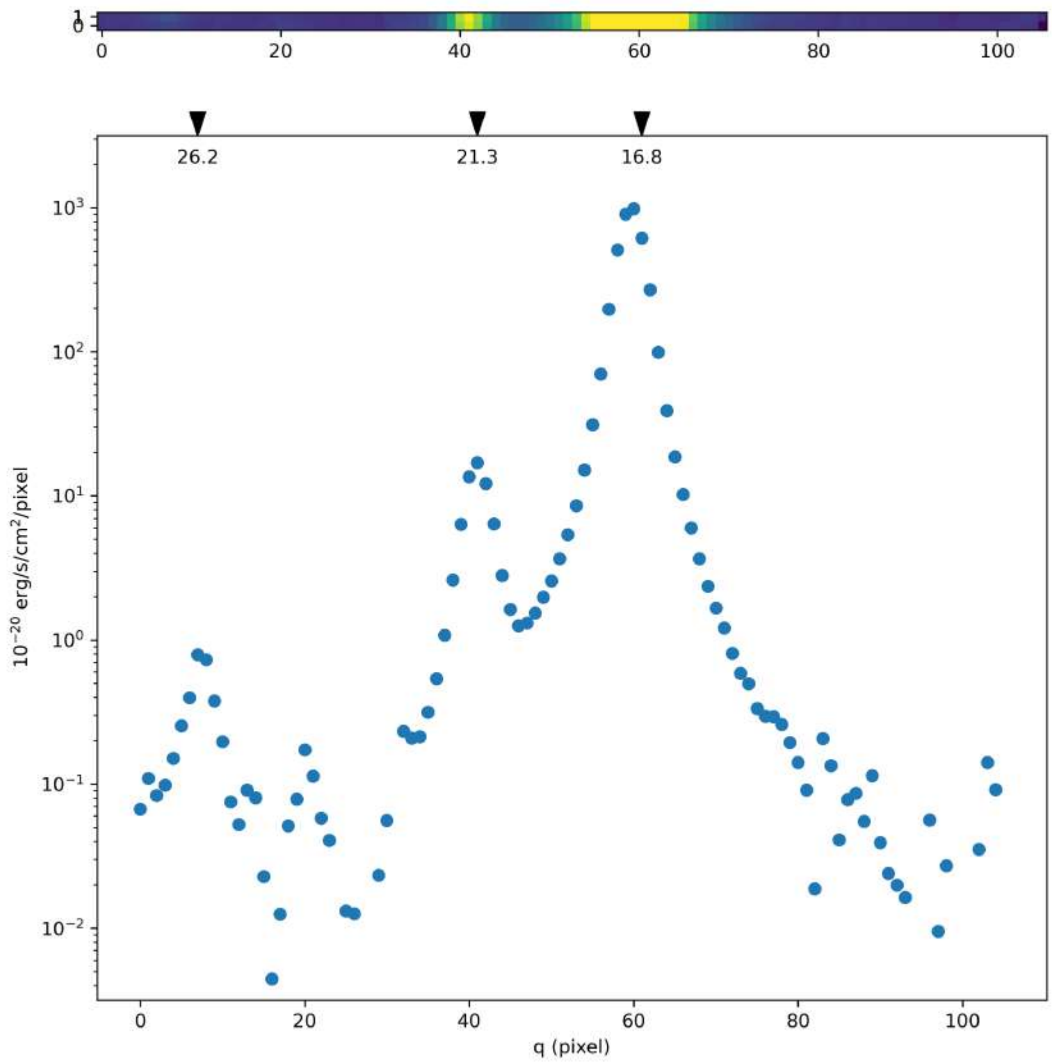


Figure 3.7: Flux distribution across a narrow region containing three stars with different magnitudes. The top panel shows an image of the region where the stars are located. Arrows indicate the positions of the flux peaks corresponding to each star in the distribution below. The F814W magnitudes of the stars are 16.8, 21.3, and 26.2, as is indicated below the arrows.

Table 3.2: Magnitude and color of 4 stars of different magnitudes used to estimate the extraction radius ($r_{ext}$) by magnitude range and the background radius ($r_b$).

| ID | F814W | F606W - F814W | $r_{ext}$ | $r_b$ |
|---|---|---|---|---|
| 35 | 21.52 | 1.18 | 3 | 9-14 |
| 412 | 23.27 | 2.11 | 2 | 6-10 |
| 777 | 24.50 | 1.09 | 1 | 4-6 |
| 846 | 24.52 | 2.58 | 1 | 4-6 |

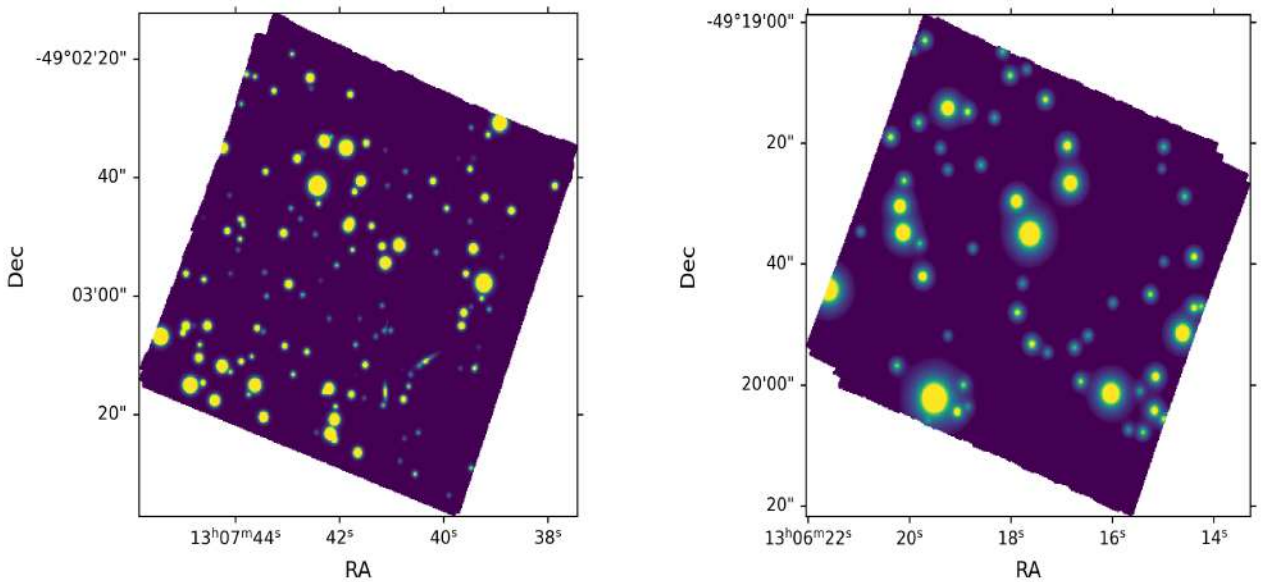


Figure 3.8: Halo and outer disk mock image FoV. These were used to calculate the scattered light from bright sources to our target RGB/AGB stars.

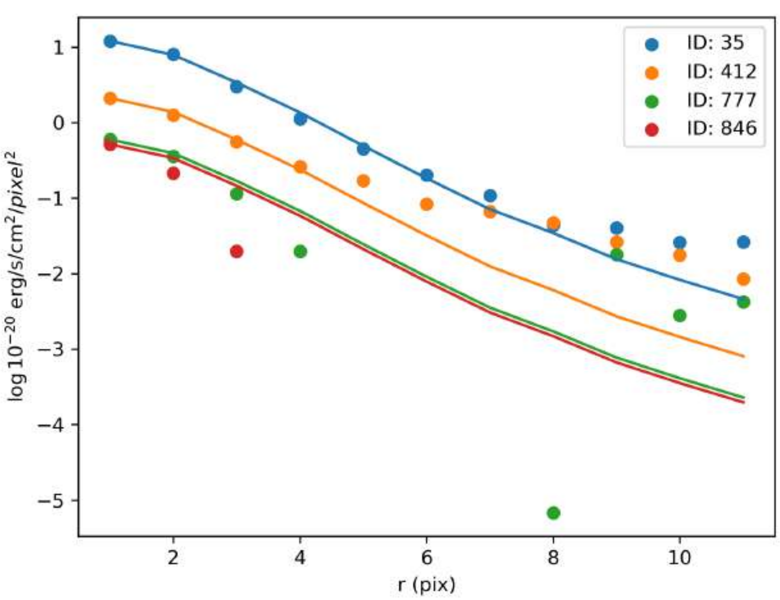


Figure 3.9: Radial profile of four stars with different magnitudes. Points are the flux measured at the respective distances, while the lines correspond to the PSF model fitted to the central flux of each star.

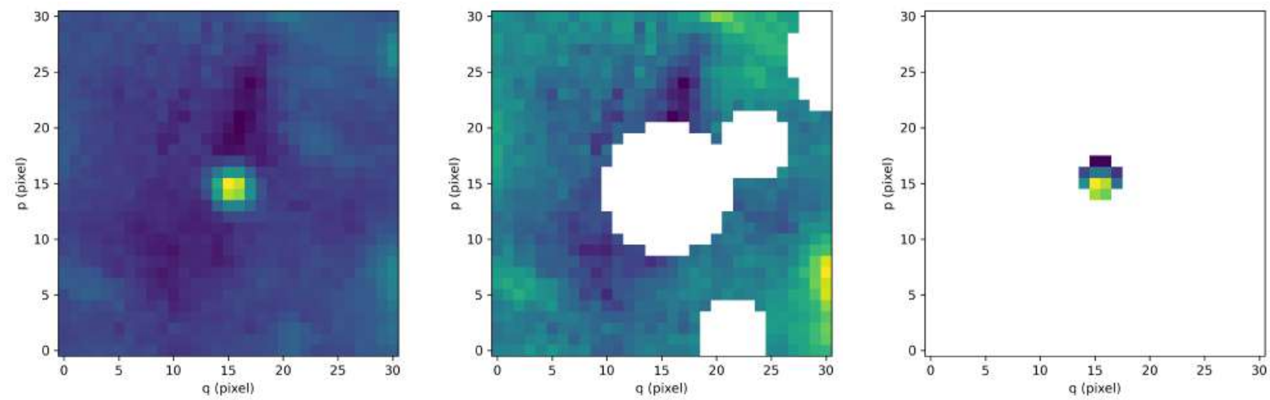


Figure 3.10: Example of the extraction procedure for the star ID=417, F814W=23.3. In the left panel, we show the square region around the star with a size of 31 spaxels per side. In the middle panel, we show the region with all detected sources masked. The remained unmasked spaxels are used to calculate the median local sky background spectrum. Finally, in the right panel, we show the spaxels used to obtain the weighted extracted spectrum of the star.

brighter stars, the region is a square of 31 spaxels per side, while for stars fainter than the TRGB, a square of 13 spaxels per side is used. In Figure 3.10, we show an example of the extraction procedure for the star ID=417, F814w=23.3. Within each selected square, all detected sources, including the target star, are masked. This masking ensures that only uncontaminated spaxels contribute to constructing the local background spectrum for each star. The local background spectrum is then created by taking the median of the available spaxels (i.e., unmasked) within each region. To determine the extraction radius per star and the minimum distance for calculating the local background, we analyzed the radial profiles of four stars with different magnitudes, as detailed in Table 3.2 and Figure 3.9. For the brightest star (F814W=21.52), the profile follows the PSF out to a distance of 6-7 spaxels before flattening, indicating the sky level that dominates the outskirts of stars. A star almost two magnitudes fainter follows the PSF to 4 spaxels before reaching the sky level. For two stars with magnitudes of 24.5, the profiles follow the PSF to 2 spaxels before dropping below it. Based on these profiles, the extraction radius varies from 4 spaxels (52 spaxels in total) for the brightest stars to 1 spaxel (4 spaxels in total) for stars fainter than the TRGB, ensuring that sky flux is not included in the extracted spectra. Additionally, the spectra are weighted by the PSF, meaning central spaxels contribute more to the flux than those further away.

The PSF-weighted spectrum extraction, coupled with the adaptive radius, ensures precise extraction of spectral information from stars across different brightness levels. After extraction, the locally calculated background spectrum is subtracted from each target star's spectrum. It is worth noting that there is a gap in radius between the extracted region of the target star and the region used to calculate the local sky background around each target star. For stars fainter than the TRGB this gap is 3 pixels, while for brighter stars above the TRGB, the radius increases to 5-6 pixels. This minimizes the possibility of oversubtraction, i.e. of including some flux from the target star itself into the local background estimate, reinforcing the purity of the extracted spectra.

For the outer disk field, we introduce two modifications to the extraction procedure due to the high density of stars and the limited availability of sky spaxels for calculating a reliable local sky background. Firstly, we extract the PSF-weighted spectrum using only 4 spaxels centered on each target star. Sec-

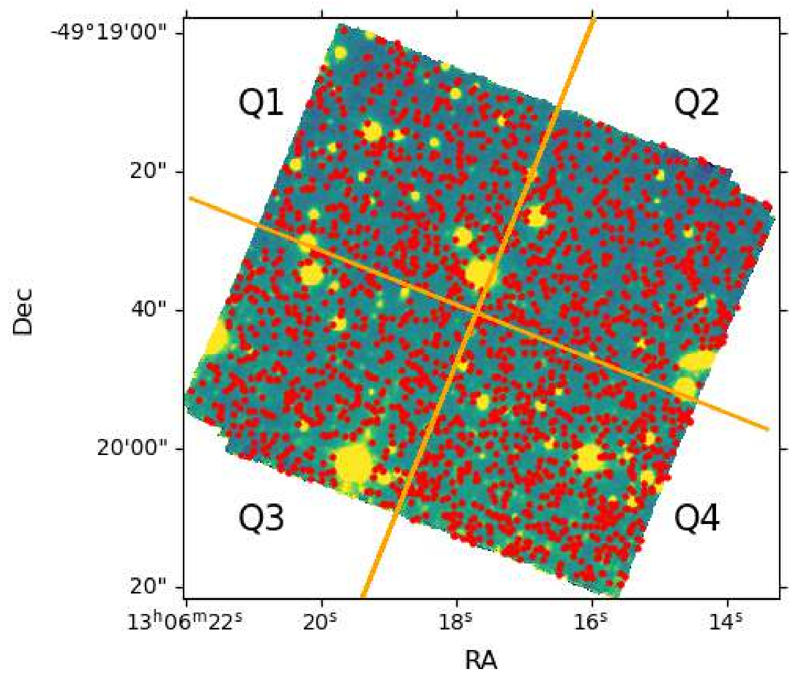


Figure 3.11: The outer disk field divided in four quadrants to calculate 4 different background spectrum.

ondly, we adopt a global sky background. For this purpose, we divide the outer disk field into four equal-sized quadrants as shown in Fig. 3.11 (Q1 and Q2 are in the upper left and right, while Q3 and Q4 are in the lower left and right) and assume that the sky background remains constant within each quadrant. We then estimate the sky background in each quadrant by calculating the median spectrum of the source-free spaxels, following the mask created for ZAP. Then, we subtract the quadrant-determined sky background spectrum from each extracted star spectrum based on its quadrant location. However, the number of source-free spaxels varies significantly between quadrants. Specifically, Q4, located closest to the galaxy disk has half the number of source-free spaxels as Q2. Consequently, due to the high crowding in Q4 and hence the rather unreliable determination of the sky background (4582 spaxels to estimate the background), we adopt the sky background estimated in Q2 for stars in Q4. This methodological adjustment, i.e., tailoring the background subtraction to the specific conditions of each quadrant, ensures a more reliable background subtraction in the outer disk field, enhancing the quality of the extracted spectra.

As an additional test, we also use the corresponding sky background spectrum calculated in Q4 for the target stars in Q4. The results obtained for the S/N and radial velocities for the stack spectra using this approach are quite similar (consistent within the errors) from those obtained by using the fiducial background subtraction. Nevertheless, given the higher crowding in Q4 due to its proximity to the disk, the likely presence of unresolved stars from NGC 4945 in that quadrant may contribute to the background there, which may result in a background spectrum containing information from the disk population. Subtracting this information from each star's spectrum could lead to information loss. In turn, we adopted the more conservative approach and decided to use the background from quadrant Q2 for the target spectra in quadrant Q4.

### 3.5.1 S/N for individual star's spectra

Once we extract each star's spectrum, we measure its S/N. To estimate the noise, we decided not to rely on the variance provided by the MUSE datacubes. This decision is based on findings from Bacon et al. (2017), which showed that the variance in the final MUSE datacubes contains correlated noise. This noise arises during the data reduction process, particularly from the interpolation used to construct the datacubes from the pixtables, and propagates throughout the procedure. Instead, we estimated the S/N directly from the extracted stellar spectra using the DERSNR code[3] (Stoehr et al., 2008). The S/N was calculated over the wavelength range 8400-8800 Å, which encompasses the calcium triplet (CaT) region. This method defines the signal (S) as the median flux in the selected spectral range and estimates the noise (N) using the third-order median absolute deviation (MAD). The MAD is computed from the differences between the flux at a given pixel and the flux at neighboring pixels spaced two pixels apart, assuming the flux distribution is Gaussian and uncorrelated across these intervals. Although this approach does not account for the full instrumental and detector-specific characteristics, it provides a uniform method for comparing the S/N across individual and stacked spectra. It has been widely adopted for kinematic studies of galaxies (e.g., Finlez et al., 2022; D'Ago et al., 2023; Comerón et al., 2023).

We analyzed the S/N as a function of stellar magnitude (Figure 3.12) and identified outliers deviating from the trend. A subset of stars exhibited significantly reduced S/N, and upon investigation, these stars were located near the edges of the field of view (FoV) in both the halo and outer disk fields. This S/N loss can be attributed to several factors: In the halo field, the combination of multiple OBs may result in lower effective integration times in peripheral regions, reducing sensitivity or causing incomplete data in specific wavelength ranges. Additionally, during the cube reconstruction process, some spectral pixels might be excluded due to the interpolation procedures used in data reduction. Furthermore, the intrinsic structure of the MUSE instrument, composed of 24 IFUs, could lead to incomplete spectral coverage at the boundaries between regions covered by each IFU, thereby affecting the quality of the spectral data in these areas.

In Figure 3.12 we show the resulting S/N per MUSE resolution element (2.5 Å) of each spectrum from uncontaminated stars (Sec. 3.4) selected in the red and blue boxes (see Fig.. 2.3) for the halo (top panel) and outer disk field (bottom panel), as a function of their magnitude. The vertical lines mark the magnitude of the TRGB. At this magnitude, we obtained a S/N $\sim$ 4 per resolution element for the halo field. For magnitudes fainter than the TRGB in the halo field, as we demonstrate below in Sec. 3.5.3, the S/N is not high enough to measure reliable individual radial velocities. For the outer disk field, the individual S/N obtained for each star is even lower. Consequently, the resulting spectra are very noisy, making it challenging to discern critical spectral features such as the CaT lines.

### 3.5.2 RGB and AGB stars spectral co-addition

To increase the S/N, we perform the co-addition of the individual star spectra, weighted by their corresponding S/N. This strategy assigns greater importance to the spectra with higher S/N, which contribute more signal. Specifically, within the halo field, we co-add the spectra of the RGB stars in the selection box, encompassing the region from the TRGB down to two magnitudes below. In the outer disk field, in addition to the RGB stars, we also stack the 70 AGB stars within the selection box illustrated in Fig. 2.3

[3] http://www.stecf.org/software/ASTROsoft/DER_SNR/der_snr.py

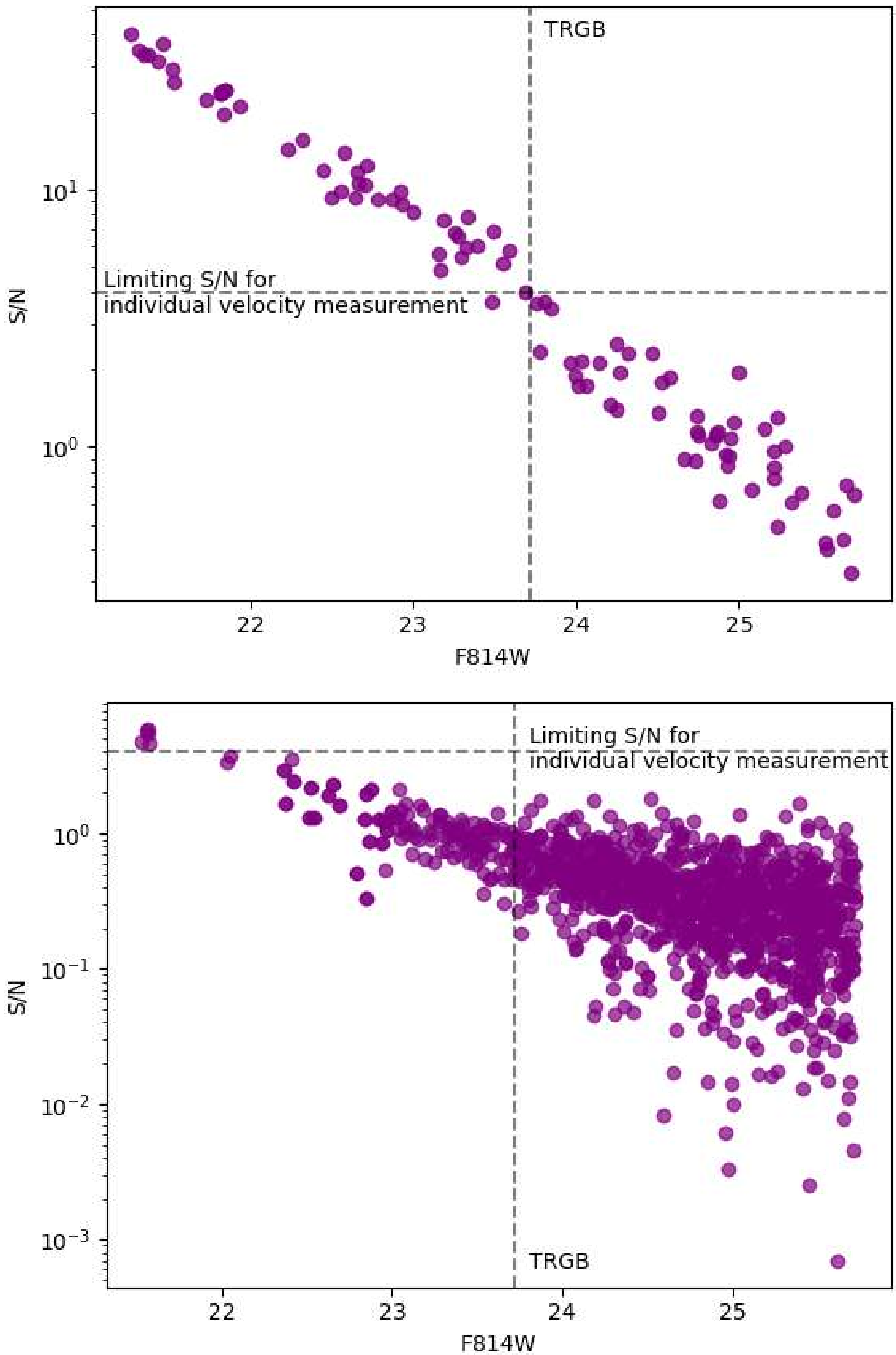


Figure 3.12: S/N per resolution element for each extracted spectra in the halo (top) and outer disk (bottom) fields measured in the CaT region 8400-8800Å. The vertical line in the upper/lower plot indicate the magnitude of the TRGB defined as the limit magnitude to measure individual velocities.

to increase the final S/N of the stacked spectrum. We generate four stack spectra for each field reaching down to different limiting magnitudes. Table 4.2 outlines the magnitude ranges, the number of stars employed for each combined spectrum, and their corresponding S/N reached in the final halo field stack. Similarly, Table 4.3 lists the same details for the outer disk field.

### 3.5.3 pPXF: measuring and testing velocities

Besides measuring the LOS velocities of the final stack, we also need to discriminate MW stars in the low density halo field from possible AGB stars belonging to NGC 4945 using their individual velocities. To derive the LOS radial velocities, we use the penalized pixel-fitting method (pPXF; Cappellari & Emsellem, 2004; Cappellari, 2017) to perform a full spectrum fitting, which consists of modeling an observed spectrum by a best-fitting linear combination of differently weighted stellar templates. pPXF has been extensively used to extract stellar or gas kinematics and stellar populations from absorption-line spectra of galaxies (e.g. when S/N is 20, Boardman et al., 2017). The pPXF method requires several inputs: a set of template spectra, the noise spectrum, and the starting value for the velocity and velocity dispersion $\sigma$ (the MUSE instrumental velocity dispersion is approximately 50 km $s^{-1}$).

We use the MUSE spectral library as stellar templates (Ivanov et al., 2019). This library was specifically constructed to match the spectral resolution of the MUSE instrument. It comprises a set of 35 standard stars that uniformly span all major sequences on the Hertzprung-Russel diagram, with $\sim 3-6$ bright stars per spectral type, except for O-type stars, where only one star is available. The spectra are shown in Figure 3.13 and have high S/N, ranging from 70 to 200.

The stars in this library cover a wide range of stellar temperatures, from 2600 and 33000 K, with $\log g$ values between 0.6 and 4.5, and [Fe/H] from $-1.22$ to 0.55. Since the library is constructed using MUSE data, it is inherently compatible with the instrumental effects of MUSE, making it an excellent choice for deconvolution processes in pPXF.

We vary the starting value for the velocity and its dispersion from 0 to 1000 km $s^{-1}$, as we show below.

We need to evaluate the confidence of our results in order to be able to distinguish MW stars from possible stars belonging to NGC 4945 above the TRGB in the halo field. Given that our observations are in a very low surface brightness and S/N regime, we performed two tests to check the stability and reliability of the velocity measurements obtained with pPXF for our particular data set, when measuring individual star velocities. First, we estimate the minimum S/N required to obtain reliable velocities using the entire wavelength range from 4800-8800 Å. Second, we evaluate the dependence of the resulting velocity on the starting value for the velocity used as input in pPXF.

To carry out the first test, aimed at determining the lowest S/N needed to achieve accurate velocity measurements, we selected a relatively bright and isolated MW star within our FoV with a magnitude F814W=22.58, a S/N$\sim$14 per resolution element and a measured LOS velocity of 13 km $s^{-1}$ obtained from a full spectrum fitting in the entire wavelength range. Then, we progressively add random Gaussian noise dependent on wavelength to the stellar spectrum: the magnitude of the perturbations is increased from a standard deviation of 0.1 to 0.9 in steps of 0.1, generating a total of 270 degraded spectra.

For each of these degraded spectra, we measure the new S/N and the LOS velocity, with a starting initial guess velocity of 200 km $s^{-1}$. In Fig. 3.14, we show the S/N vs the pPXF measured velocity for each of these spectra. The vertical blue line indicates the actual velocity of the star. It is evident that the

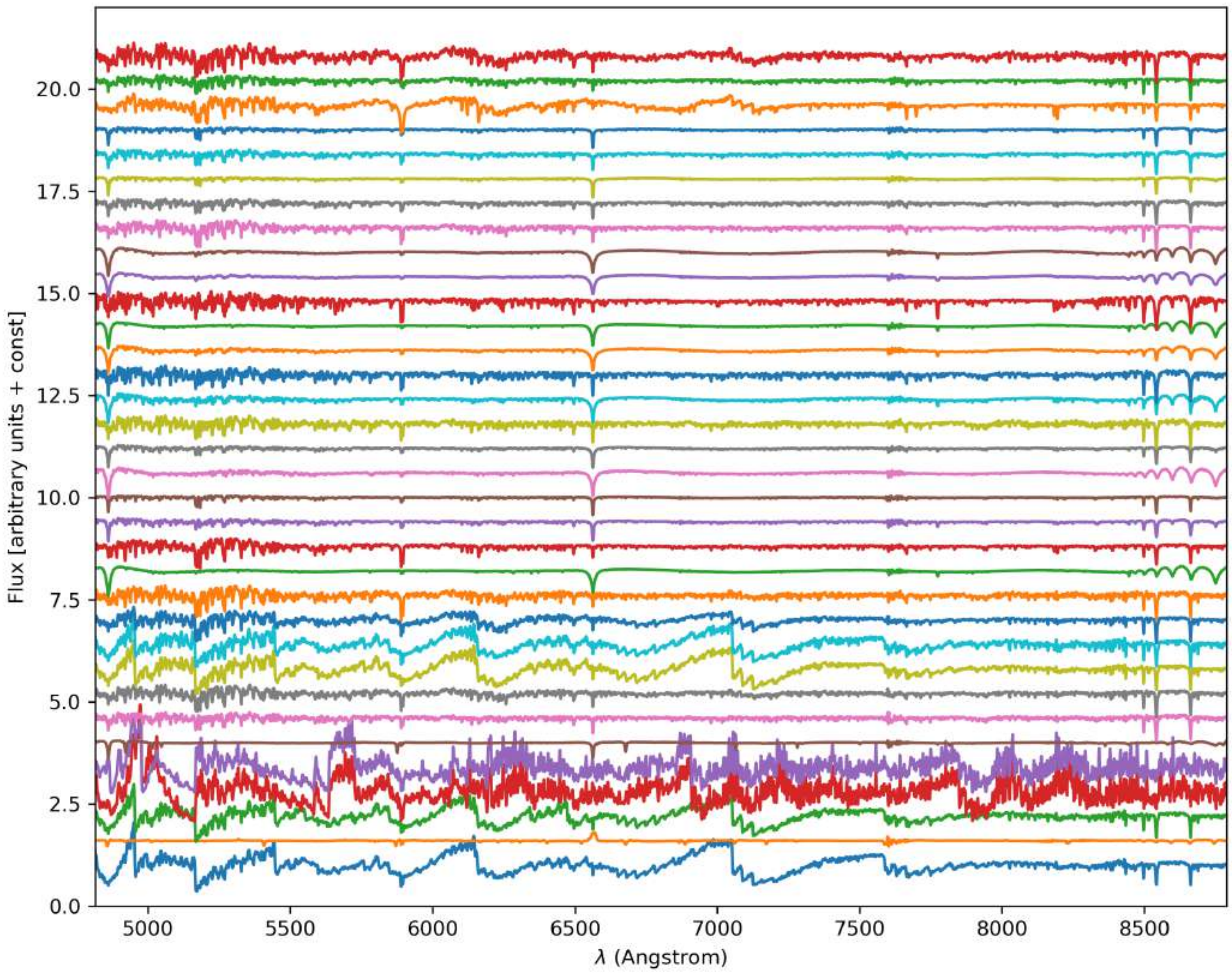


Figure 3.13: Spectra of the 35 stars used to construct the MUSE stellar library (Ivanov et al., 2019). The spectra are normalized and shifted up for clarity. These stars span all major sequences on the Hertzsprung-Russel diagram.

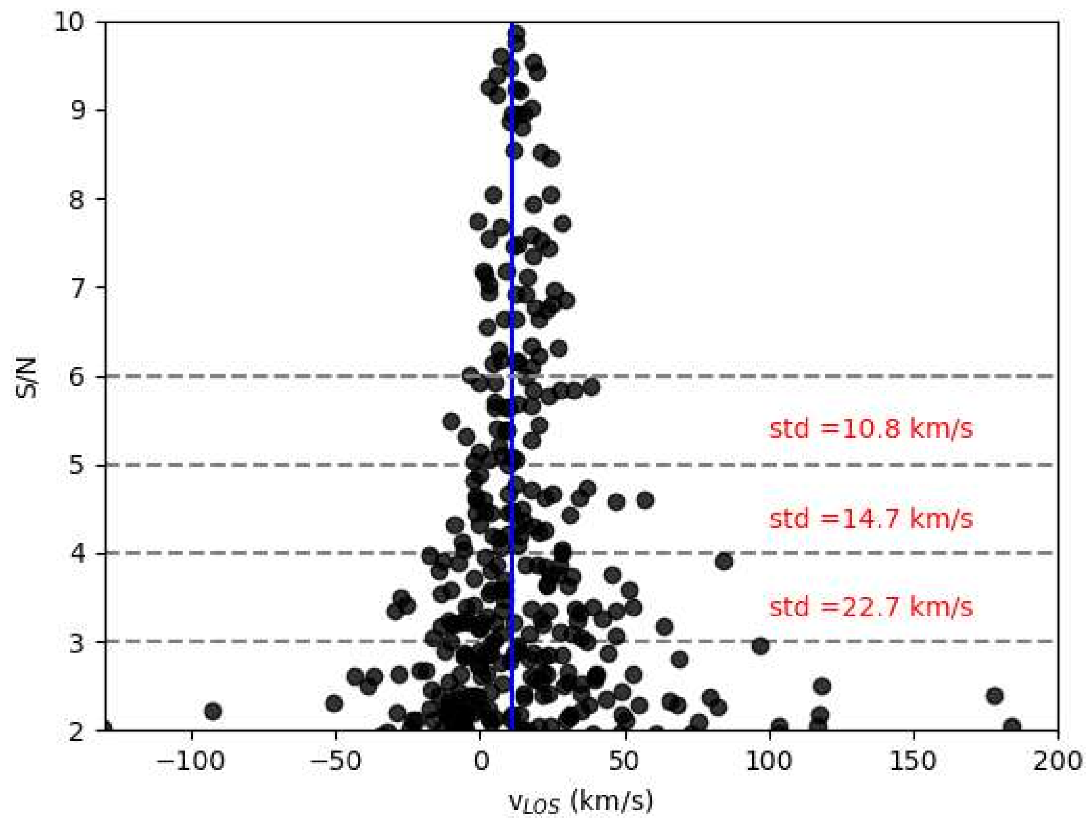


Figure 3.14: The scatter in the measurement of the velocity as a function of S/N for individual stars. We use an isolated bright star in the halo field, with F814W=22.58 and S/N=14 as the template. The vertical blue line is the radial velocity of the star obtained with pPXF, which is 12.2 km $s^{-1}$. In red we report the standard deviation at various levels of S/N, which decreases as the S/N increases.

scatter in the measured velocities widens as the S/N decreases. The scatter in the measured velocities gives us a sense of the uncertainty of the measured velocity for spectra of a given S/N level. Notably, the uncertainty in measured velocity experiences a stark increase below S/N<4. From our sample of RGB stars, only one exhibits a S/N>4, yielding a velocity measurement consistent with NGC 4945 (see below in Section 4.1). Stars with S/N>4 correspond to magnitudes above the TRGB as delineated by the vertical line in Fig. 3.12. Given our aim to differentiate MW stars, we decided that a S/N= 4 is the minimum S/N that we can use to obtain reliable velocity measurements for individual stars. Consequently, we can accurately determine velocities for stars brighter than the TRGB. This capability enables us to discern between most MW stars and potentially bright NGC 4945 stars. In the outer disk field, we do not have high enough S/N to be able to measure individual star velocities (see bottom panel in Fig. 3.12).

For the second test, i.e. how our velocity measurements depend on the initial guess velocities input in pPXF, we input 5 initial velocities: 0, 200, 400, 600, and 800 km s$^{-1}$. We measured velocities using the full wavelength range (4800 to 8800 Å) in stars brighter than the TRGB, both from the GHOSTS catalog and those detected by Gaia that are not in the GHOSTS catalog, for a total of 63 stars. For stars with magnitudes F814W $<$ 22.6, and S/N from 9 to 40, there is no variation in the velocity distribution measured when using different initial velocities.

For the 24 stars with magnitudes between F814W = 22.6 and the TRGB, the velocities obtained are more sensitive to the initial velocity guess, often tending to result in velocities close to the initial guess. Within this magnitude range, we anticipate the possibility of identifying at least one star belonging to NGC 4945, given the number of RGB stars in the halo field (see Harmsen et al. 2023). Among these stars, three emerge as strong candidates for belonging to NGC 4945. Two of these candidates consistently exhibit similar velocities across all tested starting points, while the third deviates significantly only when an initial guess of 0 km/s is used, registering velocities exceeding 400 km/s with other starting points. Additionally, several stars display velocities closely aligned with the chosen starting guess velocity. This is expected since pPXF uses a local minimization algorithm to converge in a local minimum. Given that in this magnitude range the individual S/N per star is lower, reaching the limit that gives us reliable velocities, this will cause the velocities obtained to be more dependent on the initial guess velocity.

In addition to testing the reliability of individual star measurements, we need to test the minimum S/N required to obtain a reliable velocity and velocity dispersion from a stacked spectrum. To do this test, we simulate a realistic stacked spectrum of RGB stars using a cool giant star of spectral type M3III from the MUSE spectral library (Ivanov et al., 2019) (S/N=79, velocity=19 km s$^{-1}$) as a template. We generated a random Gaussian distribution of 53 velocity values centered at 19 km s$^{-1}$ with a dispersion of 100 km s$^{-1}$. This distribution corresponds to the typical number of RGB stars used for the final stack in the MUSE halo field. The template spectrum is shifted according to the generated velocity distribution, effectively simulating spectra at different velocities. Each shifted spectrum is then assigned a noise level that is wavelength-dependent and based on the actual S/N distribution of RGB stars in the MUSE halo field (see Figure 3.12). The noise levels are applied by adding random Gaussian noise with values ranging from 0.2 to 1 in steps of 0.05. For each noise level, we generate 50 spectra, resulting in a total of 800 simulated spectra. Once noise is introduced, the spectra are combined using a weighted average based on their respective S/N values, following the method described in the previous section. Finally, we measure the S/N, LOS velocity, and velocity dispersion of the stacked spectrum at different noise levels.

Figure 3.15 shows the scatter in velocity and velocity dispersion as a function of decreasing S/N. We find that while the mean velocity of a stacked spectrum can be measured reliably at lower S/N, the

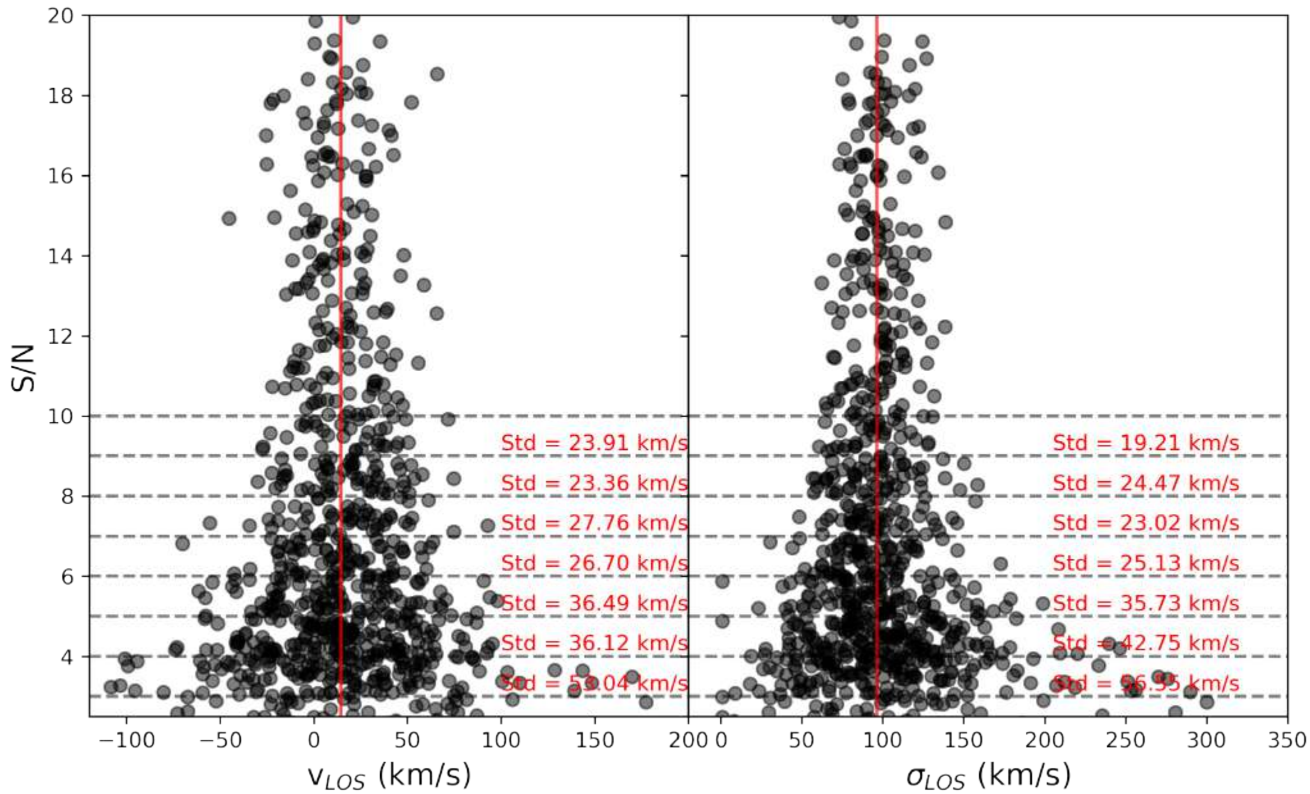


Figure 3.15: Scatter in the measurements of the velocity and velocity dispersion for stack spectra, resembling spectra of stacked RGB stars, as a function of S/N. The red vertical lines indicate the median values of velocity and velocity dispersion, 14 and 96 km $s^{-1}$ respectively. We also report the standard deviation at various levels of S/N, which decreases as the S/N increases.

second-order velocity dispersion measurement is more challenging. From this test, we conclude that reliable LOS velocity and velocity dispersion measurements can be achieved for stacked spectra with S/N>6.

To estimate the uncertainties in the measured LOS velocities—both for individual stars and the stacked spectra—as well as the uncertainties in the velocity dispersion of the stacked spectra, we performed 1000 Monte Carlo bootstrapping simulations (Cappellari, 2023). This method involves adding random noise proportional to the scatter of the residuals from the initial fit. First, we perform an initial pPXF fit to obtain the best-fit spectrum and calculate the residuals by subtracting the observed spectrum from the model. Then, we generate 1000 realizations by introducing random noise into the model, capturing the variability in velocity and velocity dispersion measurements.

# Chapter 4

# Resolved Stellar Halo Velocity Measurement of NGC 4945

As mentioned in Chapter 1, kinematic analyses of stellar halos with resolved stars have been restricted exclusively the MW and M31 until now.

In this Chapter, we present the results obtained from measuring the velocities of individual stars in the halo field of NGC 4945. This is the first time that the kinematics of a stellar halo in a galaxy outside the LG will be measured with resolved stars, allowing us to gather information about the origin of this galaxy's halo and whether it is dominated by accretion. We first show the results obtained from co-adding the spectra of individual stars, selected as described in Chapter 3, to obtain the mean velocity and velocity dispersion of the halo and outer disk fields of NGC 4945. Finally, we discuss some of the implications of the velocity values obtained in both fields and their relation to the accretion history of NGC 4945.

Based on Beltrand et al. (2024) A&A, 690, A115.
DOI: 10.1051/0004-6361/202450626

## 4.1 Individual star velocity measurements in the halo field

The spectra of bright stars in the MUSE halo field, particularly those exceeding the TRGB, exhibit S/N$\geq$4 per resolution element (Figure. 3.12). This ensures reliable velocity measurements, validated through our tests (Figure.3.14). We want to measure their individual velocities mainly to kinematically discriminate between MW foreground stars, prevalent due to the low Galactic latitude of NGC 4945, from NGC 4945 stars, especially those above the TRGB (see Figure 2.3).

We measured the LOS velocity of the 45 stars brighter than the TRGB in the halo field using pPXF, as described in Section 3.5.3. Their LOS velocity distribution is displayed in Figure 4.1. Of these, 40 stars have LOS velocities between $-100$ and 200 km s$^{-1}$, one has a LOS velocity of 202 km s$^{-1}$, another has a velocity of 329 km s$^{-1}$, and 3 stars exceed 400 km s$^{-1}$. In addition to the stars resolved by GHOSTS, we also measure the velocities of 18 bright high S/N stars detected by Gaia in our MUSE halo FoV. Their LOS velocities measured with pPXF give us a sense of the distribution of velocities of the MW foreground stars: 16 stars fall between $-150$ and 50 km s$^{-1}$, while two exhibit higher velocities (302 and 366 km s$^{-1}$, respectively; Fig.4.1).While most MW foreground stars have velocities distributed around 0 km s$^{-1}$, a small fraction can have extremely large velocities. The measured LOS velocities of

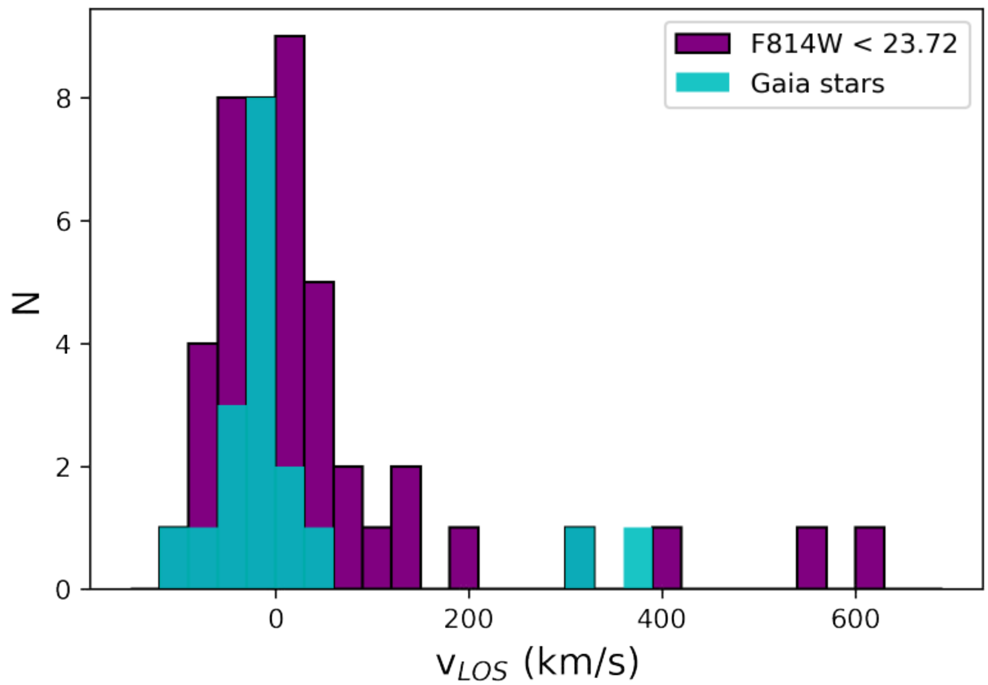


Figure 4.1: Velocity distribution of the halo field stars brighter than the TRGB (F814W = 23.72). Stars in the GHOSTS catalogue are shown in purple while stars detected by Gaia are shown in Cyan.

the Gaia stars support the assumption that the vast majority of stars with magnitudes brighter than the TRGB are indeed foreground MW stars, consistent with our expectations for this low-latitude FoV. Since the systemic heliocentric velocity of NGC 4945 is 563±3 km $s^{-1}$, and the Gaia stars have all velocities lower than 400 km $s^{-1}$, we define an upper limit of 400 km $s^{-1}$ to discriminate between MW and NGC 4945 stars. Thus, we consider stars with heliocentric LOS velocities greater than 400 km $s^{-1}$ to be candidates for being NGC 4945 stars.

Among these, three stars exceed 400 km $s^{-1}$, indicated in Figure 4.2 with green boxes. These stars lie in the range where velocity measurements depend on pPXF input parameters, as discussed in Section 3.5.3. Our different tests, however, demonstrated stable LOS velocities irrespective of initial input (0 to 800 km $s^{-1}$, spaced by 200 km $s^{-1}$), making them strong candidates for NGC 4945 membership. Their properties are summarized in Table 4.1 and marked as green squares in the CMD (Fig. 4.2).

However, we applied the different tests described in Section 3.5.3 to these three stars in particular and found that these three stars have very stable LOS velocities, regardless of the initial guess velocities used (from 0 to 800 km $s^{-1}$ spaced by 200 km $s^{-1}$). Based on kinematics alone, these stars are strong candidates to belong to NGC 4945; their main properties are listed in Table 4.1 and they are highlighted as blue squares in the CMD presented in Figure 2.3 (left panel).

Figure 4.3 shows the spectra (and their respective smoothed spectra) and pPFX best fit for these three stars. The reddest star (ID=417), with a LOS velocity of 630±16 km $s^{-1}$, is within the AGB selected region of the CMD. Its spectrum shows molecular bands indicative of a low temperature star of a spectral type M. The bluest star (ID=236), with a LOS velocity of 548±61 km $s^{-1}$, aligns closely with NGC 4945's systemic velocity. A third star (ID=210), with a velocity of 425±27 km $s^{-1}$, exhibits

Table 4.1: Positions (RA and Dec), magnitude, color, S/N and LOS velocities for the individual 3 stars brighter than the TRGB which are candidates to belong to NGC 4945 based on their measured LOS velocities.

| ID | 236 | 210 | 417 |
|---|---|---|---|
| RA (h:m:s) | 13:07:40.5 | 13:07:43.9 | 13:07:41.1 |
| Dec (d:m:s) | -49:03:30.0 | -49:02:46.9 | -49:02:41.3 |
| F814W (mag) | 23.2 | 22.7 | 23.3 |
| (F606W-F814W) | 0.4 | 1.0 | 2.1 |
| S/N | 5.5 | 9.4 | 4.5 |
| $v_{LOS}$ (km $s^{-1}$) | 548±61 | 425±27 | 630±16 |

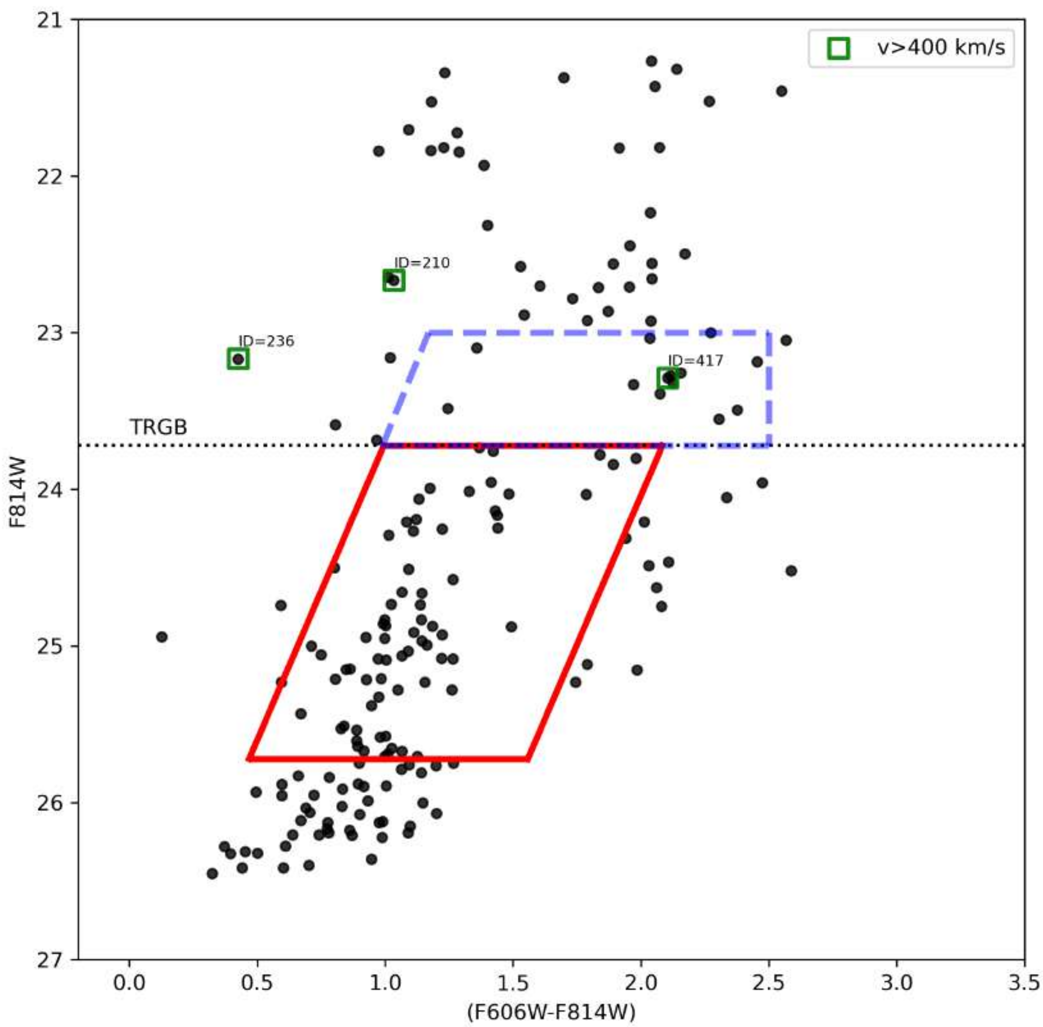


Figure 4.2: Halo CMD with red and blue boxes are the same as Figure 2.3. Green small boxes mark the stars with individual heliocentric LOS velocities greater than 400 km $s^{-1}$.

CaT lines and a redward flux increase. While the spectra of ID=236 and ID=210 lack molecular bands, consistent with their bluer color (i.e., higher temperature), their CMD positions suggest these are likely Blue Helium-burning (BHeB) and Red Helium-burning (RHeB) stars, respectively. ID=236 also shows Hβ and HeI lines, consistent with a B-type star.

Nevertheless, we cannot rule out the possibility that these could be high-velocity foreground MW stars. However, the likelihood of these being high-velocity MW stars is minimal, considering the low number of MW stars with v>400 km s$^{-1}$. Of the 5000 Gaia stars with magnitud G<15 and radial velocity measurements in a $2 \times 2$ square degree region around the MUSE halo FoV, only two have velocities >400 km s$^{-1}$ (431 km s$^{-1}$ and 605 km s$^{-1}$), yielding a fraction of 0.0004. For a 1 arcmin$^2$ FoV this translates to a negligible probability (0.0072 stars). None of the 18 Gaia stars in the MUSE FoV exceed 400 km s$^{-1}$, supporting the association of these three stars with NGC 4945.

We will discuss the implications of these three stars belonging to NGC 4945 in the Discussion Section 4.4, taking into consideration the results of the mean halo velocity and outer disk field, which we present below.

## 4.2 Velocity of the halo field from stacked RGB stars

We now measure the velocity of our stacked RGB halo stars using pPXF. In brief, as we explain in Section 3.5.2, we co-added the spectra of RGB stars (that were not significantly contaminated by neighboring sources) extending to 2 magnitudes below the TRGB: we generated 4 stacks reaching down to four limiting magnitudes, including progressively fainter stars with lower S/N. In Table 4.2, we list the magnitude range, the number of coadded RGB stars, the achieved S/N, and the heliocentric LOS velocities and velocity dispersions measured by pPFX with their corresponding uncertainties for each stacked spectrum. The four stacked spectra exhibit LOS velocities ranging from 515 to 537 km s$^{-1}$. The S/N in all four stacks is consistently above 8. However, the increase in S/N is not linear with increasing limiting magnitude (i.e., the increasing number of stars), implying that we might be adding more noise than signal. Nevertheless, considering that the variations in the obtained LOS velocity are not very pronounced, and the S/N values are also relatively stable across the stacks, we adopt the stack N°4 as the fiducial stack. This decision is based on it having the highest number of stars. The uncertainties reported are calculated from the Monte Carlo bootstrapping method presented in Section 3.5.3. We note that we do not normalize the individual spectra before the stacking procedure. See Appendix A for the results considering the previous normalization.

The top panel of Fig. 4.4 displays the halo spectrum in grey. The blue line represents the best-fitting spectrum obtained using pPXF, while the red line illustrates the smoothed spectrum. The smoothing process employs a Gaussian Kernel with a sigma of 2 pixels and is weighted by the inverse variance of the sky spectrum. The bottom panel of this Figure is a zoom in the CaT region in which we can see that the two strongest CaT lines are very clear in the spectrum.

We obtain a mean LOS velocity of $519 \pm 12$ km s$^{-1}$ and a velocity dispersion of $42 \pm 22$ km s$^{-1}$ for the halo field. We emphasize that this is the *first ever measurement of the kinematics of a diffuse stellar halo outside the Local Group obtained from its resolved stars*. This halo field LOS velocity measurement is within $\sim 40$ km s$^{-1}$ of the systemic velocity of $563 \pm 3$ km s$^{-1}$ for NGC 4945 (Koribalski et al., 2004). Considering that NGC 4945 is edge-on, its measured LOS velocity on the major axis subtracted from its systemic velocity can be considered its rotational velocity. This is $-44 \pm 12$ km s$^{-1}$, meaning that at this

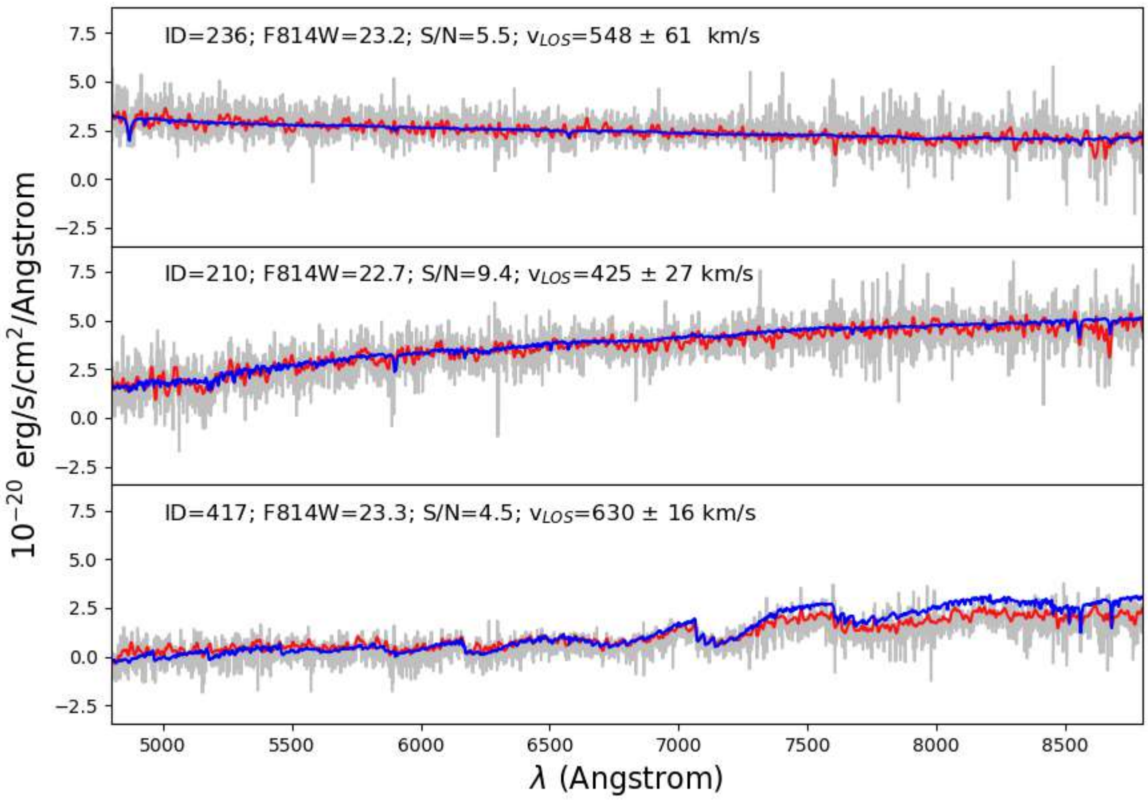


Figure 4.3: Individual spectra of the three candidate stars (grey) that belong to NGC 4945, according to our velocity criteria to discriminate foreground MW stars, with their respective best fit obtained with pPXF (blue). In red we show the spectra smoothed by a Gaussian kernel of 3 pixels weighted by the inverse variance of the sky spectrum.

Table 4.2: Halo stacked of RGB stars at different magnitude levels as described in Sec. 4.2. The listed uncertainties are measured by running 1000 Monte Carlo bootstrapping simulations.

| Stack N° | F814W | N # | S/N | $v_{LOS}$ (km $s^{-1}$) | $\sigma$ (km $s^{-1}$) |
|---|---|---|---|---|---|
| 1 | 23.72 – 24.72 | 14 | 8.9 | $537 \pm 16$ | $48 \pm 27$ |
| 2 | 23.72 – 25.00 | 28 | 9.8 | $515 \pm 14$ | $53 \pm 22$ |
| 3 | 23.72 – 25.50 | 43 | 9.7 | $517 \pm 13$ | $46 \pm 23$ |
| 4 | 23.72 – 25.72 | 53 | 9.4 | $519 \pm 12$ | $42 \pm 22$ |

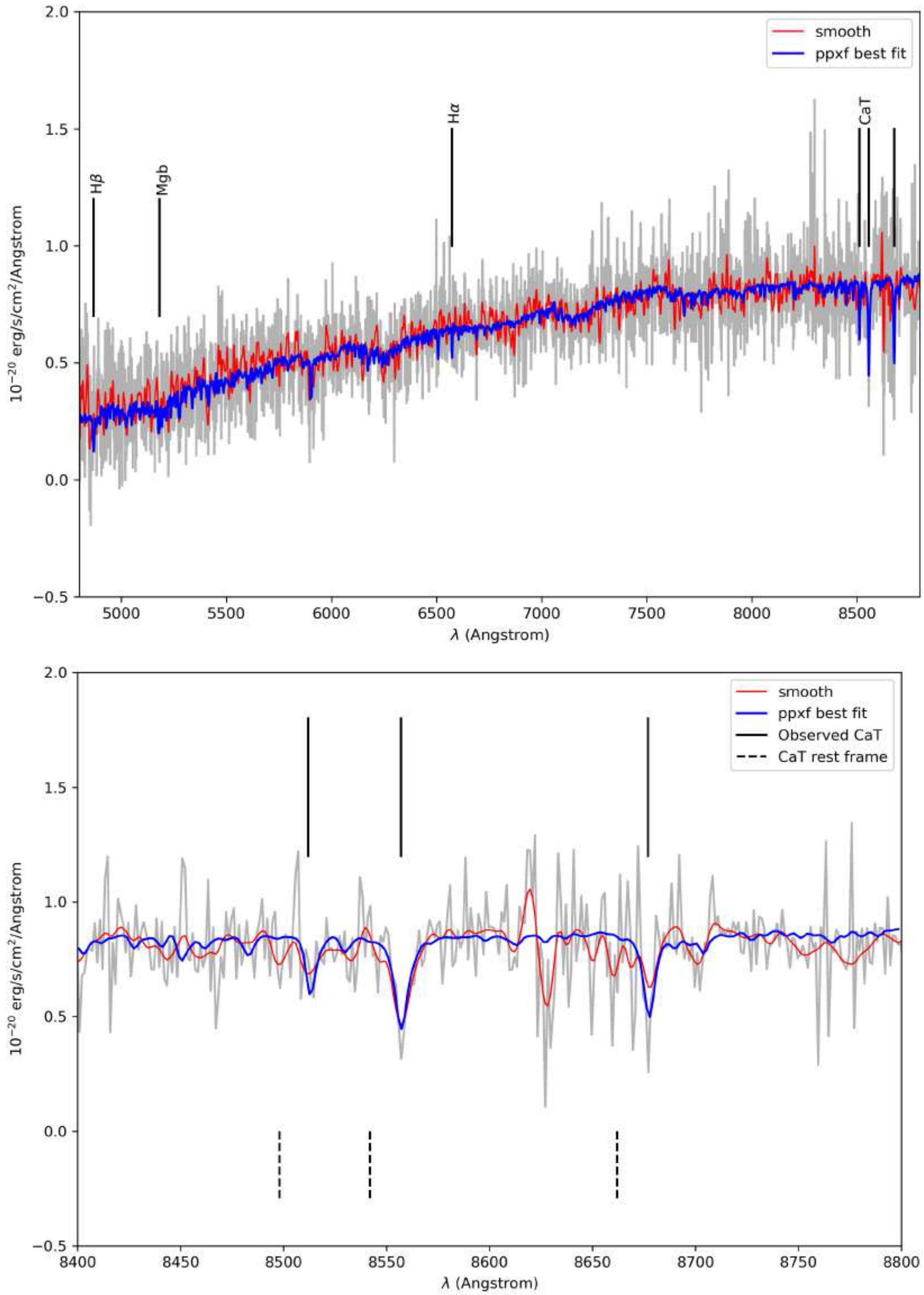


Figure 4.4: The stacked halo spectrum: Co-added spectrum of 53 halo RGB stars with F814W magnitude brighter than 25.72. Red: Co-added spectrum smoothed by a Gaussian kernel of 2 pixels weighted by the inverse variance of the sky spectrum. Blue: The best fit from pPXF. In the upper panel we show the full spectrum wavelength, 4800-8800 Å, used to measure velocity with pPXF, in the bottom panel we show a zoom in the CaT region and mark with black dashed lines the position of these lines: 8498, 8542 and 8662 Å in the restframe and in black solid lines the position of the observed CaT lines.

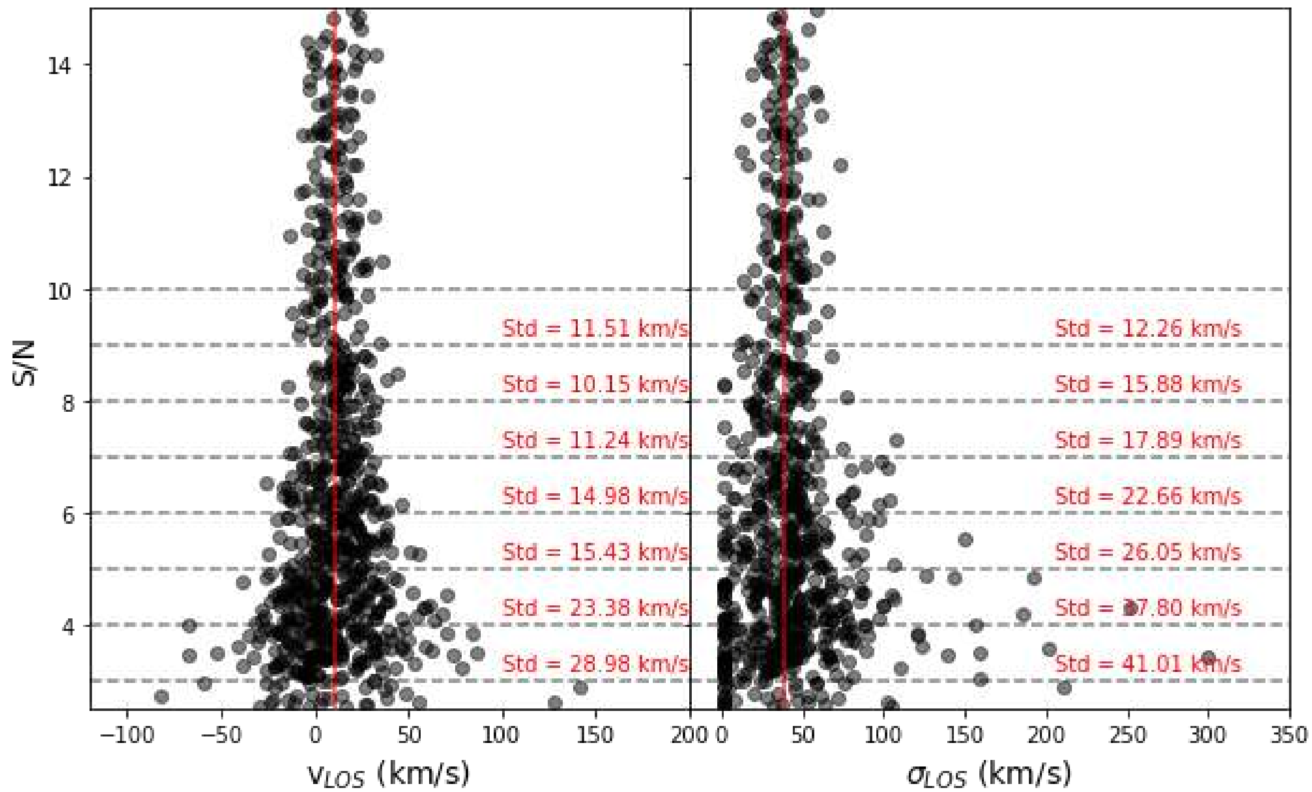


Figure 4.5: Scatter in the measurements of the velocity and velocity dispersion for stacked spectra with a dispersion of 40 km $s^{-1}$, resembling spectra of stacked RGB stars, as a function of the S/N. The red vertical lines indicate the median values of velocity and velocity dispersion, 11 and 39 km $s^{-1}$ respectively. We also report the standard deviation at various levels of S/N, which decreases as the S/N increases.

distance the halo is counter-rotating. This result suggests clear evidence of an accreted stellar halo at that distance. We will discuss the consequences of this result in Section Discussion 4.4.

We note that our velocity dispersion (42±22 km $s^{-1}$) is below the MUSE velocity resolution (∼50 km $s^{-1}$). To assess the ability of pPXF to recover this type of velocity dispersion, we performed the same test as that shown in Fig. 3.15, but using a Gaussian distribution with a width of 40 km $s^{-1}$; namely, we generated a mock stack spectrum of RGB stars with a velocity dispersion of 40 km $s^{-1}$, mimicking the velocity dispersion we obtained in the halo field. We found that pPXF successfully recovers the input velocity dispersion of 40 km $s^{-1}$ in that test, providing a median value of 39 km $s^{-1}$, as shown in Figure 4.5. This demonstrates the code's ability to accurately retrieve low velocity dispersion values, particularly for spectra with S/N>8, as these are extracted from the best fit the code produces to the real spectrum. For stacked spectra with S/N≤ 8, the possibility that pPXF may either fail to measure the velocity dispersion (resulting in a value of 0) or mismeasure it increases significantly (providing values much higher than 40 km $s^{-1}$).

Unfortunately, the S/N of our stacked spectra is not high enough to reliably measure a velocity dispersion lower than the MUSE resolution. As shown in Fig. 7 of Iodice et al. (2023), it is possible to measure velocity dispersions below the MUSE resolution, but only when the S/N is sufficiently high (S/N>15).

Given our low S/N, our measured value of 42±22 km $s^{-1}$ represents only an upper limit of the actual velocity dispersion in our halo field.

Additionally, since there are three stars brighter than the TRGB that are possibly NGC 4945 stars (see previous section), we examine the resulting velocity when adding them to the combined spectrum. We generated a new stacked spectrum by incorporating these three stars into stack N° 4, resulting in a final S/N of 14.5 and a velocity and velocity dispersion of 510 ± 13 km $s^{-1}$ and 71 ± 18 km $s^{-1}$, respectively.

## 4.3 Velocity of the outer disk field from the stacked spectrum

The low S/N of individual stars in the outer disk field prevents us from kinematically distinguishing MW foreground stars from stars members of NGC 4945. However, this is not a problem for the outer disk field since the number of MW foreground stars is negligible compared to the number of RGB and, especially, AGB stars in NGC 4945 (see Fig. 2.3). This contamination can be roughly estimated from the Trilegal simulation: 10 predicted MW foreground stars vs. 91 stars that we have in total in the AGB box region in Fig. 2.3, which accounts for a contamination of less than 20%. Along with a clear and well populated RGB, we can discern a clear AGB population in the disk field. Considering that we have 1 or 2 AGB star candidates in the halo field where there are 68 RGB stars down to 2 magnitudes below TRGB, we estimate that there should be, in proportion, at least 53 AGB stars in the outer disk field, given that there are 1835 RGB stars within the RGB box. This estimate is consistent with what we see in the CMD (Fig. 2.3). Nevertheless, to avoid MW star contamination as much as possible, we decide to be conservative in the color of the AGB region considered to do the stack, with a red limit of 2.5, since MW contamination is higher in the redder part of the AGB (see Monachesi et al. 2016b).

As mentioned in Section 3.5 , to analyze this field we first divide it into 4 quadrants: The upper and lower left (Q1 and Q3 respectively) and the upper and lower right (Q2 and Q4), as shown in Fig.2.2. This is because the crowding of the field increases significantly from Q1 to Q4, thus the background in each of these quadrants is also different. In each of the quadrants we select all the RGB/AGB stars free of contamination from neighbor stars (as explained in Sec. 3.4) and combine their spectra. We also generate, as in the halo field, four distinct stacked spectra, each including RGB stars with fainter magnitudes, reaching down to 2 mag below the TRGB. All 70 AGB stars are included in each of the stacks. Table 4.3 displays the number of RGB stars used in each combined spectrum, the S/N of the combined spectrum with both RGB and AGB stars (values within parentheses represent the results considering only the RGB stars), and the measured LOS velocities and velocity dispersion values. We highlight that across all stacks, the obtained LOS velocity values exhibit stability, with differences of less than 6 km $s^{-1}$ between them. Additionally, we find that, even though the shallow outer disk field has a much lower exposure time than the halo field, the higher density of RGB and AGB stars belonging to NGC 4945 compared to the halo field compensates in a way that it is possible to obtain a final co-added spectrum with a much higher S/N (∼16) compared to the latter (∼9).

For consistency, to select the spectrum that best represents the outer disk, we base our choice on the one with the highest number of stars in its stack, as we did for the halo. Stack N°4 meets this requirement, having a S/N = 16.7, so this will be used as representative for our analysis. The top panel of Fig. 4.6 shows the combined outer disk field spectrum of the stack N°4 in Table 4.3. We also show the smoothed spectrum in red using a Gaussian kernel of 2-pixel weighted by the inverse variance of the sky spectrum. Finally, we show the best fit calculated by pPXF as blue line. The bottom panel shows

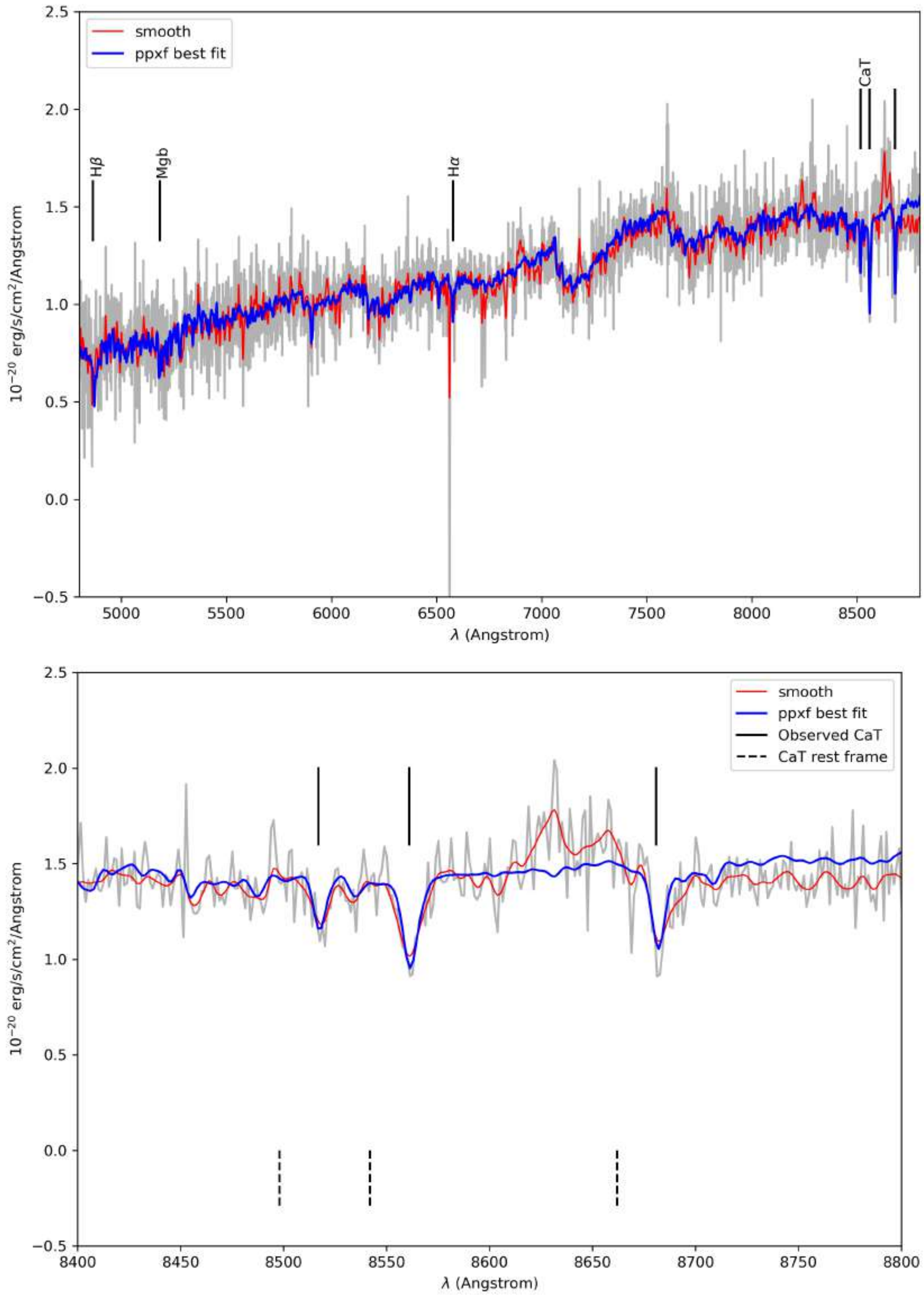


Figure 4.6: The stacked outer disk spectrum: Grey represents the median co-added spectrum of AGB plus RGB stars with F814W magnitude brighter than 25.72. Red: Co-added spectrum smoothed by a Gaussian kernel of 2 pixels weighted by the inverse variance of the sky spectrum. Blue: The best fit from pPXF. In the upper panel we show the full spectrum wavelength, 4800-8800 Å, used to measure velocity with pPXF, in the bottom panel we show a zoom in the CaT region and mark with black dashed lines the position of these lines: 8498, 8542 and 8662 Å in the restframe and black solid lines the position of the observed CaT lines.

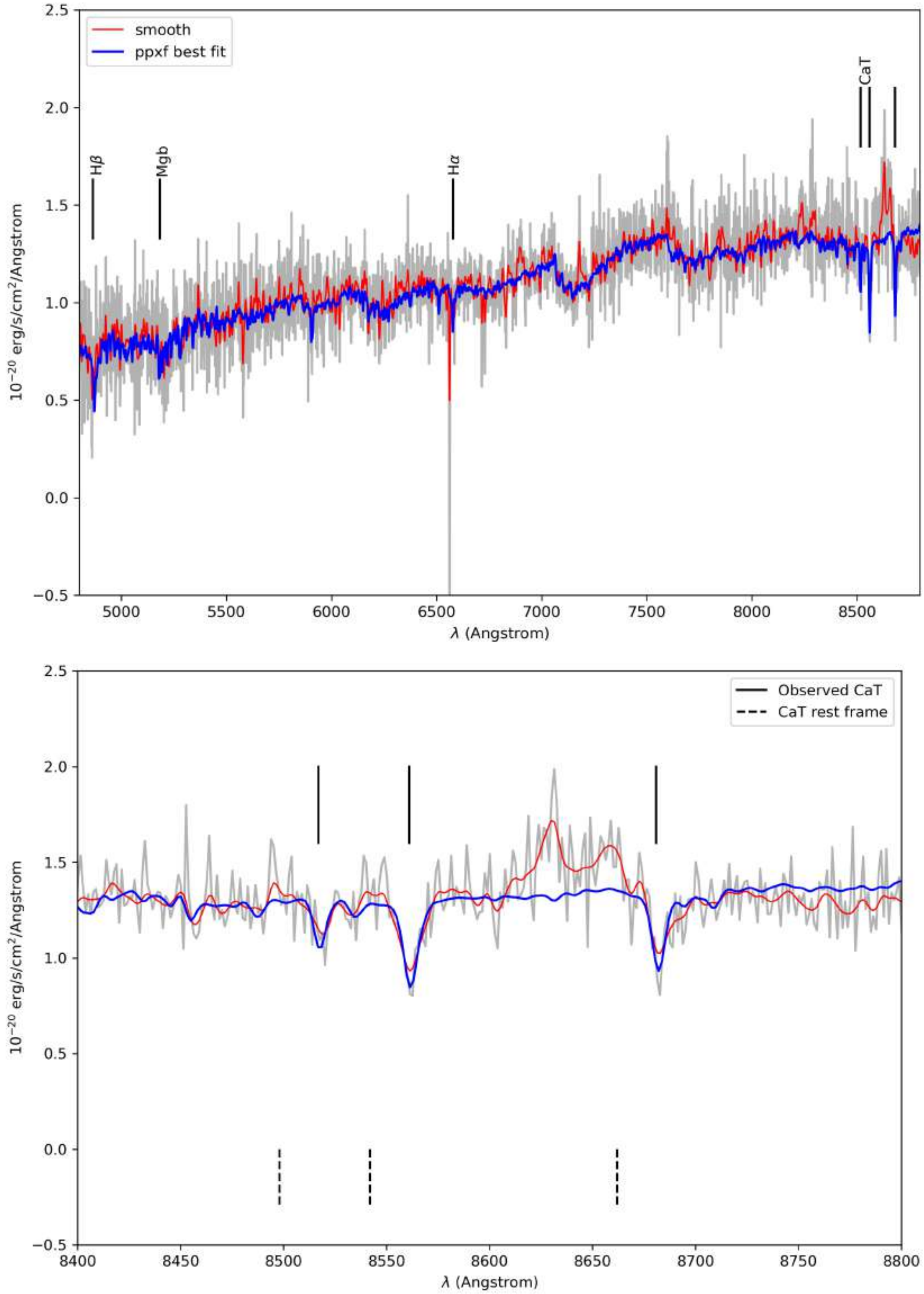


Figure 4.7: The stacked outer disk spectrum using RGB stars with F814W magnitude between the TRGB and 25.72. Colors and labels are the same as in Fig. 4.6. In the upper panel we show the full spectrum wavelength, 4800-8800 Å, used to measure velocity with pPXF, in the bottom panel we show a zoom in the CaT region.

Table 4.3: Outer disk stacked of 70 AGB plus RGB stars at different magnitude levels. The values of S/N, velocity, and velocity dispersion are obtained by considering the stacking of RGB and AGB stars. The values within parentheses are considering only the stack of RGB stars. The listed uncertainties are measured by running 1000 Monte Carlo bootstrapping simulations.

| Stack N° | F814W (mag) | RGB # | S/N | $v_{LOS}$ (km $s^{-1}$) | $\sigma$ (km $s^{-1}$) |
|---|---|---|---|---|---|
| 1 | 23.72 – 24.72 | 427 | 16.2 (14.9) | $667 \pm 11$ ($675 \pm 13$) | $76 \pm 16$ ($71 \pm 19$) |
| 2 | 23.72 – 25.00 | 622 | 15.6 (14.6) | $670 \pm 12$ ($678 \pm 12$) | $79 \pm 15$ ($72 \pm 17$) |
| 3 | 23.72 – 25.50 | 989 | 16.3 (14.7) | $671 \pm 11$ ($676 \pm 12$) | $76 \pm 15$ ($74 \pm 17$) |
| 4 | 23.72 – 25.72 | 1122 | 16.7 (14.8) | $673 \pm 11$ ($677 \pm 11$) | $73 \pm 14$ ($71 \pm 16$) |

the zoom-in of this spectrum in the CaT region, where the three lines are clearly detected. We obtain a mean heliocentric LOS velocity of $673 \pm 11$ km $s^{-1}$ for the outer disk field, which is in good agreement with the average velocity obtained from the mean HI gas velocity of the disk [1] ($\sim$700 km $s^{-1}$, Koribalski et al., 2018) near the position of our target. Given the high S/N of this final stack, and the results of the tests performed in Section 3.5.3, we can trust the velocity dispersion measurement obtained for this field, which is $73 \pm 14$ km $s^{-1}$.

As a consistency check, we also derived the LOS velocity of the outer disk field using only RGB stars. In Figure 4.7 we show the stacked spectrum with only RGB stars, generated in the same way as the final outer disk field with RGB+AGB stars. We found that the combined spectrum using only RGB stars has a lower S/N, as expected (see Table 4.3), however, the CaT lines are very distinguishable and the obtained LOS velocity is $677 \pm 11$ km $s^{-1}$, consistent with that obtained when also the AGB stars are combined.

## 4.4 Discussion

In this Chapter, we measured the median LOS heliocentric velocities of two fields along the major axis of the edge-on galaxy NGC 4945, positioned at 12.2 kpc (outer disk) and 34.6 kpc (halo) from the center of NGC 4945, by stacking their RGB and AGB stars. Since NGC4945 is edge-on, its measured velocities along the major axis can be regarded as its rotational velocity. Our findings reveal that the field at 12.2 kpc has a LOS velocity of $673 \pm 11$ km $s^{-1}$, in agreement with the velocity of the gas in a nearby position, which is $\sim$700 km $s^{-1}$ (Koribalski et al., 2018). This suggests that the stars in the outer disk field are rotating and are an extension of the disk of the galaxy. On the other hand, the field at 34.6 kpc, representing the stellar halo, displays a LOS velocity of $519 \pm 12$km $s^{-1}$, which is $\sim$40 km $s^{-1}$ lower but consistent with the systemic velocity of NGC 4945 ($563 \pm 3$ km $s^{-1}$, Koribalski et al., 2004). Consequently, at this distance, the stellar halo of NGC 4945 does not show signatures of strong rotation and it appears to be counter-rotating, implying that this is an accreted halo. Within the halo field, we also identified three stars, brighter than the TRGB, with LOS velocities exceeding 400 km $s^{-1}$. These stars

[1] https://www.atnf.csiro.au/research/LVHIS/data/LVHIS043.info.html

are potential candidates for belonging to NGC 4945, and if so these are likely a BHeB, an RHeB, and an AGB star, based on their positions in the CMD and their spectra.

In this Section, we present a global picture of NGC 4945 stellar halo, combining our results within the existing knowledge of the stellar halo of NGC 4945 from previous work and including a discussion of the three bright stars possibly belonging to NGC 4945 stellar halo. We contextualize our results of the stellar halo of NGC 4945 in comparison with the results obtained for the stellar halos of MW and M31 – the only other two galaxies for which there are velocity measurements of their halos based on individual RGB stars. We then discuss the limitations of our employed technique and the possibilities of using this technique to measure kinematics in other galaxies.

### 4.4.1 A global picture of NGC 4945

The stellar halo of the MW-like galaxy NGC 4945 has been studied by the GHOSTS survey (Monachesi et al., 2016b; Harmsen et al., 2017). Harmsen et al. (2017) derived the density profile of NGC 4945 stellar halo, which is found to decrease as a power law at a similar rate in both axes, with slopes -2.73 and -2.72 measured up to a distance of approximately 40 kpc. They also found an oblate stellar halo shape with a projected axis ratio of $c/a \sim 0.52$ at a galactocentric distance of ∼25 kpc. They estimated the total mass of the stellar halo to be approximately $3.5 \times 10^9$ $M_\odot$, which is about 9% of the galaxy's total stellar mass. We highlight that NGC 4945 exhibits a stellar halo mass and halo metallicity typical for a MW-like galaxy (Harmsen et al., 2017). Thus, in this work, we are characterizing kinematically a typical stellar halo for a MW-like galaxy.

On the other hand, Monachesi et al. (2016b) found a weak RGB color gradient in the stellar halo along the major axis of NGC 4945. This corresponds to a decrease in metallicity [Fe/H] from -0.8 (∼15 kpc) to -0.95 dex (∼45 kpc). It is interesting to note that the metallicity along the major axis of the stellar halo is similar to that found on the minor axis, which is rather flat, corresponding to a halo metallicity of [Fe/H] of -0.9 dex (Monachesi et al., 2016b). Models suggest that the contribution of the in situ halo beyond 10 kpc along the minor axis is minimal. The similarity of the metallicities on the minor and major axis of NGC 4945 halo implies that the stellar populations along the major axis beyond 20 kpc resemble the accreted stellar population along the minor axis. The flat metallicity gradient might indicate the contribution of a few (between three and ten) significant satellites at this distance (Cooper et al., 2010; Monachesi et al., 2019).

Our measurement of the LOS velocity of the halo field at 34.6 kpc along the major axis of NGC 4945, $519 \pm 12$ km $s^{-1}$, given the systemic velocity of $563 \pm 3$ km $s^{-1}$, shows, for the first time, a counter-rotating halo, thus of an accreted origin. We highlight that NGC 4945 is an edge-on galaxy; thus, its measured LOS velocity on the major axis is a good representation of its tangential velocity. This finding is particularly significant given the flattened nature of NGC 4945 halo, challenging the conventional expectation of rotation for such flattened halos (see e.g., the highly rotating accreted stellar halo of M31 Ibata et al. 2005; D'Souza & Bell 2018). Our result then demonstrates the existence of a flattened, accreted halo counter-rotating. Importantly, we emphasize that reaching such conclusions would have been impossible without the kinematic information we obtained in this work. Additionally, our measurements reveal a velocity dispersion of $42 \pm 22$ km $s^{-1}$ for NGC 4945 in our MUSE halo field. This velocity dispersion is lower than the typical values of velocity dispersion for halos of ∼100 km $s^{-1}$ (see Chapter 5 for a comparison with cosmological simulations). The lower velocity dispersion could stem from our measurement capturing a segment of a colder halo component, consistent with its flattened shape and the counter-rotation of $\sim 40 \pm 12$ km s$^{-1}$ along the major axis. We need more spectroscopic observations into the halo of NGC 4945 to confirm this.

Our measured LOS velocity for NGC 4945 at $\sim$12.2 kpc along its major axis is 673$\pm$11 km s$^{-1}$. After being corrected by its systemic velocity, we obtained a value of 110 km s$^{-1}$, which is a good proxy of the rotational velocity of the galaxy, given its edge-on configuration. Although our measured velocity of 673 km s$^{-1}$ is slightly lower than the one measured in the disk using HI gas in a nearby position, this could be due to a potential contribution from the accreted halo component at this distance. We measured that the accreted halo component, at $\sim$35 kpc along the major axis, has a velocity of 519$\pm$12 km s$^{-1}$, lower than the systemic velocity of the galaxy, so this component might also be present at 12 kpc in the outer disk field, although it would be less dominant compared to the in situ component, thereby influencing the obtained LOS velocity. Regardless, we conclude that the in situ component is dominating at this distance.

Combining all the results, we can obtain a global observational picture of the stellar halo of NGC 4945. This is a relatively massive ($\sim$3.5$\times$10$^9$ M$_\odot$) and metal-rich (-0.9 dex) stellar halo, typical for a MW-like galaxy. Additionally, it has a flattened shape of $c/a \sim 0.52$ and a rather flat metallicity gradient along the minor axis. Moreover, based on the robust correlation established by Harmsen et al. (2017) between the observed stellar mass of the halo and its metallicity at 30 kpc, we have gained valuable insights into the properties of the most significant satellite that was accreted by its host. In this context, Bell et al. (2017) estimated the most significant satellite's mass based on the stellar halo mass, suggesting that for NGC 4945, the mass of its dominant satellite contributor would be approximately $\sim 1.5 \times 10^9$ M$_\odot$, similar to the stellar mass of the LMC. In this work, we prove that NGC 4945 halo has a counter-rotation of $\sim -44 \pm 12$ km s$^{-1}$ at 34.6 kpc along the major axis, which demonstrates its accreted origin.

In order to visualize all the results, in Figure 4.8, we present the velocity measurements obtained in the outer disk and halo fields, located at projected distances of 12 and 35 kpc from the center of the galaxy, respectively. These measurements are shown in comparison to the systemic velocity of NGC 4945, indicated by the horizontal line. We also mark the velocities of the three candidate stars that may belong to NGC 4945.

Importantly, it is worth noting that the kinematic information of these two fields in NGC 4945 is crucial to drawing the conclusion that at $\sim$35 kpc, the accreted component of the stellar halo dominates – but that at $\sim$12 kpc the in situ component still dominates.

### 4.4.2 Three bright candidate member stars found in the halo field of NGC 4945

Individual velocity measurements of stars brighter than the TRGB in the halo field suggest that they belong to the halo of NGC 4945. All three stars have a heliocentric LOS velocity greater than 400 km s$^{-1}$. Of the three stars (listed in Table 4.1), the reddest star (ID=417) falls within the AGB box (see Fig. 2.3). The low number of AGB stars is consistent with the low stellar density of this field and, correspondingly, the low number of RGB stars in this field (Harmsen et al., 2023). Its heliocentric LOS velocity (630$\pm$16 km s$^{-1}$) closely resembles the velocity of the disk of NGC 4945. Besides this AGB star, we also found two stars with bluer colors. These stars closely resemble BHeB and RHeB stars, due to their positions in the CMD (Radburn-Smith et al., 2011), showing evidence of H$\beta$ and HeI lines in their spectra. The presence of helium-burning stars, which have an age between 10-1000 Myr, found at 34.6 kpc from the center of the NGC 4945 is a surprise and cannot be explained by simple radial migration

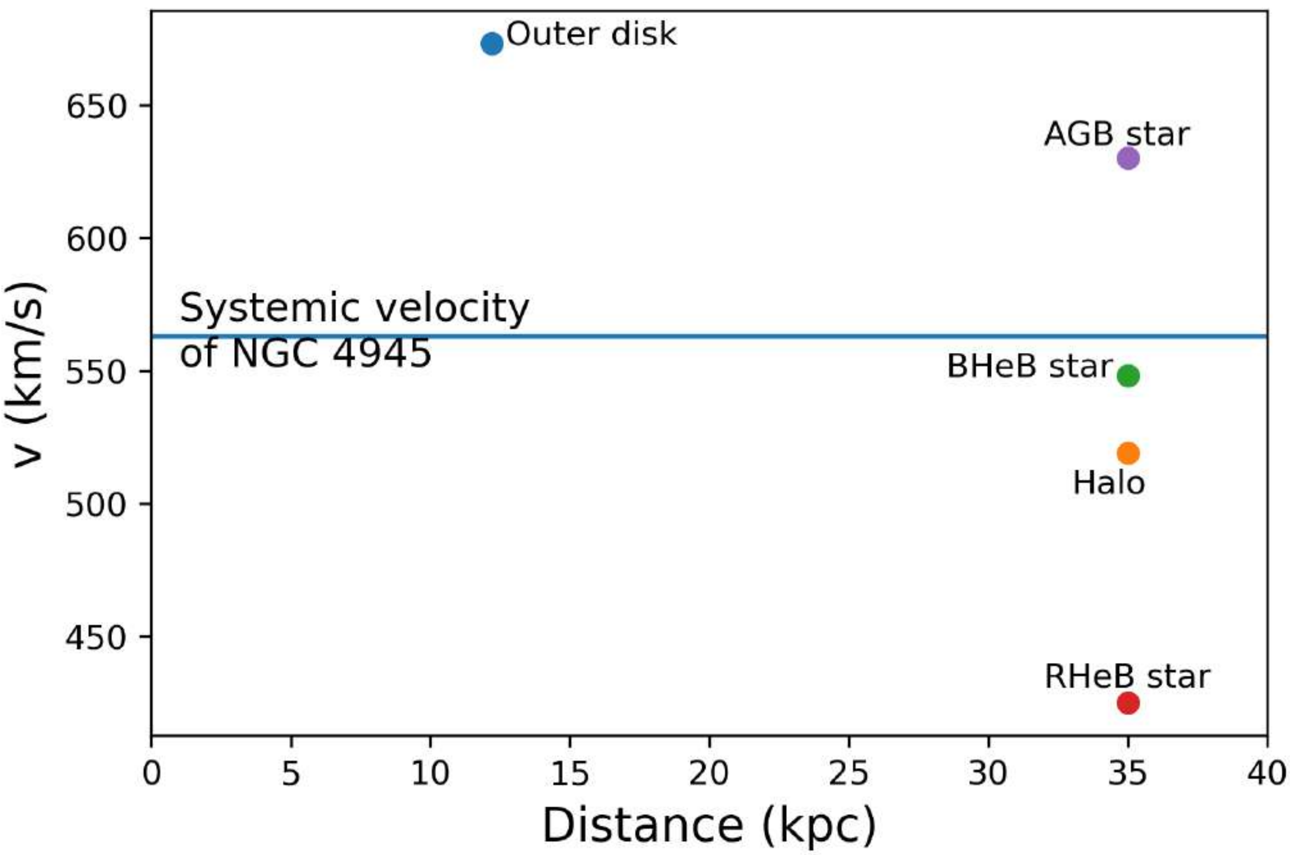


Figure 4.8: Illustrative velocity measurements obtained in the halo field (∼35 kpc) and in the outer disk field (∼12 kpc). In the halo field, we also mark the velocities of the individual stars. The horizontal line is the systemic velocity (563±3 km $s^{-1}$) of NGC 4945 obtained by Koribalski et al. (2004) with HI spectrum.

models of galaxy stellar disks. Their relative lower velocities (548±61 km $s^{-1}$ and 425±27 km $s^{-1}$) are closer to the systemic velocity of NGC 4945 and do not share the dynamics of the disk. Their velocities then suggest that these stars were probably formed in situ in its stellar halo. If so, we should expect to find HI gas in the halo, too. We note that Ianjamasimanana et al. (2022) found HI gas in the halo of NGC 4945, beyond its optical disk; however concentrated mainly on the receding side of the galaxy, not the approaching side where we have our halo field.

We also do not rule out the possibility that these stars are hypervelocity MW dwarf stars, given the low latitude of the observed fields ($b = 13.3°$), which introduces a significant amount of foreground contamination from the MW. As discussed in Sect. 4.1, the probability that these stars are indeed MW foreground is very small ($\approx 0.007$).

### 4.4.3 A comparison with the kinematics of the MW and M31's stellar halos

The kinematic measurements of the stellar halo of NGC 4945 allow us to directly compare with, and to put into context, the two other MW-like galaxies for which we have kinematic data of their stellar halos, namely, the MW and M31. Various surveys have been used to study the halo of the MW, including SDSS (Bell et al., 2008; Deason et al., 2011b), APOGEE (Mackereth & Bovy, 2020), H3 survey (Conroy et al., 2019) and *Gaia* (Gaia Collaboration et al., 2016, 2018, 2021), among others. *Gaia*, in particular, has been revolutionary in providing us with precise photometry, positions, velocities, distances, and proper motions for more than 1 billion sources. Deason et al. (2017) using a combination of SDSS imaging and *Gaia* DR1 astrometry measured a small average rotation of ∼15 km $s^{-1}$ in the stellar halo. The radial velocity dispersion profile decreases from 141 km $s^{-1}$ to 100 km $s^{-1}$ (in the inner 20 kpc) and then remains almost constant out to a distance of ∼70 kpc (Bland-Hawthorn & Gerhard, 2016). Thanks to *Gaia*, the detection of Gaia-Enceladus, the fossil of a major progenitor that was accreted 8-10 Gyr, was made possible (Helmi et al., 2018; Belokurov et al., 2018). These results and the fact that the MW has a small to average stellar halo ($10^9$ $M_\odot$, Deason et al., 2019) brings to light that the accretion history of the Galaxy has been rather quiet for the past gigayears compared to similar sized galaxies.

On the other hand, the proximity of M31 provides a unique opportunity to obtain detailed observations of its entire stellar halo, although with less detailed phase-space information than for the MW. The surveys PAndAS (Ibata et al., 2014; McConnachie et al., 2018) and SPLASH (Gilbert et al., 2012, 2018) have been dedicated to mapping M31's stellar halo using resolved stars. These reveal a massive ($1.5 \pm 0.5 \times 10^{10}$ $M_\odot$, Ibata et al., 2014) and metal-rich (-0.5 dex, Gilbert et al., 2014) stellar halo, with a steep metallicity gradient (Gilbert et al., 2014; Escala et al., 2020, 2021), reflecting the existence of a more massive and recent accretion event, accreted ∼2 Gyr ago, with remnants that are observable in its giant stellar stream (D'Souza & Bell, 2018; Hammer et al., 2018). M31's inner stellar halo shows significant rotation of ∼150 km $s^{-1}$ out to galactocentric distances of $40-70$ kpc along the major axis (Ibata et al., 2005; Dey et al., 2023). Additionally, the velocity dispersion of its stellar halo decreases from 108 km $s^{-1}$ to $\sim 80-90$ km $s^{-1}$ at a projected distance of $\sim 40-130$ kpc from the center (Gilbert et al., 2018).

In this work, we are adding a third galaxy for which we have a kinematic analysis of its stellar halo with resolved stars. We find that the flattened stellar halo (with projected $c/a = 0.52$) of NGC 4945 is accreted at galactocentric distance of 34.6 kpc, and has a counter-rotational velocity of $\sim -40 \pm 12$ km $s^{-1}$. Our measurements also reveal a velocity dispersion of $42 \pm 22$ km $s^{-1}$, lower than the typical halo values of ∼100 km $s^{-1}$. As mentioned before, this velocity dispersion could stem from our measurement capturing a segment of a cold halo component.

### 4.4.4 Limitations of the technique used to derive our measurements

This is the first measurement of the velocity of a diffuse stellar halo of a galaxy outside the Local Group using resolved stars, at a field with a surface brightness of $\sim$29.5 mag/arcsec$^2$, much fainter than the 27 mag/arcsec$^2$ reached by Toloba et al. (2016a). This offers us a taste of what will be routinely possible with the next-generation Extremely Large Telescope (ELT). However, a number of challenges need to be overcome. First, our ability to measure a LOS velocity depends on the S/N of the final stack, which in turn depends upon the number of RGB/AGB stars available to be co-added. In low surface brightness regions (fainter than 28 mag/arcsec$^2$), this becomes extremely challenging. Furthermore, at low Galactic latitudes, one also has to contend with bright MW foreground contamination which further decreases the number of available RGB stars for co-adding. In this work, MW foreground contamination decreases the available number of RGB stars to only 53 in the halo field, resulting in a S/N of 9.4. Note, however, that according to our tests, this is sufficient to obtain reliable LOS velocity and velocity dispersion measurements using pPXF (see Section 3.5.3).

Secondly, it is very difficult to extract the spectra of stars at very low S/N ($<$1), especially for stars that are much fainter than the sky background. In this work, we applied a technique akin to forced PSF photometry. Furthermore, very careful background subtraction is necessary to prevent contamination in the obtained spectra, whether from nearby stars, unresolved sources, or the sky background itself. We measured the variation of the sky background across the halo FoV, particularly focusing on the wavelength region between 8400 to 9350 Å, as this is where the greatest differences in spectra are observed. In this region, we found a minimal variation of 55%, and values reaching up to 130%. Thus, there is a large sky background variation along the FoV, in that wavelength range. In the bluer wavelength range (4800-6800 Å), the sky background variations are similar, ranging from 33% to 180%. If we subtract a general sky background to the extracted spectra of the stars (instead of creating a local background spectrum around each star and subsequently subtracted it from the star's spectrum; see Section 3.5), we obtain S/N values of around 7 for the combined stack spectrum. Despite the spectra being noisier, we still obtained stable velocity values, ranging from 515 to 526 km s$^{-1}$, similar to those shown in Table 4.2. This indicates that even with a general background, reliable velocity values can be obtained. This confirms our test results from Fig. 3.15, which shows that the velocity values can be trusted even at S/N values as low as 4. Nevertheless, in order to achieve spectra with minimal noise and improve the background subtraction, we created a local background spectrum around each star in the halo field and subsequently subtracted it from the star's spectrum.

On the other hand, in the outer disk field, creating a local background spectrum around each star was impractical due to the crowding. Instead we adopted a global background, dividing the FoV into four quadrants, each having a mean background spectrum constructed and subtracted from the spectrum extracted for each individual star. While this approach proved adequate for our purposes and give stable velocity measurements, it certainly can be improved by employing smooth 2D splines to fit the background sky spectrum.

# Chapter 5

# Deciphering the counter-rotating halo of NGC 4945 with simulations

In this Chapter, we compare our results with hydrodynamical cosmological simulations to explore the kinematics of stellar halos in MW-type galaxies within the ΛCDM cosmological framework. Our aim is to gain insights into what the kinematical properties can reveal about the origins of stellar halos. Specifically, we utilize two sets of simulations: Auriga (Grand et al., 2017) and Illustris TNG50 (Pillepich et al., 2019; Nelson et al., 2019).

We contextualize our measured values of LOS velocity and the upper limit of the velocity dispersion for NGC 4945, which are $519 \pm 12$ and $42 \pm 22$ km $s^{-1}$, respectively. This comparison demonstrates that the simulations can produce counter-rotating stellar halos with low velocity dispersion along the line of sight.

Next, we select galaxies from the simulations whose kinematical properties most closely resemble those of NGC 4945, i.e., with counter-rotation and low velocity dispersion. This selection provides insights into the possible accretion history of NGC 4945's stellar halo.

## 5.1 Auriga Simulations

The Auriga project is a set of more than 40 cosmological magneto-hydrodynamical zoom-in simulations of isolated MW-like galaxies. These galaxies were chosen based on their dark matter halos selected from the EAGLE project (Schaye et al., 2015) and fall within the dark matter mass range of $1 \leq M_{200}/10^{12}\ M_{\odot} \leq 2$, comparable to the mass of the MW. These selected dark halos were resimulated with the AREPO code (Springel, 2010) at higher resolution. In this work, we use 28 galaxies of resolution level named Level 4 in Grand et al. (2017), namely, with a baryonic mass resolution of $\sim 5 \times 10^4\ M_{\odot}$ and a dark matter mass resolution of $\sim 3 \times 10^5\ M_{\odot}$. The gravitational softening lengths are 369 pc for star particles and high-resolution dark matter particles. The simulated galaxies lie in the stellar mass range between 2.75 and 10.97 $\times 10^{10}\ M_{\odot}$. They are also star-forming at z=0 and exhibit a typical late-type disk galaxy component, although three of them lack an extended disk, showing a more spheroidal morphology. These simulated galaxies follow the general observational trends for MW-like galaxies, and display a wide variety of properties, primarily due to the diversity in their merger histories (Grand et al., 2017). The Auriga simulations have been extensively used in recent years because they have demonstrated the ability of the galaxy formation model to replicate late-type galaxies with debris from merging activities (for example in reproducing a Gaia-Enceladus-like stream or linking the brightest stream to properties of satellites progenitors, Fattahi et al., 2019; Vera-Casanova et al., 2022). These simulations have also been analyzed to study the properties of the stellar halos of galaxies, revealing diversity in their masses, density profiles, metallicities, shapes, and ages, reflecting the stochasticity in their accretion and merger histories (Monachesi et al., 2016a, 2019). These properties have been compared to nearby MW-like galaxies, primarily from the GHOSTS survey (Monachesi et al., 2016b; Harmsen et al., 2017), and have been found to be in good agreement with observations. We then use this set of simulations, capable of reproducing many observable properties of MW-like galaxies, to analyze their kinematics at distances representing the outer disk and the halo fields of NGC 4945.

## 5.2 TNG50 Simulations

The TNG simulations are another set of cosmological magneto-hydrodynamic simulations depicting the formation and evolution of galaxies. These simulations were run with three different physical box sizes, corresponding to cube volumes of approximately 50, 100, and 300 Mpc side lengths, referred to as TNG50, TNG100, and TNG300, respectively. The resolution increases with decreasing volume, with TNG50 (Nelson et al., 2019; Pillepich et al., 2019) achieving a baryonic mass resolution of $8.5 \times 10^4$ $M_\odot$. The gravitational softening lengths are 290 pc at z = 0 for the stars and dark matter. In this study, we specifically utilize MW and M31 analogs from TNG50 (Pillepich et al., 2023). These analogs represent simulated galaxies with a stellar mass range between $10^{10.5}$ and $10^{11.2}$ $M_\odot$, exhibiting a disk-like morphology and visually identified spiral arms. Additionally, selected analogs meet specific criteria, including having no other galaxies within 500 kpc with a stellar mass greater than $10^{10.5}$ $M_\odot$ and a total mass of the host halo smaller than that typical of massive groups ($\leq 10^{13}$ $M_\odot$). These criteria yield a sample of 180 MW and M31 analogs for our analysis.

## 5.3 Kinematical measurements of the simulated galaxies

To fairly compare the kinematics of simulated galaxies with our observations of NGC 4945, we first addressed the differences in disk sizes among the simulations. To standardize our analysis, we normalized the spatial scales using the optical radius ($R_{\rm opt}$) of each galaxy, defined as the radius where the B-band surface brightness drops down to $\mu_B = 25$ mag arcsec$^2$, even though the extent to which stellar halos scale with $R_{\rm opt}$ remains uncertain. For NGC 4945, the $R_{\rm opt}$ is approximately 12 kpc, placing our MUSE outer disk field at a distance of $\sim 1.02 \times R_{\rm opt}$ and the halo field at $\sim 2.9 \times R_{\rm opt}$ along the major axis. To replicate the positions of these observational fields within the simulations, we rotated each galaxy to align its disk edge-on. We then defined two spatial regions along the major axis: one for the outer disk and another for the stellar halo. Stellar particles were selected from these regions as follows: for the outer disk field, particles were taken from 0.95 to 1.1 $R_{\rm opt}$ and confined within 1 kpc above and below the disk plane. For the halo field, particles were selected from 2.8 to 3.2 $R_{\rm opt}$, with a larger vertical range of 2 kpc. By tailoring these selection criteria, we aimed to closely mimic the spatial configuration of our observational fields while accounting for the intrinsic properties and scale variations of the simulated galaxies. This setup allowed us to directly compare the kinematics of NGC 4945 with those of MW-like galaxies in the

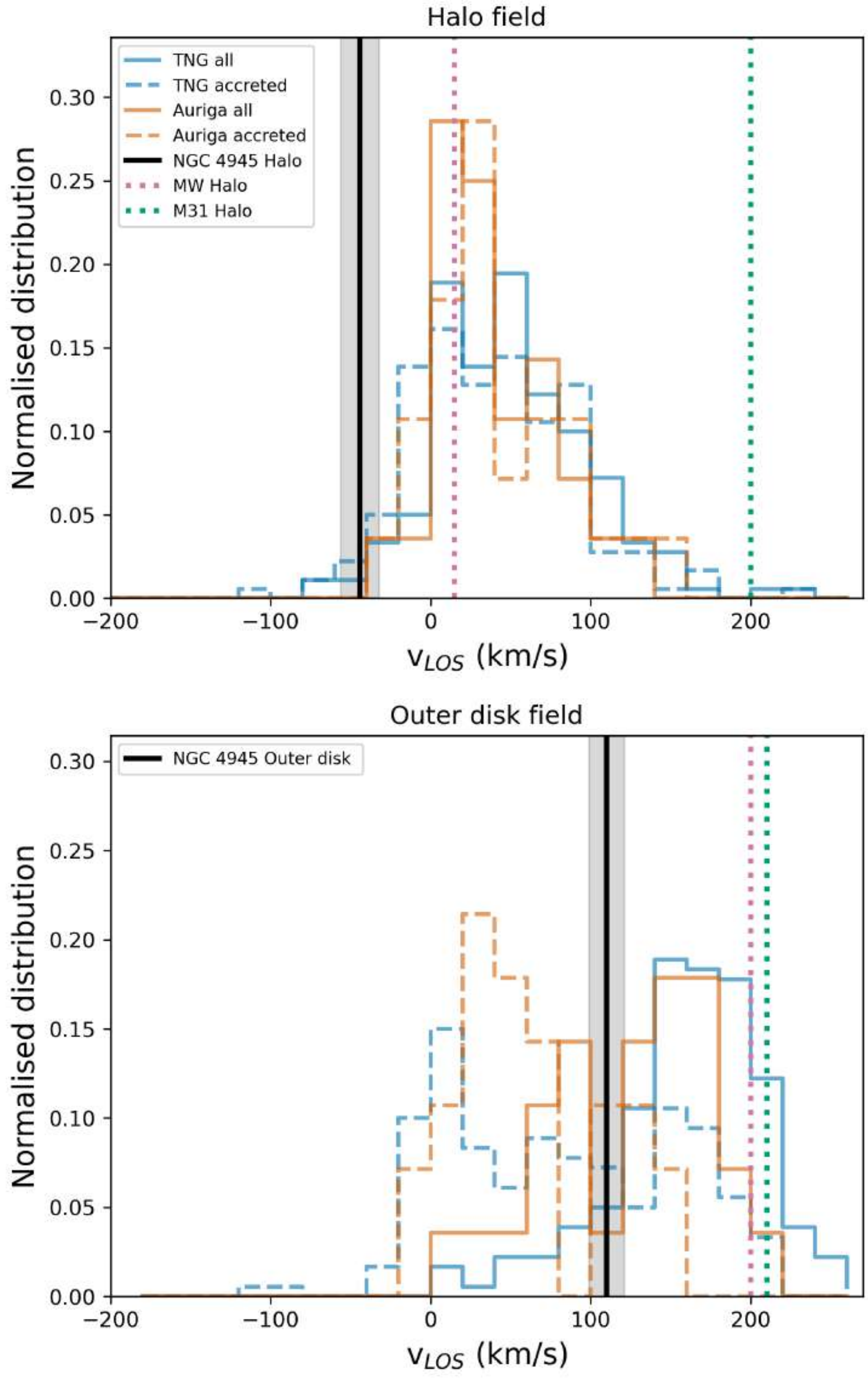


Figure 5.1: Median LOS velocity distribution at galactocentric distances of 1.02$R_{opt}$ (top) and 2.9$R_{opt}$ (bottom) kpc along the major axis for MW/M31 like galaxies in an edge-on configuration, in the TNG50 (blue) and Auriga (orange) simulations. Black vertical lines are our velocity measurements for NGC 4945 at those distances, corrected for its systemic velocity. Green and pink dotted vertical lines show the halo rotational velocity of the MW (halo and outer disk, Deason et al., 2017; Bland-Hawthorn & Gerhard, 2016, respectively) and M31 (halo and outer disk, Ibata et al., 2005; Zhang et al., 2024, respectively).

simulations.

While our MUSE observations are limited to one side of NGC 4945's disk, the selection in the simulations included particles from both sides of the major axis. This approach ensured a more statistically robust sample for kinematic measurements, particularly given the lower stellar density in the halo. Additionally, the larger selection box for the halo field was designed to compensate for the diffuse stellar distribution and to gather sufficient particles for meaningful velocity and velocity dispersion calculations.

For both the Auriga and TNG50 simulations, we calculate the median LOS velocities for all stellar particles and for only the accreted particles within each selection region of every galaxy. The top (bottom) panel of Fig. 5.1 shows the LOS velocity distribution of the box representing the halo (outer disk) region on the major axis, considering all the stellar particles (solid lines) and just the accreted ones (dashed lines), in orange for the Auriga galaxies and blue for TNG50. We also mark with a black vertical line the LOS velocity, corrected for the systemic velocity of NGC 4945, of $-44(110)$ km s$^{-1}$ obtained in this work for the halo(outer disk) of NGC 4945. The grey area around the black lines represents the uncertainty in our measurement. We mark in green and pink the rotational halo and outer disk velocity of the MW and M31 at the corresponding distances of $1.02R_{\text{opt}}$ and $2.9R_{\text{opt}}$. For the MW the $R_{\text{opt}}$ is 12 kpc (Pilyugin et al., 2023) and for M31, it is 21.6 kpc (transformed from an optical radius of 95.3'; de Vaucouleurs et al., 1991). We marked the values at the corresponding $\sim$1.02$R_{\text{opt}}$ and $\sim$2.9$R_{\text{opt}}$ of both galaxies: 200 and 15 km s$^{-1}$ for the MW (Bland-Hawthorn & Gerhard, 2016; Deason et al., 2017) and 210 and 200 for M31 (Zhang et al., 2024).

The median LOS velocities of the Auriga galaxies in the halo selected box (top panel of Fig. 5.1) are distributed between $-40$ and $\sim$160 km s$^{-1}$, with a dominant peak at $\sim$20 km s$^{-1}$. We found no big differences between the total and accreted component distribution, which reflects that at those distances the Auriga simulations predict mostly an accreted component. For TNG50, the bulk of the total median LOS velocity distribution is around $\sim$30 km s$^{-1}$, and there is, like in Auriga, no significant difference between the total and accreted component distribution. However, their values are more widely distributed than in Auriga, between $\sim -100$ and 240 km s$^{-1}$.

Our measured halo LOS velocity of NGC 4945 at $\sim$35 kpc (corrected for the systemic velocity) along the major axis falls within the simulated values, in line with the kinematics of an accreted component of the stellar halo at that distance. The counter-rotation in our MUSE halo field indicates that at this distance of $\sim$35 kpc from the center of NGC 4945 the in situ component is not dominant, assuming that this component should rotate with disk-like kinematics[1].

For the box representing the outer disk field (bottom panel of Fig. 5.1), both the Auriga and TNG50 galaxy samples show a peak in the LOS velocity distribution at around 150 km s$^{-1}$ when considering all particles. This clearly indicates the presence of a rotating disk at those distances. We highlight that, since NGC 4945 is edge-on, its LOS velocity in the outer disk field along the major axis can be regarded as a proxy of its rotational velocity. We also show that a significant number of galaxies from both the TNG and Auriga simulations showcase elevated LOS velocities when solely considering the accreted particles. At this distance, the in situ component is expected to dominate, so this feature can be attributed to a massive satellite that perturbed the disk in such a way that now the satellite and the disks are all aligned and rotating similarly (Gómez et al., 2017).

Our measured LOS velocity for NGC 4945 at $\sim$12.2 kpc along its major axis is 673 km s$^{-1}$. After being corrected by its systemic velocity, we obtained value of 110 km s$^{-1}$, which is a good proxy of the

[1]Although we note that in few of the TNG galaxies some of the in situ populations at $\sim$35 kpc have no rotation.

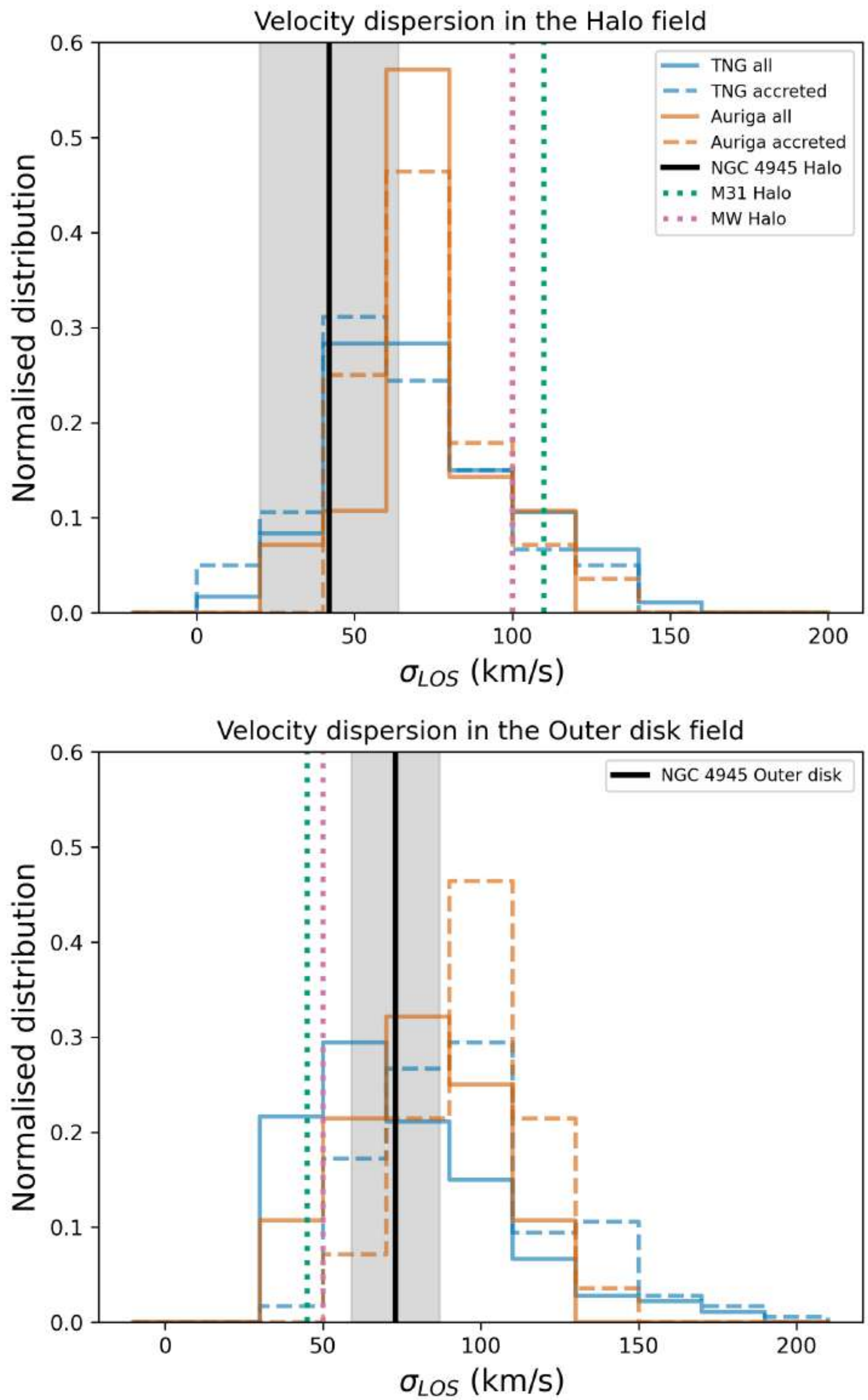


Figure 5.2: Velocity dispersion in the LOS at galactocentric distances of $1.02R_{\rm opt}$ (top) and $2.9R_{\rm opt}$ (bottom) kpc along the major axis for MW/M31-like galaxies in the TNG50 (blue) and Auriga (orange) simulations. Black vertical lines are our velocity dispersion measurements for NGC 4945 at those distances. Green and pink dotted vertical lines show the halo velocity dispersion of the MW (Bland-Hawthorn & Gerhard, 2016) and M31 (Zhang et al., 2024). Our measurements of NGC 4945 are in agreement with both set of cosmological simulations.

rotational velocity of the galaxy, given its edge-on configuration. This value falls within the distribution of LOS velocities obtained from the simulations. Although our measured velocity of 673 km s$^{-1}$ is slightly lower than the one measured in the disk using HI gas in a nearby position, this could be due to a potential contribution from the accreted halo component at this distance. We measured that the accreted halo component, at ∼35 kpc along the major axis, has a velocity of 519 km s$^{-1}$, a bit lower but approximately consistent with the systemic velocity of the galaxy. This component might also be present at 12 kpc in the outer disk field, although it would be much less dominant compared to the in situ component, thereby influencing slightly the obtained LOS velocity. Regardless, we conclude that the in situ component is dominating at this distance.

In Fig. 5.2, we illustrate the distribution of velocity dispersion in the same regions, along with the halo and outer disk, used for the LOS velocity measurements in both Auriga and TNG simulations (Fig. 5.1). Additionally, our velocity dispersion measurements for the halo and outer disk fields (42±22 km s$^{-1}$ and 73±14 km s$^{-1}$, respectively) are indicated by black vertical lines. Furthermore, we include the velocity dispersion values for the MW (50 and 100 km s$^{-1}$ for the outer disk and halo, respectively; Bland-Hawthorn & Gerhard, 2016) and for M31 (∼45 and ∼110 km s$^{-1}$ for the outer disk and halo, respectively; Zhang et al., 2024).

At a distance of $\sim 2.9{\times}R_{\rm opt}$ kpc, both simulations exhibit a peak around ∼70 km s$^{-1}$ in velocity dispersion, with values ranging from 0 to 140 km s$^{-1}$ for the Auriga simulations and 0 to 160 km s$^{-1}$ for the TNG simulations. Our measured LOS velocity dispersion of 42±22 km s$^{-1}$ is lower compared to the MW and M31 halo velocity dispersions. However, it falls well within the range represented by the cosmological simulations, albeit in the lower tail of values. Even considering the uncertainty, our measurement falls within the range of velocity dispersion values depicted by the simulations. This value also supports our scenario of an accreted halo, with a low counter-rotation, and this lower velocity dispersion may indicate that we are capturing some colder halo structure.

At a distance of $\sim 1.02{\times}R_{\rm opt}$ kpc, the peak velocity dispersion ranges between 50 and 80 km s$^{-1}$ in both sets of simulations, with values ranging from 30 to 200 km s$^{-1}$ in the TNG simulations and between 30 and 150 km s$^{-1}$ in the Auriga simulations. Our measured velocity dispersion in the outer disk field is 73±14 km s$^{-1}$, falling squarely within the range exhibited by the simulations. It is important to note that the velocity dispersion observed in this field exceeds that of the halo and exceeds what is typically expected in a disk. The positioning of the outer disk field (particularly with one end closer to the disk, where we observe a drastic increase in stellar density in that corner) may account for this higher velocity dispersion. We attribute this elevated dispersion to a combination of contributions from both ordered motion in the disk and stars with kinematics more akin to the halo, resulting in an overall increase in velocity dispersion.

Additionally, for comparison, we selected the stellar particles in boxes at fixed distances of 12.2 kpc and 35 kpc, instead of using the optical radius of the galaxies, which mimics the physical locations of our MUSE fields. The results from these selection boxes are shown in Figure 5.3 and Figure 5.4. At ∼35 kpc, both sets of simulations do not show significant differences compared to the results obtained by normalizing the distance to $2.9R_{\rm opt}$. Similarly, there are no significant differences when we fix the boxes at 12.2 kpc, compared to the results using a normalized distance of $1.02R_{\rm opt}$.

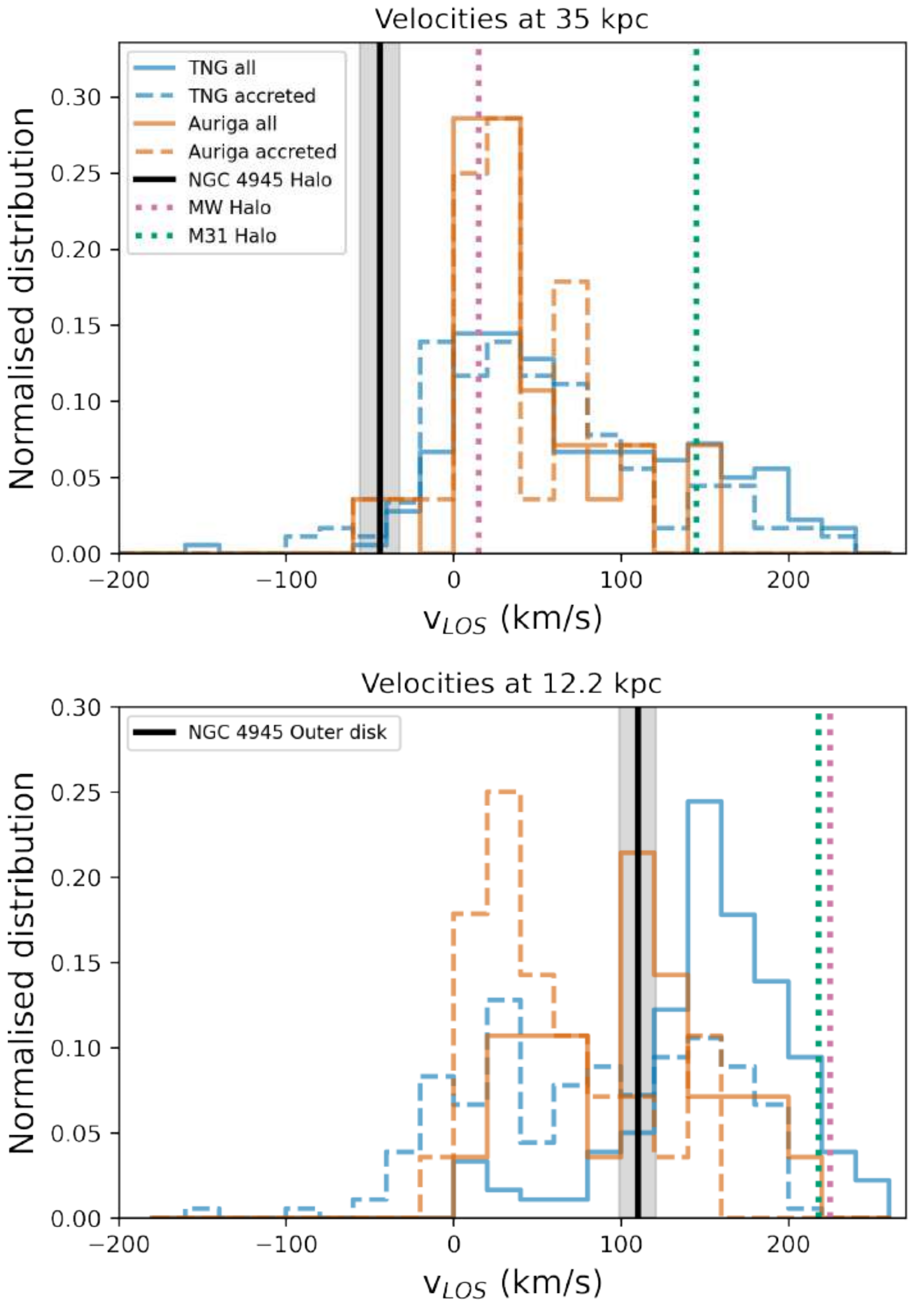


Figure 5.3: Median LOS velocity distribution at galactocentric distances of 35 (Upper) and 12.2 (bottom) kpc along the major axis for MW/M31-like galaxies in an edge-on configuration, in the TNG50 (blue) and Auriga (orange) simulations. Black vertical lines are our velocity measurements for NGC 4945 at those distances, corrected for its systemic velocity. Green and pink dotted vertical lines show the halo rotational velocity of the MW (halo and outer disk, Deason et al., 2017; Bland-Hawthorn & Gerhard, 2016, respectively) and M31 (halo and outer disk, Ibata et al., 2005; Zhang et al., 2024, respectively). Our velocity measurements of the stellar halo of NGC 4945 at 35 kpc are in agreement with those of the accreted component of the simulated galaxies at 35 kpc. At a distance of 12.2 kpc, simulations show that our results are consistent with the disk in situ component dominating the field, with little contribution from the accreted component.

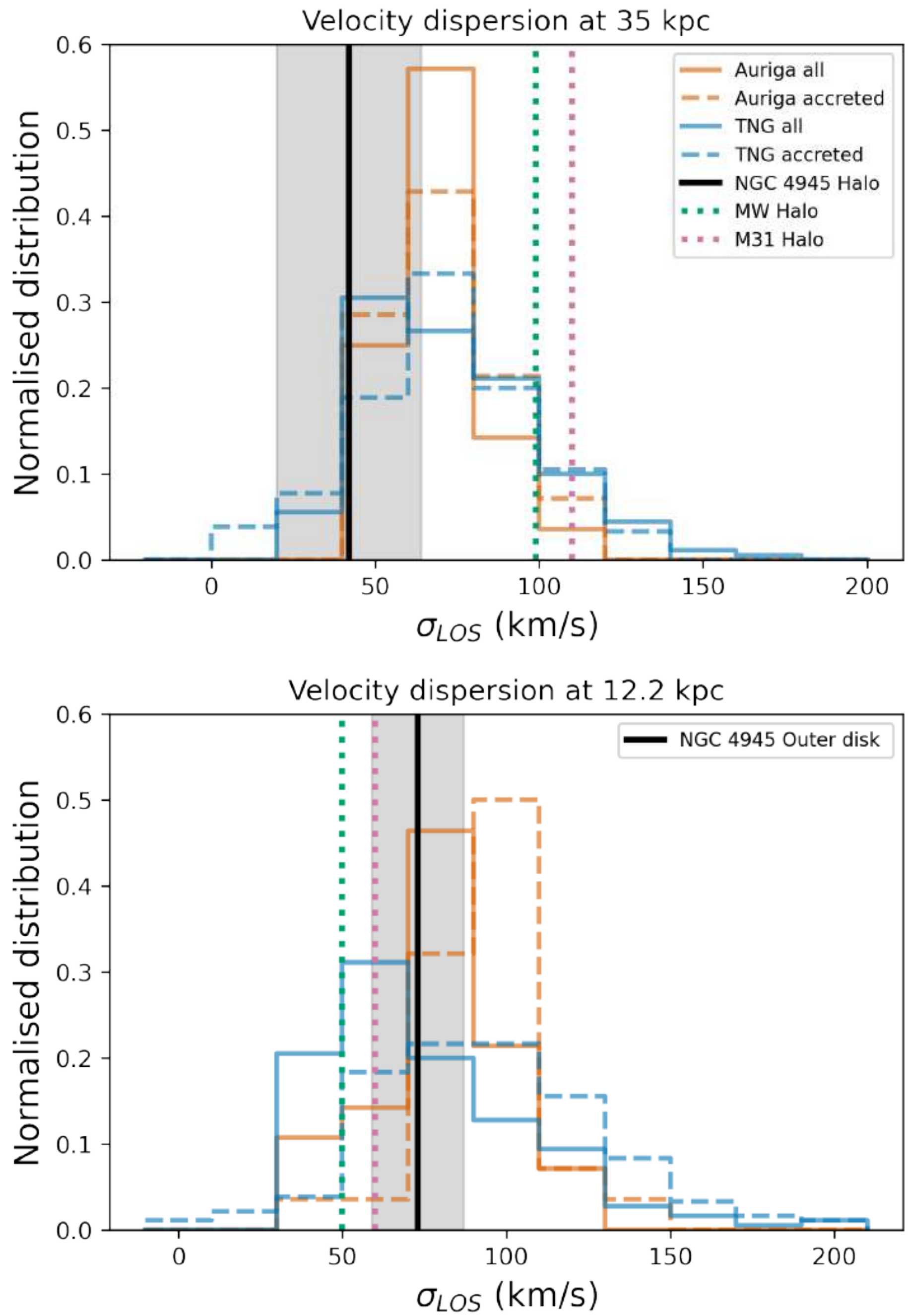


Figure 5.4: Velocity dispersion in the LOS at galactocentric distances of ∼35 (top) and 12.2 (bottom) kpc along the major axis for MW/M31-like galaxies in the TNG50 (blue) and Auriga (orange) simulations. Black vertical lines are our velocity dispersion measurements for NGC 4945 at those distances. Green and pink dotted vertical lines show the halo velocity dispersion of the MW (Bland-Hawthorn & Gerhard, 2016) and M31 (Zhang et al., 2024). Our measurements of NGC 4945 are in agreement with both sets of cosmological simulations.

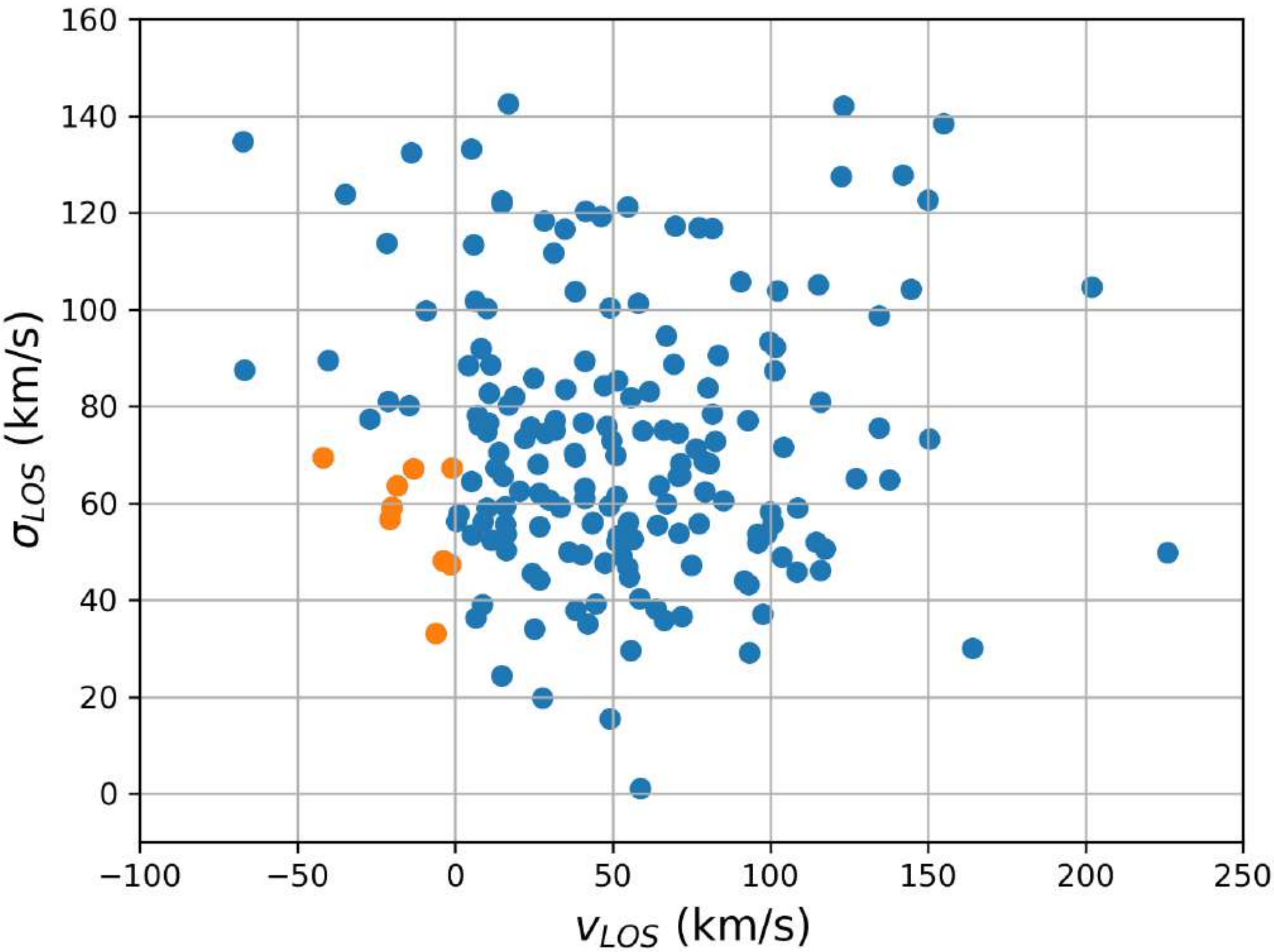


Figure 5.5: Line of sight velocity vs. velocity dispersion measurements at distances of $2.9\times R_{\rm opt}$ kpc along the major axis for the entire TNG50 sample of MW/M31-like galaxies. Orange dots indicate the sample that meet our kinematic criteria of counter rotation and low velocity dispersion.

## 5.4 Identifying NGC 4945 Analogs in Simulations

As we demonstrated in the previous section, the kinematic properties of NGC 4945's stellar halo make it a particularly intriguing case for study. At a galactocentric distance of $\sim 2.9\times R_{\rm opt}$ ($\sim$ 35 kpc), our measurements revealed a counter-rotating halo with a low velocity dispersion. Such a combination of features is rare among simulated MW-like galaxies, highlighting the uniqueness of NGC 4945 and the potential clues its stellar halo holds about its evolutionary history. To better understand this phenomenon, we aimed to identify galaxies in our simulation sample that share similar kinematic characteristics. These analogs could provide insights into the conditions or events that lead to such distinct halo properties.

Building on the kinematic results from NGC 4945, we selected galaxies with stellar halos that closely resemble their LOS velocity and velocity dispersion. Specifically, we defined the selection criteria as $v_{LOS} < 0\,{\rm km\,s^{-1}}$ and $\sigma_{LOS} < 70\,{\rm km\,s^{-1}}$. Figure 5.5 illustrates the relationship between velocity dispersion

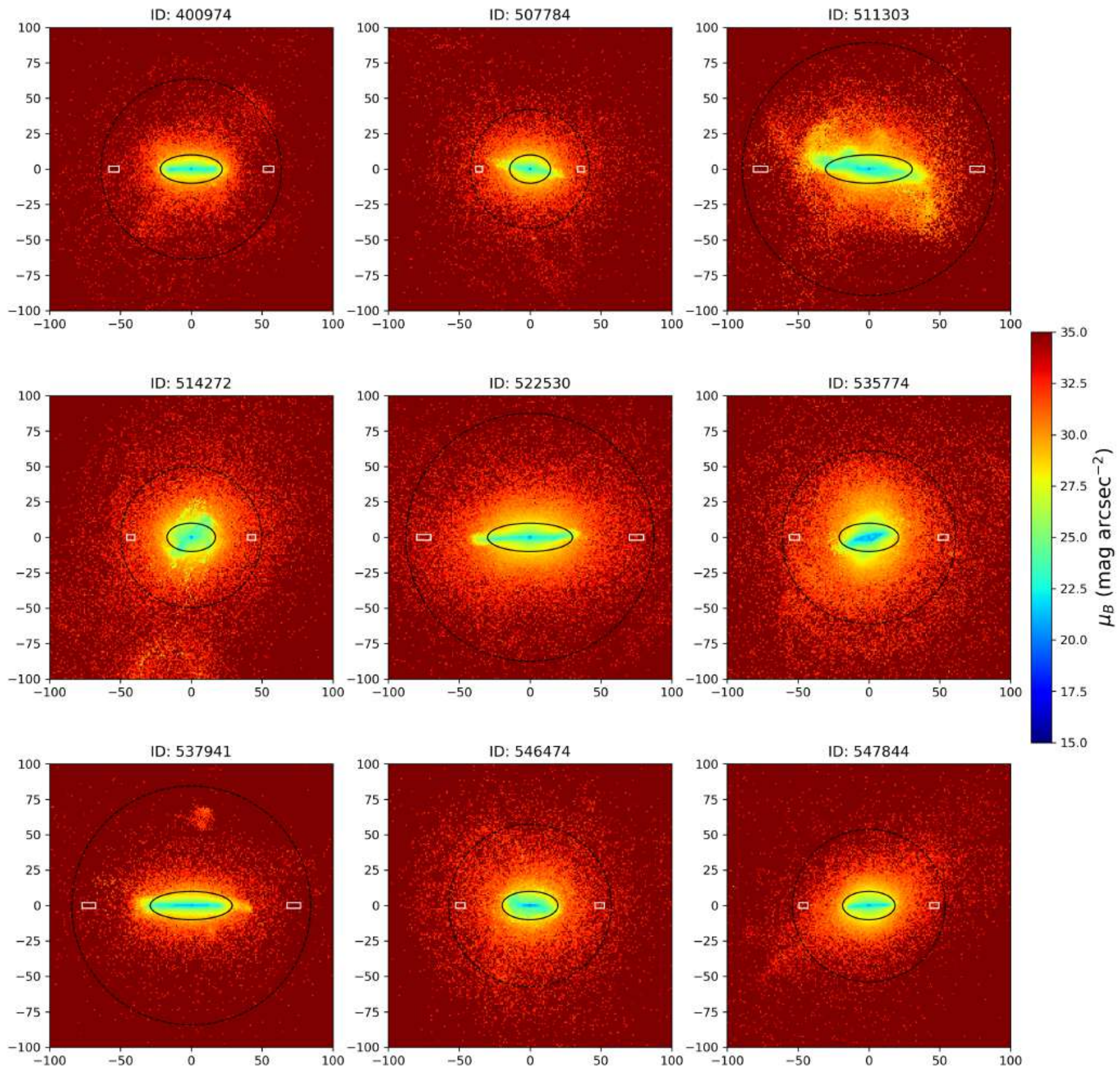


Figure 5.6: Surface brightness maps in the B-band of the TNG50 subsample that meets the same kinematic properties of counter-rotation and low halo velocity dispersion as were found in NGC 4945. The particles inside the inner black ellipse are spatially considered disks. The outer dashed circumference at $3.5\times R_{\rm opt}$ indicates the virtual limit to calculate stellar masses. White boxes indicate our spatial identification of the halo particles to measure LOS velocity and dispersion velocity of the stellar halo in each galaxy.

Table 5.1: Optical radius and stellar mass properties of the nine TNG 50 galaxies similar to NGC 4945 kinematically. Columns three, four and five are the total stellar mass, total halo mass and total accreted halo mass of each galaxy.

| ID | $R_{\rm opt}$ [kpc] | $M_*^{\rm tot}$ [$M_\odot$] | $M_*^{\rm halo}$ [$M_\odot$] | $M_*^{\rm haloacc}$ [$M_\odot$] |
|---|---|---|---|---|
| 400974 | 18.2 | $3.89\times10^{10}$ | $9.56\times10^{8}$ | $1.27\times10^{8}$ |
| 507784 | 12.0 | $3.96\times10^{10}$ | $1.37\times10^{9}$ | $3.60\times10^{8}$ |
| 511303 | 25.5 | $4.97\times10^{10}$ | $3.31\times10^{9}$ | $9.60\times10^{8}$ |
| 514272 | 14.2 | $3.79\times10^{10}$ | $3.00\times10^{9}$ | $1.29\times10^{9}$ |
| 522530 | 25.0 | $6.91\times10^{10}$ | $3.84\times10^{9}$ | $2.60\times10^{9}$ |
| 535774 | 17.5 | $5.14\times10^{10}$ | $4.69\times10^{9}$ | $1.42\times10^{9}$ |
| 537941 | 24.1 | $5.23\times10^{10}$ | $1.20\times10^{9}$ | $1.57\times10^{8}$ |
| 546474 | 16.4 | $4.75\times10^{10}$ | $1.62\times10^{9}$ | $6.32\times10^{8}$ |
| 547844 | 15.4 | $5.10\times10^{10}$ | $1.98\times10^{9}$ | $5.51\times10^{8}$ |

and LOS velocity for the stellar halos of the 180 galaxies analyzed in the TNG50 sample. The galaxies meeting our criteria are highlighted in orange. Remarkably, only nine out of 180 galaxies, i.e. only 5% of the TNG50 sample, matched these conditions, emphasizing the rarity of such kinematic configurations.

To further characterize these analogs, Figure 5.6 shows the surface brightness profiles of the nine galaxies that match the kinematic constraint. In each panel, the inner black ellipse represents a region with a major axis equal to $R_{\rm opt}$ and a minor axis extending to 10 kpc, while the dashed black circle marks a radius of $3.5\times R_{\rm opt}$. The region between the ellipse and the circle is considered as the stellar halo of these galaxies, to mimic what is done in observational works (Harmsen et al., 2017). The white boxes denote the area at $\sim 2.9\times R_{\rm opt}$ corresponding to the position of our MUSE halo field in NGC 4945, where we measured $v_{LOS}$ and $\sigma_{LOS}$. Among these analogs, we observe a striking diversity in morphological properties: for example, galaxy ID 514272 is undergoing a merger, with a visibly distorted disk, while galaxy ID 522530 exhibits a disk extending well beyond $R_{\rm opt}$.

In addition to the kinematic information obtained for the stellar halo of NGC 4945, we know that its stellar halo mass is $1.69\times10^{9}$ $M_\odot$ (between 10 to 40 kpc Harmsen et al., 2017). Since our kinematic measurements indicate that the stellar halo at $\sim$35 kpc is accreted, we further refine our sample by selecting TNG50 galaxies with a minimum accreted stellar halo mass of $5.00\times10^{8}$ $M_\odot$.

For each galaxy, we calculated: (1) the total stellar mass by summing the mass of all stellar particles; (2) the stellar halo mass, determined by summing the mass of particles within the region between the ellipse and the red circle; and (3) the mass of accreted particles in the stellar halo, using only particles identified as accreted. These properties along with the optical radius of each galaxy are summarized in Table 5.1.

Among the nine pre-selected galaxies, six meet both the kinematic and stellar halo mass criteria. For these six galaxies, we analyzed the origin of the accreted particles within the selection boxes (see Figure 5.6) to identify and characterize the contributing satellites in terms of their mass and accretion time.

To carry out this analysis, we developed a code that traces the progenitor subhalo of each accreted particle in the selection box. For each contributing subhalo, we calculated its maximum stellar mass and determined the time of accretion onto the host galaxy, defined as the last snapshot in which the satellite was identified. The subhalo that contributed the most particles to our selection boxes is referred to as the dominant satellite.

The analysis of the six selected galaxies, identified as analogs to NGC 4945, yielded the following results:

1. Two galaxies (522530 and 535774) have a single dominant satellite that contributed the majority of the accreted particles. Their maximum stellar masses of 6.45 and 2.62 $\times 10^9$ $M_\odot$, accreted approximately 6 Gyr ago.

2. One galaxy (546474) exhibits contributions from two dominant satellites, with maximum masses of 3.7 $\times 10^9$ $M_\odot$ and 1.2 $\times 10^8$ $M_\odot$, accreted 7.6 Gyr and 5.5 Gyr ago, respectively.

3. One galaxy (514272) has contributions from three dominant satellites, with maximum stellar masses of 1.2 $\times 10^9$ $M_\odot$, 9.9 $\times 10^8$ $M_\odot$, and 4.2 $\times 10^9 M_\odot$, accreted 9.1 Gyr, 8.5 Gyr, and 7.2 Gyr ago, respectively.

4. One galaxy (511303) shows that 50% of the accreted particles originated from a single satellite with a maximum mass of 3.7 $\times 10^8$ $M_\odot$, accreted 6.3 Gyr ago.

5. The galaxy (547844) shows contributions from several satellites, with the most massive contributing 5.8 $\times 10^8$ $M_\odot$, accreted 8.8 Gyr ago, and the most recently accreted satellite (5.1 Gyr ago) having a maximum mass of 1.3 $\times 10^8$ $M_\odot$.

Our findings suggest that in half of the selected NGC 4945 analogs, the accreted stellar particles primarily originated from one or two dominant satellites, which can account for the observed counter-rotation and low velocity dispersion in those regions.

Through visual inspection, we identified three galaxies that most closely resemble NGC 4945: IDs 522530, 535774, and 546474. To better understand the origin of the observed low velocity dispersion in the stellar halo of these galaxies, we aim to identify potential substructures that may have contributed to this feature. Figures 5.7 and 5.8 display the spatial distribution of all particles within each galaxy (blue dots), with accreted particles inside the selection boxes highlighted in black. For these accreted particles, we identified their progenitor satellite (or two satellites in the case of galaxy 546474) and marked all particles associated with the satellite in orange (and purple).

For galaxy 522530, we observe that accreted particles at distances of approximately x$\sim -75$ kpc align with possible shell structures. At a distance of x$\sim$110 kpc, satellite particles form a clear long stream that extends from $\sim$50 kpc above the plane of the disk to $\sim$110 kpc below it, reaching toward x$=0$.

In galaxy 535774, accreted particles on both sides of the galactic center coincide with an overdensity of the dominant satellite's particles, also visible in the surface brightness map. An additional overdensity is observed $\sim$100 kpc from the disk center and $\sim$50 kpc above the disk plane. However, another overdensity located at $\sim -50$ kpc from the disk and $\sim$50 kpc below the plane appears unrelated to the dominant satellite, suggesting the presence of a separate accreted structure or interaction.

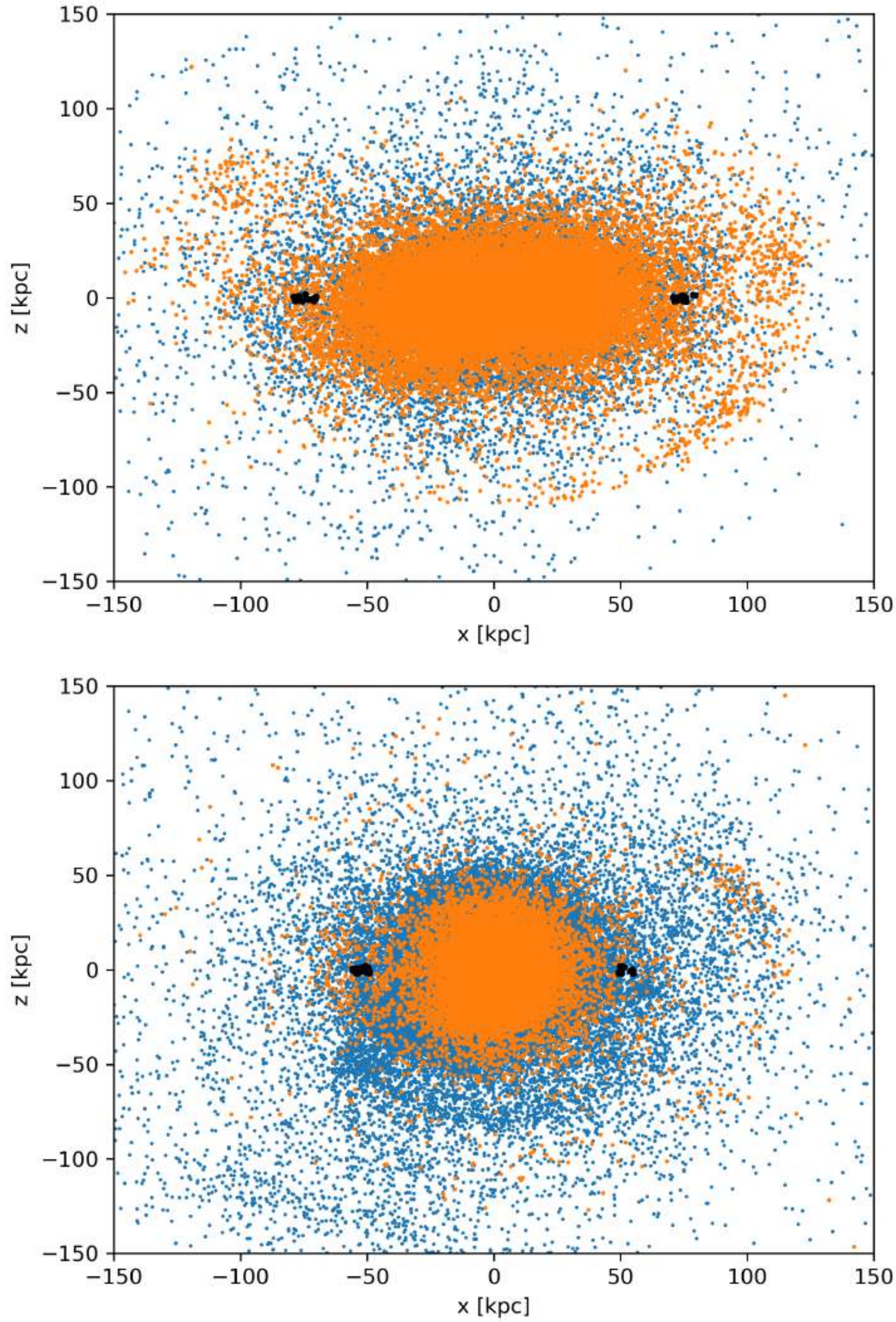


Figure 5.7: Galaxies 522530 (top) and 535774 (bottom). Blue dots are all the particles (in situ and accreted) from the entire galaxy. Orange dots are the particles from the dominant satellite that contributed the majority of the accreted particles to our selection boxes. Black dots are the accreted particles within the selection boxes mimicking our NGC 4945 halo observations.

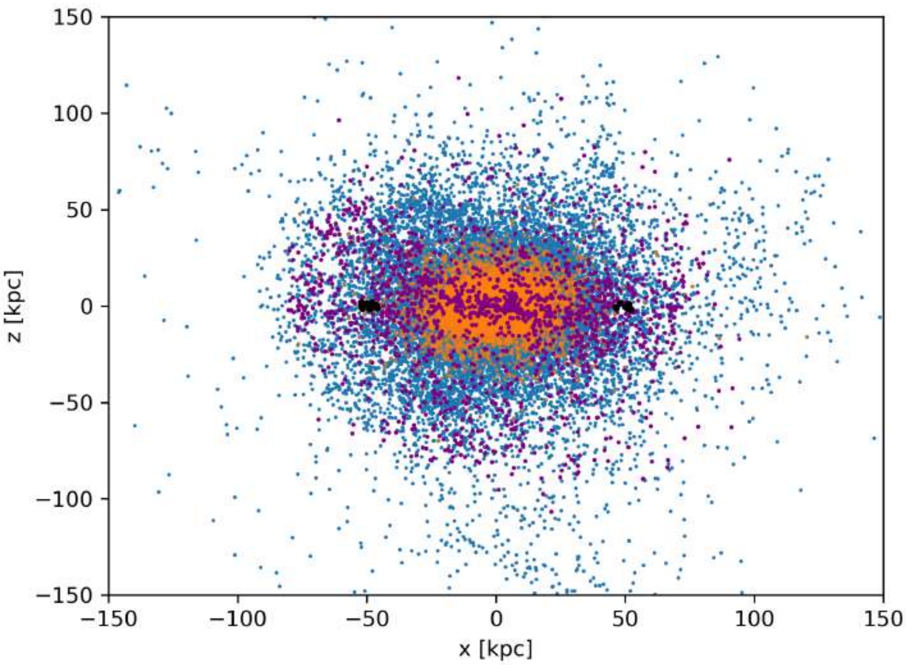


Figure 5.8: Galaxy 546474. Blue dots are all the particles (in situ and accreted) from the entire galaxy. Orange dots are the particles from the most massive satellite contributing to our accreted particles in the selection box. Purple dots represent particles from the second most massive satellite. Black dots are the accreted particles within the selection box mimicking our NGC 4945 halo observations.

Two dominant satellites were identified for galaxy 546474 and visualized using distinct colors for clarity. The most massive and oldest accreted satellite (orange) is concentrated near the galactic center. The second satellite (purple) is primarily distributed along the disk plane, especially in the central region spanning $-30$ to 30 kpc from the disk center. At greater distances ($-30$ kpc), its particles scatter above and below the plane, forming two distinct shell-like substructures at x$\sim -40$ kpc and x$\sim -70$ kpc. Due to their prominence, we selected two regions within these shells for kinematic analysis. Velocity dispersion measurements yielded values of 13 and 33 km $s^{-1}$ for the outer and inner shells, respectively, with LOS velocities of $-12$ and $-15$ km $s^{-1}$. The accreted particles in the selection region that mimics our NGC 4945 observations (black particles in Figure 5.7 and 5.8) exhibit a LOS velocity of $-2.7$ km $s^{-1}$ and a velocity dispersion of 30 km $s^{-1}$, consistent with the shells' measurements.

We also analyzed the particles from the three dominant satellites in galaxy 514272. However, this system is currently undergoing a massive merger, which has even deformed its disk. Explaining counter-rotation and low velocity dispersion, in this case, is challenging due to the combined contributions of multiple satellites and the ongoing merger. This scenario does not align with NGC 4945, as it is not currently experiencing a major merger.

Attempts to perform similar analyses for the other two galaxies were hindered by multiple contributing satellites, making it difficult to isolate overdensities that could account for low velocity dispersion and counter-rotation. However, these cases remain interesting for further investigation.

## 5.5 Discussion

In this chapter, we analyzed the LOS velocity and velocity dispersion distributions of the halo and outer disk fields of NGC 4945, comparing them with predictions from the TNG50 and Auriga cosmological simulations. Additionally, we searched for analogs to NGC 4945 in terms of kinematics and stellar halo accreted mass.

To compare our observations with the TNG50 and Auriga simulations, we selected particles located at distances similar to those covered by our MUSE fields, in terms of $R_{\rm opt}$, as explained in Section 5.3. However, the region used to select stellar halo particles at $2.9R_{\rm opt}$ is significantly larger than the actual MUSE FoV, which may have affected our velocity dispersion measurements. This larger selection region was chosen to compensate for the low number of particles at that distance and to obtain a more statistically robust measurement. With higher-resolution simulations, a more direct and precise comparison will be possible. Nevertheless, the results obtained from TNG50 and Auriga provide an important first step in understanding the counter-rotating and low-velocity dispersion kinematics of NGC 4945's stellar halo at $2.9R_{\rm opt}$.

For both fields, the measured LOS velocity of NGC 4945, corrected for systemic motion, aligns well with the range of velocities predicted by the simulations. However, both measurements lie in a less common region of the distribution, making NGC 4945 an interesting case to analyze, as few galaxies exhibit accreted stellar halos counter-rotating. To investigate further, we selected a subsample of TNG50 galaxies with counter-rotation ($v_{LOS} < 0$ km $s^{-1}$) and velocity dispersion values below 70 km $s^{-1}$. For these galaxies, we analyzed the accreted particles located within the halo region at 2.9 $R_{\rm opt}$ and traced their origins.

The counter-rotation observed in our data implies that the in situ stellar component is not dominant at these radii, further supporting an accretion-driven formation scenario. Specifically, the counter-rotation at a distance of 2.9 $R_{\mathrm{opt}}$ suggests the presence of material deposited during a past merger event. This is corroborated by the low measured velocity dispersion of 42±22 km s$^{-1}$ in the halo field, which falls within the lower range of values predicted by the simulations. Such a low velocity dispersion indicates the presence of a dynamically cold substructure.

It is important to emphasize that, as a MW-like galaxy, NGC 4945 is expected to host a significant population of classical satellites ($M_V < -9$), alongside numerous fainter satellites. However, no satellites have been reported for this galaxy to date. Therefore, explaining the counter-rotation and low velocity dispersion as the result of a satellite depositing its particles at 2.9 $R_{\mathrm{opt}}$ is a plausible scenario. Interestingly, a previous study by Ianjamasimanana et al. (2022), based on HI observations with MeerKAT, identified a well-defined warp on both the approaching and receding sides of the galaxy. The origin of this warp could be linked to a prior interaction with a satellite galaxy, although no direct evidence of such an accretion event has yet been obtained.

To explore this, we selected counter-rotating galaxies from the TNG50 simulation with low velocity dispersion at distances comparable to our MUSE halo field. We analyzed the accreted particles in this region, starting with a visual inspection of surface brightness maps, followed by an analysis of the satellites from which these particles originated and the locations of the remaining particles from those satellites. In half of our sample (three galaxies), the accreted particles at 2.9 $R_{\mathrm{opt}}$ originated from one or two satellites. Furthermore, the remaining particles from these satellites formed overdensities near the selected region. This indicates that the counter-rotation and low velocity dispersion observed in the stellar halo of NGC 4945 at 2.9 $R_{\mathrm{opt}}$ could indeed be explained by streams or shells of an accreted satellite, which left its kinematic imprint on the halo. For the two galaxies where counter-rotation in the stellar halo can be attributed to a single dominant satellite, the satellites were accreted approximately 6.5 Gyr ago, contributing masses of 6.45 and 2.62 $\times 10^9$ $M_\odot$, respectively. The third galaxy showed contributions from two satellites to the counter-rotation, with the second satellite forming shell-like structures in the stellar halo. This satellite was accreted more recently, around 5.5 Gyr ago (compared to the first, accreted 7.6 Gyr ago), and contributed a mass of $\sim 1.2 \times 10^8 M_\odot$−ten times less massive than the earlier accreted satellite.

# Chapter 6

# Summary

Understanding the formation and evolution of galaxies remains one of the most compelling questions in modern astrophysics. The structures and kinematics of their stellar halos hold crucial clues about their assembly history, tracing both the internal processes and external interactions that have shaped them over cosmic time.

In addition to the accreted component, simulations predict the existence of an in situ stellar halo component. This component is composed of stars that were “kicked-up” from the disk, smooth accreted gas, and other elements. However, this in situ component is poorly constrained, with significant variation between models. One potential way to measure it is by identifying stars that were heated and displaced from the disk due to interactions with satellites, resulting in more halo-like orbits. These stars are predicted to be more dominant along the galaxy’s major axis.

Identifying the in situ stellar halo is thus crucial for understanding the formation and structure of the stellar halo. While the outer regions of halos are dominated by accreted material, the inner regions may have a significant contribution from this in situ component, particularly from stars heated during past interactions that now exhibit halo-like orbits. Therefore, kinematic studies of stellar halos are essential to disentangle the contribution of "kicked-up" stars to the stellar halo.

While significant progress has been made in kinematically studying the stellar halos of nearby galaxies, most of these studies have relied on tracers such as PN or GC. Studies of resolved stellar populations have so far been limited to the MW and M31, the two main MW-like galaxies in the LG. Expanding kinematic studies of stellar halos to other galaxies using resolved stellar populations is necessary to avoid the limitations inherent to other tracers and build a larger database for comparison to theory. This thesis presents a robust methodology that paves the way for such studies in galaxies beyond the LG. Furthermore, with the advent of new instruments and the next generation of giant telescopes, it will become possible to extend these studies to more distant galaxies, requiring less integration time.

NGC 4945, a MW-like galaxy located at 3.6 Mpc, serves as an excellent target for this work. Its stellar halo was first detected and studied by Monachesi et al. (2016b) and Harmsen et al. (2017) using GHOSTS HST imaging data. The halo is relatively massive ($M_{halo} \sim 3 \times 10^9$ $M_\odot$), oblate ($c/a = 0.51$ at 25 kpc), and metal-rich ([Fe/H] $\sim -0.9$ dex). This thesis focused on studying the kinematics of the stellar halo of NGC 4945, marking the first time such measurements have been conducted for a stellar halo outside the LG.

To achieve this, we used new MUSE data in combination with HST imaging data across two fields along the galaxy’s semi-major axis: one at a galactocentric distance of $\sim$12.2 kpc to measure the kinematics of the outer disk, and another at $\sim$35 kpc to study the stellar halo. The goal was to disentangle potential contributions from the in situ halo in the outer halo field. Details of the data used in this thesis are provided in Chapter 2.

In Chapter 3, we describe the methodology developed to obtain reliable measurements of radial velocity and velocity dispersion in both fields. This involved obtaining spectra with minimal contamination from other sources and sky residuals. To characterize the kinematics of the stellar halo and outer disk, we performed stacking of spectra from RGB stars (up to 2 magnitudes below the TRGB) in the halo field and RGB plus AGB stars in the outer disk field. This stacking significantly improved the S/N of the final spectrum. We then used the pPXF software to measure LOS velocity and velocity dispersion from the co-added spectra.

Chapter 4 presents the main kinematic results. For the halo field, we co-added 53 RGB stars, reaching a S/N= 9.4 for its stacked spectrum. We measured a mean heliocentric LOS velocity of 519$\pm$12km s$^{-1}$ and a velocity dispersion of 42$\pm$22 km s$^{-1}$. Given NGC 4945 systemic velocity of 563$\pm$3 km s$^{-1}$, this measurement shows that the halo of NGC 4945 at $\sim$35 kpc from its center along the major axis is counter-rotating, with a rotational velocity of $-44 \pm 12$ km s$^{-1}$, which demonstrates its accreted origin, with no contribution from the in situ component. Additionally, we measured velocities for individual stars in the halo field with S/N $> 4$. Most of the stars brighter than the TRGB in the halo field are MW foreground stars, based on their measured velocities. However, we found three stars in the halo field that are brighter than the TRGB, with velocities larger than 400 km s$^{-1}$. These stars are strong candidates to belong to NGC 4945 stellar halo based on their velocities only. According to their position in the CMD, these stars would be one AGB, one BHeB, and one RHeB. For the outer disk field, we co-added 1122 RGB stars along with 70 AGB stars, resulting in a stacked spectrum with S/N= 16.7 and a mean heliocentric LOS velocity of 673$\pm$11 km s$^{-1}$ and a velocity dispersion of 73$\pm$14 km s$^{-1}$. This is consistent with the mean HI velocity of the disk at a nearby position ($\sim$700 km s$^{-1}$, Koribalski et al., 2018). In this Chapter, we also discuss the implications of our kinematic measurements, including the presence of a cold structure in the halo, inferred from the lower velocity dispersion compared to the outer disk.

In Chapter 5, we use the TNG50 and Auriga cosmological simulations to gain insight into the kinematic behavior of NGC 4945's halo and the possible presence of substructure that could explain the observed counter-rotation and low velocity dispersion at $\sim$35 kpc. From a sample of 180 TNG50 galaxies, we identified nine with counter-rotating halos and low velocity dispersion at analogous distances. Of these, six had a stellar halo mass $> 5 \times 10^8$ M$_\odot$. Finally, three of these galaxies showed substructures that could explain the counter-rotation and low velocity dispersion. In these cases, accreted particles in the regions corresponding to the MUSE halo field originated from a satellite with a mass of $\sim 5 \times 10^9$ M$_\odot$, and in one case, a secondary satellite with a mass of $\sim 10^8$ M$_\odot$. This supports the idea that the counter-rotating halo of NGC 4945 at 35 kpc, with its low velocity dispersion, is a cold structure formed from a satellite merger. However, it is important to note that no satellites of NGC 4945 have been detected to date.

The resolved stellar halo velocity measurement of NGC 4945 with MUSE sets a new standard for studying stellar halos in galaxies beyond the LG. The results presented in this thesis highlight the existence of an accreted flattened stellar halo with a slight counter-rotation. Importantly, this work adds a third galaxy with these types of measurements to the only other two galaxies whose diffuse stellar halos have been studied kinematically from their resolved stars: the MW and M31. The methodology and analysis presented here demonstrate the potential for future studies using next-generation telescopes like the ELT. With its 39-meter segmented mirror, the ELT will enable the resolution of individual halo stars in more distant galaxies. The MOSAIC instrument, with its 40-times larger field of view than MUSE and the ability to observe 200 objects simultaneously, will be ideal for mapping stellar halos. Additionally, HARMONI, with its higher spectral resolution and capabilities in both visible and NIR wavelengths, will allow detailed studies of more distant halos with shorter integration times. These instruments will significantly expand the statistical sample of galaxies studied, enabling a deeper understanding of the origin and evolution of stellar halos.

# Chapter 7

# Future work

This thesis opens avenues for further investigation, which we outline in this Chapter. On one hand, we can continue studying the properties of NGC 4945 using the same dataset. On the other hand, we can explore its evolutionary history in greater depth using cosmological simulations.

## 7.1 Observational prospects

### 7.1.1 Spectroscopic metallicities of the fields studied

From an observational perspective, the methodology developed in this thesis successfully enabled the extraction of a stacked spectrum for the stellar halo field of NGC 4945 with a S/N of 9.4. This S/N is sufficient to estimate the metallicity using the CaT absorption lines. In Chapter 4, we presented the stacked spectrum of RGB stars in the halo field obtained during this research, clearly showing the two strongest CaT lines. By measuring the equivalent widths (EW) of these lines and applying the Carrera et al. (2013) calibration, the metallicity ([Fe/H]) can be derived. A similar analysis can be performed for the outer disk field, although only the stacked spectrum of RGB stars can be used, as the calibration is specific to this population. In Figure 7.1, we present the stacked spectrum for the outer disk using RGB stars only, which achieves an S/N of 14.8 (as reported in Table 1) and clearly displays all three CaT lines. This methodology has been successfully applied to the stellar stream of NGC 4449 and a dwarf spheroidal galaxy in the M81 halo (Toloba et al., 2016a,b). Comparing the metallicities of the halo and outer disk populations will provide valuable insights into their formation and evolutionary histories. Moreover, this analysis will represent the first spectroscopic metallicity study of a diffuse stellar halo

Table 7.1

| region | F814W (mag) | RGB # | S/N | $v_{LOS}$ (km $s^{-1}$) | $\sigma$ (km $s^{-1}$) |
|---|---|---|---|---|---|
| Up | 23.72 – 25.72 | 409 | 7.2 | $650 \pm 34$ | $119 \pm 41$ |
| Low | 23.72 – 25.72 | 708 | 13.7 | $680 \pm 12$ | $68 \pm 18$ |

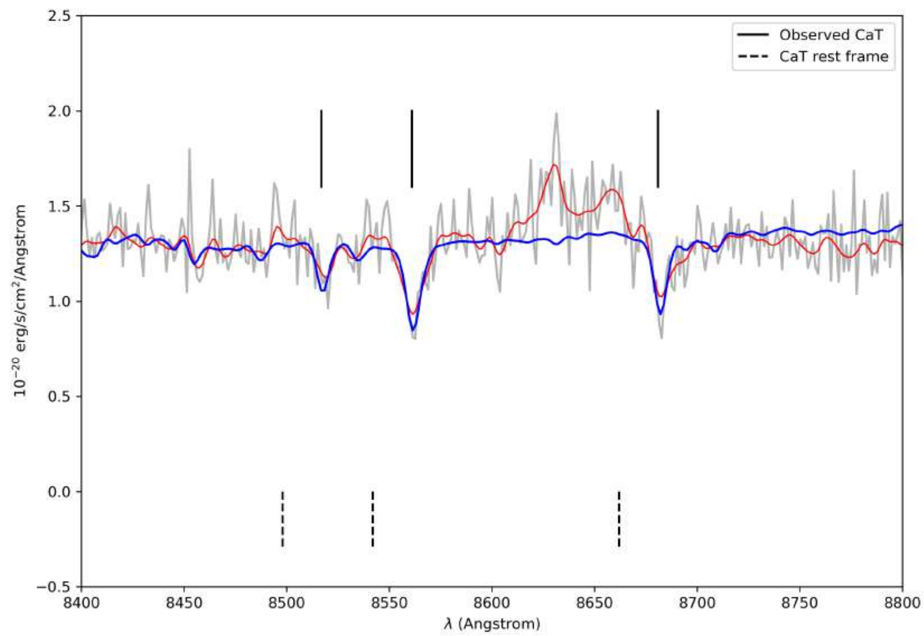


Figure 7.1: Grey represents the median co-added spectrum in the CaT region of 1122 RGB stars in the Outer disk field with F814W magnitude brighter than 25.72. Red: Co-added spectrum smoothed by a Gaussian kernel of 2 pixels weighted by the inverse variance of the sky spectrum. Blue: The best fit from pPXF. Black solid lines mark the position of the CaT lines in the observed spectrum.

beyond the LG using resolved stellar populations and will allow comparisons with metallicities derived photometrically.

### 7.1.2 Outer disk: two different stellar populations

The outer disk field also presents an opportunity for further exploration. In this field, we measured a LOS velocity of 673±11 km s$^{-1}$, along with a high velocity dispersion of 74±12 km s$^{-1}$, which is higher than expected for a rotationally supported disk, where motion is typically more orderly. As discussed in Chapter 2, the lower-right corner of this field is closer to the disk of NGC 4945. When designing the methodology for this thesis, we determined that this corner could not be used for local background subtraction. Thus, we divided the outer disk field into quadrants for further investigation, as shown in Figure 3.11. As part of a preliminary analysis conducted during this thesis, we explored potential variations within the outer disk field by dividing it horizontally into upper and lower regions (Figure 7.2). We produced separate stacked spectra for stars in the upper and lower halves and measured the LOS velocity and velocity dispersion for each region. The upper region yielded a spectrum with an S/N of 7.2, while the lower region achieved an S/N of 13.7. Although the LOS velocities are relatively similar between the two regions, the velocity dispersions differ significantly. In Table 7.1, we present the LOS velocity, velocity dispersion, S/N, and the number of RGB stars used in the stacking for the upper and lower regions. The upper region shows a LOS velocity of 650±34 km s$^{-1}$ and a velocity dispersion of 119±41 km s$^{-1}$. In contrast, the lower region, which is closer to the disk, shows a LOS velocity of 680±12 km s$^{-1}$ and a velocity dispersion of 68±18 km s$^{-1}$.

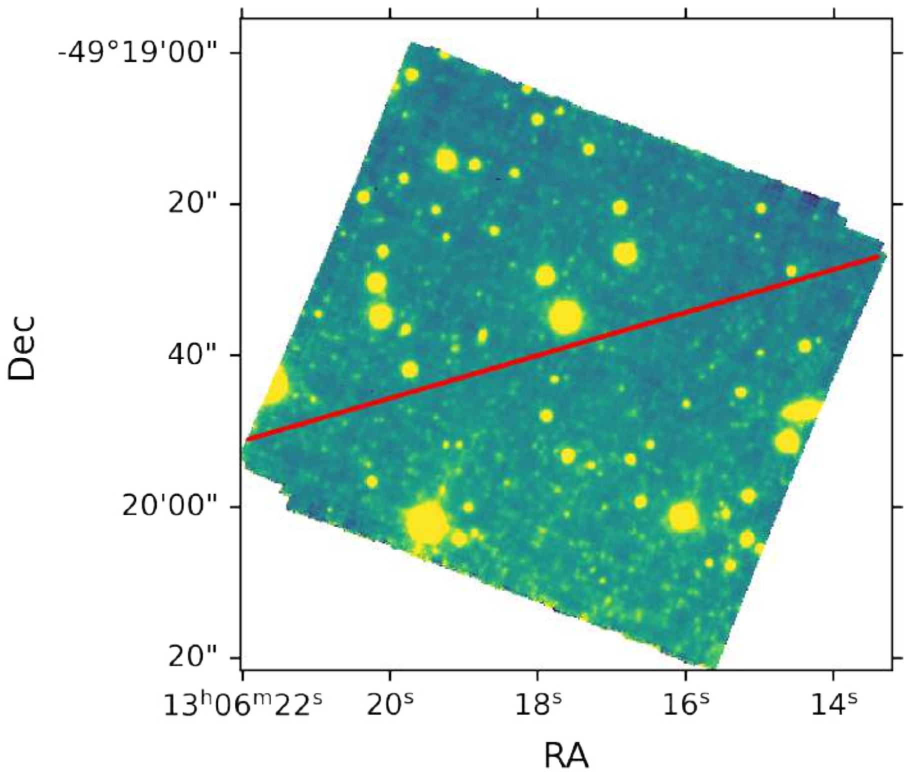


Figure 7.2: Outer disk field divided into two halves: up and down. The lowest corner is closer to the center of the galaxy.

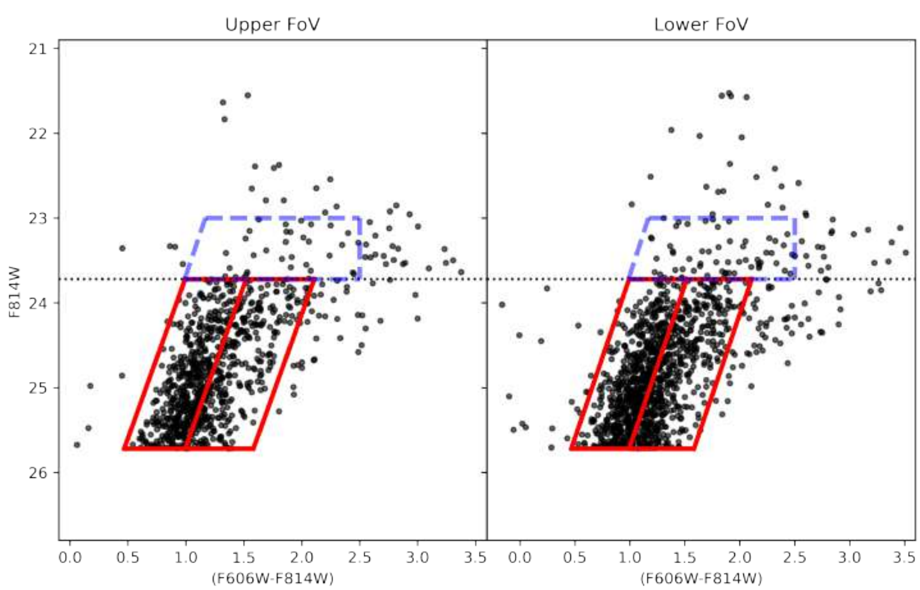


Figure 7.3: Outer disk CMDs for the upper and lower regions of the field.

This preliminary analysis suggests a difference in stellar populations within the FoV. The lower region exhibits a velocity closer to the HI disk velocity of NGC 4945, while the upper region shows a lower velocity and double the velocity dispersion. This could indicate the presence of another stellar population, such as an in situ halo, the thick disk of NGC 4945, or remnants of an accreted satellite, which cause an increase in the velocity dispersion. However, the S/N of the upper-region spectrum is relatively low, with only 409 RGB stars contributing to the stack, making it challenging to draw definitive conclusions.

A promising approach to further investigate this potential population would be to divide the RGB stars in both the upper and lower regions based on their color. In the CMD, the redder RGB stars represent younger, metal-rich populations, while the bluer stars are older and more metal-poor. We divided the RGB population in each region into red and blue subgroups, as shown in Figure 7.3. In the lower region, both red and blue RGB stars exhibit similar LOS velocities ($\sim$680 km s$^{-1}$) but different velocity dispersions: 51$\pm$22 km s$^{-1}$ for the blue population and 82$\pm$23 km s$^{-1}$ for the red. In the upper region, however, the dispersions are significantly different, with the blue RGB stars exhibiting a dispersion of 165$\pm$54 km s$^{-1}$ compared to 49$\pm$65 km s$^{-1}$ for the red stars. This analysis suggests that within the small FoV of the outer disk, we may be detecting evidence of an in situ halo component, distinct from the accreted halo observed at $\sim$35 kpc. While the LOS velocities are not drastically different between the upper and lower regions, the significant differences in velocity dispersion, particularly in the upper region, align with kinematic expectations for a halo population. Moreover, the color-based division reveals a notable difference in the behavior of the red and blue RGB populations, consistent with the idea that older, metal-poor stars (blue RGB) exhibit higher velocity dispersion, while younger, metal-rich stars (red RGB) display more orderly, disk-like kinematics. However, we note that these measurements rely on stacked spectra with relatively low S/N, especially in the upper region, and additional data with longer exposure times are needed to confirm these findings.

Other scenarios, such as the presence of a thick disk or remnants of an accreted satellite, remain possible. Telescopes like the ELT, paired with instruments such as MOSAIC and HARMONI, will enable detailed studies of halo kinematics and metallicities, not only for nearby galaxies but also for more distant systems. These instruments will significantly enhance our ability to characterize stellar halos, enabling studies of NGC 4945's accretion history and the detection of potential satellite galaxies in its halo.

## 7.2 Cosmological simulations

Beyond observational studies, cosmological simulations offer a powerful tool for studying the accretion history of NGC 4945 and for better characterizing its structures and past mergers. Simulations can predict the satellite population of NGC 4945, which could be confirmed observationally with the arrival of next-generation telescopes and instruments. Further exploration using cosmological simulations, particularly those with higher resolution than TNG50 or Auriga, could help resolve the origin of the difference in velocity dispersion observed in the outer disk field. This would be an intriguing project for future work.

# Bibliography


Abadi M. G., Navarro J. F., Steinmetz M., 2006, MNRAS, 365, 747

Abraham R. G., van Dokkum P. G., 2014, PASP, 126, 55

Bacon R., et al., 2001, MNRAS, 326, 23

Bacon R., et al., 2017, A&A, 608, A1

Bailin J., Bell E. F., Chappell S. N., Radburn-Smith D. J., de Jong R. S., 2011, ApJ, 736, 24

Barker M. K., Ferguson A. M. N., Irwin M., Arimoto N., Jablonka P., 2009, AJ, 138, 1469

Bell E. F., et al., 2008, ApJ, 680, 295

Bell E. F., Monachesi A., Harmsen B., de Jong R. S., Bailin J., Radburn-Smith D. J., D'Souza R., Holwerda B. W., 2017, ApJL, 837, L8

Belokurov V., et al., 2006, ApJL, 642, L137

Belokurov V., Erkal D., Evans N. W., Koposov S. E., Deason A. J., 2018, MNRAS, 478, 611

Beltrand C., et al., 2024, arXiv e-prints, p. arXiv:2406.17533

Bendo G. J., Henkel C., D'Cruze M. J., Dickinson C., Fuller G. A., Karim A., 2016, MNRAS, 463, 252

Bhattacharya S., Arnaboldi M., Hammer F., Yang Y., Gerhard O., Caldwell N., Freeman K. C., 2023, MNRAS, 522, 6010

Bird S. A., Xue X.-X., Liu C., Shen J., Flynn C., Yang C., Zhao G., Tian H.-J., 2021, ApJ, 919, 66

Bland-Hawthorn J., Gerhard O., 2016, ARA&A, 54, 529

Boardman N. F., et al., 2017, MNRAS, 471, 4005

Brodie J. P., Strader J., 2006, ARA&A, 44, 193

Bullock J. S., Johnston K. V., 2005, ApJ, 635, 931

Bullock J. S., Kravtsov A. V., Weinberg D. H., 2001, ApJ, 548, 33

Bundy K., et al., 2015, ApJ, 798, 7

Cappellari M., 2017, MNRAS, 466, 798

Cappellari M., 2023, MNRAS, 526, 3273

Cappellari M., Emsellem E., 2004, PASP, 116, 138

Cappellari M., et al., 2011, MNRAS, 413, 813

Carollo D., et al., 2007, Nature, 450, 1020

Carrera R., Pancino E., Gallart C., del Pino A., 2013, MNRAS, 434, 1681

Cohen R. E., Goudfrooij P., Correnti M., Gnedin O. Y., Harris W. E., Chandar R., Puzia T. H., Sánchez-Janssen R., 2020, ApJ, 890, 52

Comerón S., et al., 2023, A&A, 675, A143

Conroy C., et al., 2019, ApJ, 883, 107

Cooper A. P., et al., 2010, MNRAS, 406, 744

Cooper A. P., Parry O. H., Lowing B., Cole S., Frenk C., 2015, MNRAS, 454, 3185

Cortese L., Bendo G. J., Isaak K. G., Davies J. I., Kent B. R., 2010, MNRAS, 403, L26

Croom S. M., et al., 2012, MNRAS, 421, 872

D'Ago G., et al., 2023, A&A, 672, A17

D'Souza R., Bell E. F., 2018, Nature Astronomy, 2, 737

D'Souza R., Kauffman G., Wang J., Vegetti S., 2014, MNRAS, 443, 1433

Dalcanton J. J., et al., 2015, ApJ, 814, 3

Darg D. W., et al., 2010, MNRAS, 401, 1043

Deason A. J., Belokurov V., Evans N. W., 2011a, MNRAS, 411, 1480

Deason A. J., Belokurov V., Evans N. W., 2011b, MNRAS, 416, 2903

Deason A. J., Mao Y.-Y., Wechsler R. H., 2016, ApJ, 821, 5

Deason A. J., Belokurov V., Koposov S. E., Gómez F. A., Grand R. J., Marinacci F., Pakmor R., 2017, MNRAS, 470, 1259

Deason A. J., Belokurov V., Sanders J. L., 2019, MNRAS, 490, 3426

Dey A., et al., 2023, ApJ, 944, 1

Dorman C. E., et al., 2012, ApJ, 752, 147

Dorman C. E., et al., 2015, ApJ, 803, 24

Eggen O. J., Lynden-Bell D., Sandage A. R., 1962, ApJ, 136, 748

Emig K. L., et al., 2020, ApJ, 903, 50

Escala I., Kirby E. N., Gilbert K. M., Cunningham E. C., Wojno J., 2019, ApJ, 878, 42

Escala I., Kirby E. N., Gilbert K. M., Wojno J., Cunningham E. C., Guhathakurta P., 2020, ApJ, 902, 51

Escala I., Gilbert K. M., Wojno J., Kirby E. N., Guhathakurta P., 2021, AJ, 162, 45

Fattahi A., et al., 2019, MNRAS, 484, 4471

Finlez C., et al., 2022, ApJ, 936, 88

Font A. S., McCarthy I. G., Crain R. A., Theuns T., Schaye J., Wiersma R. P. C., Dalla Vecchia C., 2011, MNRAS, 416, 2802

Frenk C. S., White S. D. M., 1980, MNRAS, 193, 295

Frenk C. S., White S. D. M., Davis M., Efstathiou G., 1988, ApJ, 327, 507

Gaia Collaboration et al., 2016, A&A, 595, A1

Gaia Collaboration et al., 2018, A&A, 616, A1

Gaia Collaboration et al., 2021, A&A, 650, C3

Gargiulo I. D., et al., 2022, MNRAS, 512, 2537

Gilbert K. M., et al., 2006, ApJ, 652, 1188

Gilbert K. M., et al., 2007, ApJ, 668, 245

Gilbert K. M., et al., 2012, ApJ, 760, 76

Gilbert K. M., et al., 2014, ApJ, 796, 76

Gilbert K. M., et al., 2018, ApJ, 852, 128

Gilbert K. M., et al., 2022, ApJ, 924, 116

Gilhuly C., et al., 2022, ApJ, 932, 44

Girardi L., Groenewegen M. A. T., Hatziminaoglou E., da Costa L., 2005, A&A, 436, 895

Gómez F. A., White S. D. M., Grand R. J. J., Marinacci F., Springel V., Pakmor R., 2017, MNRAS, 465, 3446

Grand R. J. J., Springel V., Gómez F. A., Marinacci F., Pakmor R., Campbell D. J. R., Jenkins A., 2016, MNRAS, 459, 199

Grand R. J. J., et al., 2017, MNRAS, 467, 179

Greggio L., Rejkuba M., Gonzalez O. A., Arnaboldi M., Iodice E., Irwin M., Neeser M. J., Emerson J., 2014, A&A, 562, A73

Grogin N. A., et al., 2011, ApJS, 197, 35

Guth A. H., 1981, PhRvD, 23, 347

Hammer F., Yang Y. B., Wang J. L., Ibata R., Flores H., Puech M., 2018, MNRAS, 475, 2754

Harmsen B., Monachesi A., Bell E. F., de Jong R. S., Bailin J., Radburn-Smith D. J., Holwerda B. W., 2017, MNRAS, 466, 1491

Harmsen B., Bell E. F., D'Souza R., Monachesi A., de Jong R. S., Smercina A., Jang I. S., Holwerda B. W., 2023, MNRAS, 525, 4497

Hartke J., et al., 2022, A&A, 663, A12

Helmi A., White S. D. M., 1999, MNRAS, 307, 495

Helmi A., White S. D. M., 2001, MNRAS, 323, 529

Helmi A., White S. D. M., Springel V., 2003, MNRAS, 339, 834

Helmi A., Babusiaux C., Koppelman H. H., Massari D., Veljanoski J., Brown A. G. A., 2018, Nature, 563, 85

Hodges-Kluck E., Bregman J. N., 2014, ApJ, 789, 131

Hopkins P. F., Hernquist L., Cox T. J., Di Matteo T., Robertson B., Springel V., 2006, ApJS, 163, 1

Hubble E. P., 1929, ApJ, 69, 103

Ianjamasimanana R., et al., 2022, MNRAS, 513, 2019

Ibata R. A., Gilmore G., Irwin M. J., 1994, Nature, 370, 194

Ibata R., Chapman S., Ferguson A. M. N., Lewis G., Irwin M., Tanvir N., 2005, ApJ, 634, 287

Ibata R., Martin N. F., Irwin M., Chapman S., Ferguson A. M. N., Lewis G. F., McConnachie A. W., 2007, ApJ, 671, 1591

Ibata R. A., et al., 2014, ApJ, 780, 128

Ibata R., et al., 2021, ApJ, 914, 123

Iodice E., et al., 2023, A&A, 679, A69

Ivanov V. D., Coccato L., Neeser M. J., Selman F., Pizzella A., Dalla Bontà E., Corsini E. M., Morelli L., 2019, A&A, 629, A100

Johnston K. V., Spergel D. N., Hernquist L., 1995, ApJ, 451, 598

Johnston K. V., Hernquist L., Bolte M., 1996, ApJ, 465, 278

Johnston K. V., Zhao H., Spergel D. N., Hernquist L., 1999, ApJL, 512, L109

Johnston K. V., Bullock J. S., Sharma S., Font A., Robertson B. E., Leitner S. N., 2008, ApJ, 689, 936

Kamann S., Wisotzki L., Roth M. M., 2013, A&A, 549, A71

Koribalski B. S., et al., 2004, AJ, 128, 16

Koribalski B. S., et al., 2018, MNRAS, 478, 1611

Laporte C. F. P., Johnston K. V., Gómez F. A., Garavito-Camargo N., Besla G., 2018, MNRAS, 481, 286

Law D. R., Johnston K. V., Majewski S. R., 2005, ApJ, 619, 807

Longobardi A., Arnaboldi M., Gerhard O., Mihos J. C., 2015, A&A, 579, L3

Lucero D. M., Carignan C., Elson E. C., Randriamampandry T. H., Jarrett T. H., Oosterloo T. A., Heald G. H., 2015, MNRAS, 450, 3935

Mackereth J. T., Bovy J., 2020, MNRAS, 492, 3631

Makarov D., Prugniel P., Terekhova N., Courtois H., Vauglin I., 2014, A&A, 570, A13

Malin D., Hadley B., 1997, , 14, 52

Martínez-Delgado D., Peñarrubia J., Gabany R. J., Trujillo I., Majewski S. R., Pohlen M., 2008, ApJ, 689, 184

Martínez-Delgado D., Pohlen M., Gabany R. J., Majewski S. R., Peñarrubia J., Palma C., 2009, ApJ, 692, 955

Martínez-Delgado D., et al., 2010, AJ, 140, 962

Martínez-Delgado D., et al., 2012, ApJL, 748, L24

McConnachie A. W., et al., 2009, Nature, 461, 66

McConnachie A. W., et al., 2018, ApJ, 868, 55

Melchior P., et al., 2015, MNRAS, 449, 2219

Merritt A., van Dokkum P., Abraham R., Zhang J., 2016, ApJ, 830, 62

Mingozzi M., et al., 2019, A&A, 622, A146

Monachesi A., et al., 2013, ApJ, 766, 106

Monachesi A., Bell E. F., Radburn-Smith D. J., Bailin J., de Jong R. S., Holwerda B., Streich D., Silverstein G., 2016a, MNRAS, 457, 1419

Monachesi A., Gómez F. A., Grand R. J. J., Kauffmann G., Marinacci F., Pakmor R., Springel V., Frenk C. S., 2016b, MNRAS, 459, L46

Monachesi A., et al., 2019, MNRAS, 485, 2589

Mouhcine M., Ferguson H. C., Rich R. M., Brown T. M., Smith T. E., 2005a, ApJ, 633, 810

Mouhcine M., Ferguson H. C., Rich R. M., Brown T. M., Smith T. E., 2005b, ApJ, 633, 821

Mouhcine M., Rich R. M., Ferguson H. C., Brown T. M., Smith T. E., 2005c, ApJ, 633, 828

Nelson D., et al., 2019, MNRAS, 490, 3234

Peacock M. B., Strader J., Romanowsky A. J., Brodie J. P., 2015, ApJ, 800, 13

Peebles P. J. E., 1984a, ApJ, 277, 470

Peebles P. J. E., 1984b, ApJ, 284, 439

Peng C. Y., Ho L. C., Impey C. D., Rix H.-W., 2002, AJ, 124, 266

Peng E. W., Ford H. C., Freeman K. C., 2004, ApJ, 602, 685

Pillepich A., Madau P., Mayer L., 2015, ApJ, 799, 184

Pillepich A., et al., 2019, MNRAS, 490, 3196

Pillepich A., et al., 2023, arXiv e-prints, p. arXiv:2303.16217

Pilyugin L. S., Tautvaišienė G., Lara-López M. A., 2023, A&A, 676, A57

Planck Collaboration et al., 2020, A&A, 641, A1

Pulsoni C., Gerhard O., Arnaboldi M., Pillepich A., Nelson D., Hernquist L., Springel V., 2020, A&A, 641, A60

Pulsoni C., Gerhard O., Fall S. M., Arnaboldi M., Ennis A. I., Hartke J., Coccato L., Napolitano N. R., 2023, A&A, 674, A96

Purcell C. W., Bullock J. S., Zentner A. R., 2007, ApJ, 666, 20

Purcell C. W., Bullock J. S., Kazantzidis S., 2010, MNRAS, 404, 1711

Quillen A. C., Minchev I., Bland-Hawthorn J., Haywood M., 2009, MNRAS, 397, 1599

Radburn-Smith D. J., et al., 2011, ApJS, 195, 18

Rejkuba M., Mouhcine M., Ibata R., 2009, MNRAS, 396, 1231

Rejkuba M., Harris W. E., Greggio L., Crnojević D., Harris G. L. H., 2022, A&A, 657, A41

Roth M. M., et al., 2005, PASP, 117, 620

Sánchez S. F., et al., 2012, A&A, 538, A8

Schaye J., et al., 2015, MNRAS, 446, 521

Schurch N. J., Roberts T. P., Warwick R. S., 2002, MNRAS, 335, 241

Searle L., Zinn R., 1978, ApJ, 225, 357

Soto K. T., Lilly S. J., Bacon R., Richard J., Conseil S., 2016, MNRAS, 458, 3210

Springel V., 2010, MNRAS, 401, 791

Springel V., Di Matteo T., Hernquist L., 2005a, MNRAS, 361, 776

Springel V., Di Matteo T., Hernquist L., 2005b, ApJL, 620, L79

Stoehr F., et al., 2008, in Argyle R. W., Bunclark P. S., Lewis J. R., eds, Astronomical Society of the Pacific Conference Series Vol. 394, Astronomical Data Analysis Software and Systems XVII. p. 505

Tau E. A., Vivas A. K., Martínez-Vázquez C. E., 2024, AJ, 167, 57

Tissera P. B., Scannapieco C., Beers T. C., Carollo D., 2013, MNRAS, 432, 3391

Tissera P. B., Beers T. C., Carollo D., Scannapieco C., 2014, MNRAS, 439, 3128

Toloba E., Guhathakurta P., Romanowsky A. J., Brodie J. P., Martínez-Delgado D., Arnold J. A., Ramachandran N., Theakanath K., 2016a, ApJ, 824, 35

Toloba E., Sand D., Guhathakurta P., Chiboucas K., Crnojević D., Simon J. D., 2016b, ApJL, 830, L21

Trujillo I., Martinez-Valpuesta I., Martínez-Delgado D., Peñarrubia J., Gabany R. J., Pohlen M., 2009, ApJ, 704, 618

Vera-Casanova A., et al., 2022, MNRAS, 514, 4898

Vogelsberger M., Marinacci F., Torrey P., Puchwein E., 2020, Nature Reviews Physics, 2, 42

Weilbacher P. M., et al., 2020, A&A, 641, A28

Westmoquette M. S., Exter K. M., Christensen L., Maier M., Lemoine-Busserolle M., Turner J., Marquart T., 2009, arXiv e-prints, p. arXiv:0905.3054

White S. D. M., Rees M. J., 1978, MNRAS, 183, 341

Williams B. F., et al., 2015, ApJ, 806, 48

Worthey G., 1994, ApJS, 95, 107

Wright A. C., et al., 2023, arXiv e-prints, p. arXiv:2309.10039

Yang C., Zhu L., Tahmasebzadeh B., Xue X.-X., Liu C., 2022, AJ, 164, 241

York D. G., et al., 2000, AJ, 120, 1579

Zhang X., Chen B., Chen P., Sun J., Tian Z., 2024, MNRAS, 528, 2653

Zinn R., 1985, ApJ, 293, 424

Zolotov A., Willman B., Brooks A. M., Governato F., Brook C. B., Hogg D. W., Quinn T., Stinson G., 2009, ApJ, 702, 1058

Zolotov A., Willman B., Brooks A. M., Governato F., Hogg D. W., Shen S., Wadsley J., 2010, ApJ, 721, 738

de Jong R. S., 2008, MNRAS, 388, 1521

de Vaucouleurs G., de Vaucouleurs A., Corwin H. G. J., Buta R. J., Paturel G., Fouque P., 1991, S&T, 82, 621

van den Bergh S., 1969, ApJS, 19, 145

# Appendix A

# Individual spectra normalization

During the evaluation of this thesis, we realized that the individual spectra were not normalized before stacking. The primary objective of the methodology was to prioritize obtaining a combined spectrum with higher S/N, which would allow us to derive reliable measurements of both radial velocity and velocity dispersion. Tables A.1 and A.2 present the results obtained when normalizing the individual spectra before stacking. We observe that the velocity values in both the halo and outer disk fields remain similar to those obtained without prior normalization. This suggests that even without normalization, our resulting velocities can still be considered reliable.

Figure A.1 shows the combined halo spectrum using pre-normalized individual spectra. Although the spectrum appears noticeably noisier, the CaT absorption lines are still clearly identifiable. However, in both the halo and outer disk fields, the S/N decreases significantly when normalization is applied prior to stacking. This results in increased uncertainties in the derived kinematic parameters. Furthermore, the low S/N of the normalized spectra renders the measurements of velocity dispersion particularly unreliable, especially in the outer disk field. This is evident in Table 2, where the velocity dispersion values vary substantially between different stacked realizations, and the associated uncertainties are very large.

Table A.1: Halo stacked normalized RGB spectra at different magnitude levels. The listed uncertainties are measured by running 1000 Monte Carlo bootstrapping simulations.

| Stack N° | F814W | N # | S/N | $v_{LOS}$ (km s$^{-1}$) | $\sigma$ (km s$^{-1}$) |
|---|---|---|---|---|---|
| 1 | $23.72 - 24.72$ | 14 | 8.0 | $539 \pm 17$ | $47 \pm 29$ |
| 2 | $23.72 - 25.00$ | 28 | 7.3 | $507 \pm 15$ | $46 \pm 26$ |
| 3 | $23.72 - 25.50$ | 43 | 7.7 | $512 \pm 14$ | $37 \pm 25$ |
| 4 | $23.72 - 25.72$ | 53 | 7.3 | $516 \pm 13$ | $31 \pm 23$ |

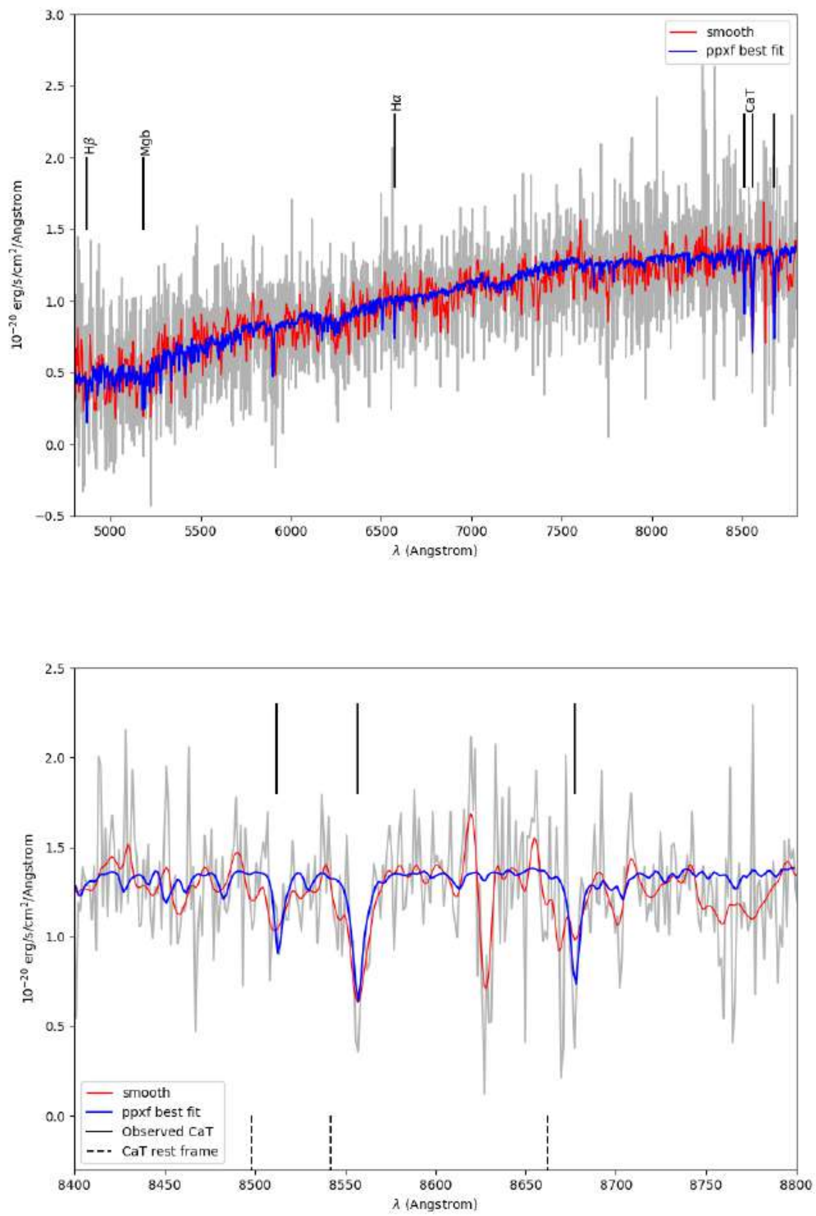


Figure A.1: The stacked normalized spectra of 53 halo RGB stars with F814W magnitude between 23.72 and 25.72. Red: Co-added spectrum smoothed by a Gaussian kernel of 2 pixels weighted by the inverse variance of the sky spectrum. Blue: The best fit from pPXF. In the upper panel we show the full spectrum wavelength, 4800-8800 Å, used to measure velocity with pPXF, in the bottom panel we show a zoom in the CaT region and mark with black dashed lines the position of these lines: 8498, 8542 and 8662 Å in the restframe and black solid lines the position of the observed CaT lines.

Table A.2: 70 normalized AGB plus RGB outer disk stacked stars at different magnitude levels. The values of S/N, velocity, and velocity dispersion are obtained by considering the stacking of RGB and AGB stars. The values within parentheses are considering only the stack of RGB stars. The listed uncertainties are measured by running 1000 Monte Carlo bootstrapping simulations.

| Stack N° | F814W (mag) | RGB # | S/N | $v_{LOS}$ (km s$^{-1}$) | $\sigma$ (km s$^{-1}$) |
|---|---|---|---|---|---|
| 1 | 23.72 – 24.72 | 427 | 8.5 (7.3) | 672 ± 14 (671 ± 17) | 37 ± 25 (27 ± 33) |
| 2 | 23.72 – 25.00 | 622 | 7.7 (6.4) | 670 ± 21 (669 ± 31) | 49 ± 36 (68 ± 49) |
| 3 | 23.72 – 25.50 | 989 | 5.0 (4.5) | 655 ± 51 (664 ± 54) | 130 ± 63 (133 ± 66) |
| 4 | 23.72 – 25.72 | 1122 | 5.5 (4.9) | 671 ± 34 (677 ± 42) | 73 ± 56 (63 ± 63) |

## Acknowledgments

I have reached the end of this stage, filled with ups and downs, but also with a lot of effort throughout the years. I want to dedicate these last words of my thesis to thank those who were an important part of this journey.

First and foremost, I want to thank my advisor, Dr. Antonela Monachesi, for accepting me as your student and for proposing a challenging and beautiful project. Anto, thank you for your patience, support, perseverance, and constant encouragement—for questioning me, for always pushing me forward, especially during the moments when I faltered and felt lost. Without a doubt, you brought out the best in me and helped me grow as a scientist and researcher. I also want to thank Dr. Richard D'Souza for accepting to be my co-supervisor, for being so committed to this project, and for your constant ideas and questions that enriched this thesis.

Thank you to the entire community at the Departamento de Astronomía at the Universidad de La Serena, for always creating a friendly work environment and for the willingness to help whenever I needed it. In particular, I want to thank the members of my Doctoral Advisory Committee—Doug, Ricardo, and Guillermo—for their constructive and positive feedback at the end of each semester.

I extend my heartfelt appreciation to the reviewers who took the time to evaluate my thesis and provide constructive feedback. Their valuable comments and suggestions helped refine and strengthen the final version of this work.

I would like to acknowledge the financial support from the Vicerrectoría de Investigación at the Universidad de La Serena through the Beca Doctoral and the financial support provided by the National Agency for Research and Development (ANID) through the Scholarship Program / Doctorado Nacional / 2021-21211381. I also want to thank the financial support from ANID/FONDECYT Regular/Grant 1181797 and 1212046 (PI Antonela Monachesi), SOCHIAS / Scholarship / Adelina Gutiérrez, the Proyecto Basal FB210003 from Centro de Astrofísica y Tecnologías Afines (CATA), and the PhD Program in Astronomy / ULS, which allowed me to attend various conferences throughout the course of this thesis.

I am grateful to my PhD classmates, with whom I shared enjoyable moments in the office, discussions about our progress and setbacks, and also many moments of coffee, mates, barbecues, and beers. Special mention to my cohort friends Silvio, Mario, and Dania for the mutual support we gave each other, especially during the early years of the PhD. I also want to thank my office mates, Franklin and Gissel, for putting up with my madness, my laughter, and my never-ending forgetfulness. A very special thanks to Eli, who also shared the department with me. Eli and Gissel were fundamental throughout this final stretch—and truly, since the moment we met. Working with you made each day a joy; we laughed endlessly, sometimes cried (especially with Eli), and we always had words of support for one another. I want you to know how much I enjoyed every outing, coffee break, conference, and walk we shared. We have so many stories that we could write another thesis—though maybe we'll just stick to TikTok, jaja.

Thank you to the Team Fénix cycling group for the joy and encouragement you brought me on every ride and every competition I participated in.

Finally, I want to thank my parents, Franco and Pamela, for their endless love, for comforting my heart during every phone call and visit to Iquique, and for always believing in me. To my siblings, to whom I dedicate this thesis: I want you to know that you are always in my thoughts, and I feel incredibly lucky to have you in my life.